Masaryk University
Faculty of Science

Department of Theoretical Physics and Astrophysics

Ph.D. Dissertation

Orbits of open clusters

Lucie Jílková

Supervisor: Mgr. Filip Hroch, Ph.D.
Advisor: RNDr. Bruno Jungwiert, Ph.D.

Brno 2013

Bibliographic Entry

Author	Lucie Jílková Faculty of Science, Masaryk University Department of Theoretical Physics and Astrophysics
Title of Dissertation	Orbits of open clusters
Degree Programme	Physics
Field of Study	Theoretical Physics and Astrophysics
Supervisor	Mgr. Filip Hroch, Ph.D. Faculty of Science, Masaryk University Department of Theoretical Physics and Astrophysics
Academic Year	2012/2013
Number of Pages	158
Keywords	Open clusters, Galactic orbits, Milky Way, NGC 6791, Galactic disk

Bibliografický záznam

Autorka	Lucie Jílková Přírodovědecká fakulta, Masarykova Univerzita Ústav teoretické fyziky a astrofyziky
Název práce	Dráhy otevřených hvězdokup
Studijní program	Fyzika
Studijní obor	Teoretická fyzika a astrofyzika
Školitel	Mgr. Filip Hroch, Ph.D. Přírodovědecká fakulta, Masarykova Univerzita Ústav teoretické fyziky a astrofyziky
Akademický rok	2012/2013
Počet stran	158
Klíčová slova	otevřené hvězdokupy, Galaktické dráhy, Mléčná dráha, NGC 6791, Galaktický disk

Abstract

This thesis is focused on study of Galactic orbits of open clusters. Well known observational advantages in the characterization of star clusters have yielded many important results helping us to understand physical processes on various scales – from the stellar evolution, up to the constraints on the chemodynamical evolution of the Milky Way disk and galactic disks in general. Clusters kinematics, orbital history, and their connection with other clusters characteristics are an important part of the information these stellar systems hold.

In the first part of the thesis, we concentrated on the open cluster NGC 6791. This is a unique case in the Galactic system of open clusters, being one of the oldest (with age about 8 Gyr) and, at the same time, one of the most metal-rich ([Fe/H]$\sim$ +0.4) open clusters known. The current position of NGC 6791, at the Galactocentric radius of about 8 kpc, contradicts the classical picture of the metallicity gradient as traced by open clusters, which predicts a much lover metallicity for a cluster at this radius. The number of unique characteristics of NGC 6791 possess the basic question of the cluster origin and history. In this thesis, we study the cluster orbit and investigate the possibility that the cluster formed close to the Galactic center and later migrated outward to its current location. To this aim, we integrated orbit of NGC 6791 in a potential consistent with the present-day picture of the Milky Way including the Galactic bar and spiral arms. Multiple non-axisymmetric patterns induce one of the possible mechanisms of radial migration. Current cluster orbit is compared with orbits originating in the inner Galactic disk regions. The results show that only the combined model, including both the bar and spiral arms, could bring the cluster to its current position with orbit similar to the current one. However, even thought the scenario is plausible, its probability based on our calculations is very low (less then 1%). Further, using a theoretical approximation for star cluster mass loss presented in the literature, we have also performed a basic estimate of the NGC 6791 initial mass.

In the second part of the thesis, we investigated orbits of a sample of 34 open clusters. The clusters were selected to have a high-resolution metallicity estimate available in the literature. We obtained clusters mean proper motion vectors using data on individual stars from the UCAC4 catalog. Orbits are calculated in the axisymmetric model as well as in the model including the bar and spiral arms. We investigate orbital parameters and their connection with the clusters metallicities and ages, and also the possible time evolution of the radial metallicity gradient. However, we do not find any significant evidence for the latter and reasons and implication of our results are discussed.

Abstrakt

Tato práce se zabývá studiem Galaktických drah otevřených hvězdokup. Výhody pozorování hvězdokup jsou dobře známé a přinesly mnoho zásadních výsledků vedoucích k pochopení astrofyzikálních procesů na různých škálách – od základů hvězdného vývoje až po chemodynamický vývoj Galaktického disku (a disků obecně). Kinematika a dráhy hvězdokup v kontextu dalších charakteristik těchto systémů jsou důležitou částí poznání, které hvězdokupy nesou.

V první části prezentované práce jsme se zaměřili na studium dráhy otevřené hvězdokupy NGC 6791. Jde o jedinečný systém, který s věkem okolo 8 Gyr patří mezi nejstarší a zároveň, s metalicitou [Fe/H]$\sim +0.4$, nejvíce na kovy bohaté známé otevřené hvězdokupy. Současná poloha NGC 6791 v Mléčné dráze s Galaktocentrickým poloměrem 8 kpc protiřečí klasickému obrazu radiálního gradientu metalicity otevřených hvězdokup. Tento gradient předpovídá výrazně nižší obsah kovů pro systém nacházející se v takové vzdálenosti od Galaktického centra. Množství zvláštních chrakteristik pozorovaných u hvězdokupy NGC 6791 přirozeně vzbuzuje otázku, jaký je původ tohoto systému. V prezentované práci jsme se soustředili na variantu, kdy se systém sformoval blízko Galaktického centra a později se přemístil – migroval – do větší vzdálenosti v disku, kde ho pozorujeme dnes. S užitím modelu, který je v souladu se současně známým obrazem Mléčné dráhy, jsme provedli integrace dráhy hvězdokupy NGC 6791. Model obsahuje také Galaktickou příčku a spirální ramena. Vícenásobné osově nesymetrické poruchy jsou jednou z možných příčin procesu radiální migrace. Současná dráha hvězdokupy je porovnána s drahami pocházejícími ve vnitřních částech disku. Výsledky ukazují, že pouze kombinovaný model, obsahující jak příčku tak i spirální ramena, je schopný vytvořit dráhu podobnou současné dráze NGC 6791 a přemístit tak hvězdokupu do její současné polohy. Nicméně, pravděpodobnost realizace takové dráhy odhadujeme na základě našich výpočtů jako velmi nízkou (menší než 1%). S použitím teoretické aproximace pro popis ztráty hmoty z hvězdokup popsané v literatuře, jsme dále provedli jednoduchý odhad původní hmotnosti hvězdokupy NGC 6791.

V druhé části práce prezentujeme dráhy 34 otevřených hvězdokup. Výběr jednolivých hvězdokup byl podmíněn dostupností informace o jejich metalicitě pocházející ze spektroskopického měření s vysokým rozlišením. Vektor vlastního pohybu pro tyto systémy jsme odvodili s užitím dat pro jednotlivé hvězdy prezentovaných v katalogu UCAC4. Dráhy jsou spočítány s užitím osově symetrického modelu a modelu obsahujícím osově nesymetrické komponenty (příčka a spirální ramena). Jsou prozkoumány možné souvislosti dráhových elementů (výstřednost, vertikální amplituda) s dalšími vlastnostmi hvězdokup (metalicita a stáří). Dále je také zkoumán možný časový vývoj radiálního gradientu metalicity hvězdokup. Přítomnost časového vývoje však není v našich výsledcích prokázána a diskutujeme možné příčiny a důsledky.

Acknowledgment

This research has made use of the NASA's Astrophysics Data System

This research has made use of the VizieR catalogue access tool, CDS, Strasbourg, France.

This publication makes use of data products from the Two Micron All Sky Survey, which is a joint project of the University of Massachusetts and the Infrared Processing and Analysis Center/California Institute of Technology, funded by the National Aeronautics and Space Administration and the National Science Foundation.

This research has made use of the WEBDA database, operated at the Institute for Astronomy of the University of Vienna.

I acknowledge the support by two-year European Southern Observatory (ESO) PhD studentship, held at Santiago, Chile.

I acknowledge the support by grants No. 205/08/H005 (Czech Science Foundation) and MUNI/A/0968/2009 (Masaryk University in Brno).

When I started my PhD studies in September 2008, I had only a little clue what I was going to write this very thesis about. The way to its final topic and content was maybe a little nonstandard. Here, I would like to express my heartfelt gratitude to the people and institutions that helped me to walk this way, and that supported me and my work during these past (almost) five years.

I thank Filip Hroch for being my supervisor and for making my PhD studies possible. He helped me in many practical aspects of my work, especially these concerning programming or statistics.

I thank Bruno Jungwiert for being my thesis advisor and for supporting me and my work greatly during the time of my PhD studies. I thank him for sharing with me his knowledge of galactic dynamics and astrophysics in general. I also thank him for gathering and organizing the *pidi-group*, which have assimilated me as its member. I am glad I can be part of this working group and I am also grateful to its other members – Ivaana Ebrová, Miroslav Křížek, Tereza Skalická, Ivana Orlitová, Kateřina Bartošková, Michal Bílek, and Adam Růžička – for all the seminars, discussions, journal-club sessions, football

matches, and the overall motivating atmosphere they have created. I hope we will share many more of these!

I thank Giovanni Carraro for being my supervisor during the time I have spent at ESO Santiago and for his support during that and later times. He has presented the cluster NGC 6791 and open clusters in general to me. I am grateful for the collaboration with him, for all the tasks he assigned me, and for that he showed me what working efficiently means. He also introduced me the observatories in Chile, where astronomy is made at the first place, by including me in projects held not only at Paranal but also at smaller – but not small – observatories of Cerro Tololo and Las Campanas.

I thank the Department of Theoretical Physics & Astrophysics (DTPA, Faculty of Science, Masaryk University in Brno) for supporting me and providing me facilities which made my PhD studies possible.

I am grateful to ESO for the support by the two-year studentship held in Santiago de Chile. I would like to thank the whole Santiago ESO Science office, and especially its director by the time of my stay, Michael West, for creating an unique scientific environment. My stay at ESO gave me a whole new perspective on what working as an astronomer can be.

I thank Ivan Minchev for the discussions and ideas about radial migration and for his collaboration on the paper about open cluster NGC 6791.

I thank Alvaro for his comments on part of this manuscript and for the caterpillarish remarks he never spared me. These were giving me more motivation than Alvaro himself was probably aware of.

I thank my friends and fellow PhD students at the DTPA in Brno as well as at ESO Santiago. Especially, I thank Tereza and Tomáš – for the many discussions inside and outside the office, for practical and psychological support, for the direct and indirect encouragement they have been giving me during the time of our PhD studies and the time at university in general – we have spent together almost ten years. It was great, important, and helpful to have them around! I also thank them for bearing my grumpiness and moodiness which have affected me widely during the recent several months. I thank Tereza for proofreading this manuscript and for all her comments.

In a way, I am also grateful to this thesis. The graduate research aiming to it made me meet many interesting people and travel to various places all around the world. Before all else, during the time I have spent in Chile, I encountered many great people, and some of them have become very close and important to me. Thanks to them, my time in Chile was much richer than what work alone could offer.

In advance, I thank my brother for a bottle of the finest Rioja that he will award me for submitting this thesis before he does that with his – I hope we will enjoy that wine together soon! Finally I thank my parents for always being supportive and never doubting me and my choices.

Díky! Thanks! ¡Gracias!

Lucie
Brno, April 2013

Contents

List of acronyms

2MASS	Two Micron All Sky Survey
AGB	asymptotic giant branch
AMR	age–metallicity relation
CDS	Strasbourg astronomical Data Center
CMD	color–magnitude diagram
ESO	European Southern Observatory
GC	globular cluster
GMC	giant molecular cloud
HB	horizontal branch
HST	Hubble Space Telescope
IMF	initial mass function
MS	main sequence
MW	Milky Way
OC	open cluster
PDF	probability density function
PM	proper motion
RGB	red giant branch
RV	radial velocity
SDSS	Sloan Digital Sky Survey
S/N	signal to noise
SPH	smoothed particle hydrodynamics
UCAC	US Naval Observatory CCD Astrograph Catalog
UV	ultraviolet
VPD	vector point diagram
WD	white dwarf

Preface

During the time of my PhD studies (September 2008–April 2013), I have been working on several different topics with two main focuses – the Galactic orbits of open clusters, and the structure of line-profiles in shell galaxies. The former topic has been of my interest since my two-year studentship (December 2009–December 2011) at ESO in Santiago, Chile, where I worked under the supervision of Giovanni Carraro (ESO, Santiago, Chile) and my thesis advisor Bruno Jungwiert (Astronomical Institute, Academy of Sciences of the Czech Republic, Prague). The research on orbits of open cluster is described in detail in this thesis.

The work on shell galaxies is not explicitly included here, even though much of what I have learned while dealing with shell galaxies was helpful for the research described in the presented thesis. I have been working on the topic of line-profiles in shell galaxies mostly during the first year of my PhD (September 2008–December 2009) but also during some later periods of my studies. The work was stimulated by the collaboration mainly with Bruno Jungwiert and Ivaana Ebrová from the Astronomical Institute, Academy of Sciences of the Czech Republic, Prague, and other colleagues who are, or were during a certain period of their research career, affiliated to the same institute – Miroslav Křížek, Ivana Orlitová, and Michal Bílek – as well as with colleagues from my current institute (Department of Theoretical Physics and Astrophysics, Faculty of Science, Masaryk University, Brno) – Tereza Skalická and Kateřina Bartošková. The work on shell galaxies is a non-negligible part of the scientific output of my PhD studies and resulted into several publications. Among the most important are the poster presentation Jílková et al. (2010) and the refereed publication Ebrová et al. (2012). My contribution and interests in these projects were mainly the test-particle simulations of a minor merger of galaxies originating shells and their further analysis (using principally similar methods to the integration of Galactic orbits). I have also contributed to the development and numerical calculations of the theory of radial oscillations approximately describing the kinematics of stars in shells (see Ebrová et al., 2012, for details).

Apart from the studies of Galactic orbits and shell galaxies, I have also participated in an investigation of blue stragglers populations in four Sagittarius dwarf spheroidal galaxy globular clusters based on the data from the Danish Telescope at ESO La Silla presented by Salinas et al. (2012). In this project, we observed and analyzed photometry of four Sagittarius dwarf globular clusters. We measured the structural parameters of the clusters using the fitting of King profiles. We identify the blue stragglers and compared charac-

teristics of their populations with the horizontal branch stars and the red giant branch stars. In more detail, my contribution to the project included the construction of surface stellar density profiles for clusters and their fitting with the King profile. I have also participated in the statistical analysis of the results (Anderson-Darling tests comparing the radial distributions of stars of various evolutionary stages).

References

Ebrová, I., Jílková, L., Jungwiert, B., Křížek, M., Bílek, M., Bartošková, K., Skalická, T., & Stoklasová, I. 2012, A&A, 545, A33

Jílková, L., Jungwiert, B., Křížek, M., Ebrová, I., Stoklasová, I., Bartáková, T., & Bartošková, K. 2010, Galaxy Wars: Stellar Populations and Star Formation in Interacting Galaxies, ed. B. Smith, J. Higdon, S. Higdon, & N. Bastian, volume 423 of ASP Conference Series, page 243

Salinas, R., Jílková, L., Carraro, G., Catelan, M., & Amigo, P. 2012, MNRAS, 421, 960

Chapter 1

Introduction

Star clusters have played an important role in astrophysical research. They are aggregates of stars formed roughly simultaneously from the same well-mixed molecular cloud, and they hold together by their mutual gravitational attraction. Therefore, the stars in clusters have approximately the same age and chemical composition. A star cluster occupies a relatively small volume of space and its stars have the same distance from the Sun. At the first sight, cluster appears as a simple stellar population. Individual stars differ in their mass and clusters provide us an unique probe into the star evolution history. At the same time, due to the common properties of stars, it is possible to derive clusters characteristics – such as their distance to the Sun, chemical composition, age, radial velocity, or proper motion – from observations in an easier and more precise way than for the field stars. Moreover, many clusters are bright objects and can be observed at large distances.

Star clusters are observed in the Milky Way (MW) as well as in external galaxies. The Galactic star clusters are classically divided into two main types – globular clusters (GCs) and open clusters (OCs). GCs are usually part of the bulge and halo population, they are massive (10^4–$10^6\,M_\odot$), the distribution of their stars is nearly spherically symmetric and very dense in the center. They are very old and are probably remnants of the formation of the MW itself. GCs generally do not contain any gas, dust, or young stars. They are dynamically old and belong to the simplest observed stellar systems. On the other hand, OCs are young systems, most of them with age below 1 Gyr. Their masses are usually within the range of 10^2–$10^4\,M_\odot$, and the distribution of their stars is more irregular than in the GCs. They are strongly concentrated to the Galactic plane and sometimes being referred to as *Galactic clusters*. OCs are continuously forming in the Galactic disk in the giant molecular clouds (GMCs). It is believed that almost all star formation happens in clustered environment (70–90%, see, e.g., Lada & Lada, 2003 for a review on the early stages of clusters evolution). Star clusters are considered as building blocks of galaxies. However, only a small fraction of clustered systems, originally embedded in gas and dust, survives the very early evolutionary stages with strong stellar winds and supernovae explosions (so-called *infant mortality*). During their later life, due to internal processes

in the clusters as well as due to their interaction with the external environment, clusters loose their mass and their lifetime is limited.

The MW contains about 150 GCs (Harris, 1996) and the total number of OCs is estimated to be of order of 10^5 (Piskunov et al., 2006; Bonatto et al., 2006). Star clusters also serve as a probe of the structure and evolution of their surrounding galactic environment. Mapping of the spatial distribution, kinematic properties, and chemical composition of star clusters systems have brought important information about galaxies and about the MW particularly. The young OCs are tracers of star formation, spiral structure, and constrain the chemodynamical evolution of the Galactic disk; while old GCs helped to reveal the halo structure and its overall scale. Characteristics of individual clusters in the overall Galactic context constitute an important part of information we can learn from star clusters.

In this thesis, we focus on study of orbits of OCs. Kinematics and orbits carry information about a part of cluster history. Orbits are given by the environment in which the cluster lives – by the Galactic gravitational potential of the MW. Hence the orbits bring information about the clusters themselves, as well as about the MW.

For about 30 past years, it was believed that stars (and star clusters) stay in the same part of the Galactic disk for most of their lives. This assumption has many implications and it allows to recover the history of a part of the disk at particular radius based on the present-day observations of stars of various ages. However, many recent theoretical works on the galactic disks dynamics weaken this classical assumption and show that many stars may wander several kiloparsecs in the disk during their lives. This phenomenon is called *radial migration* and received much attention in the last years. Several independent processes inducing the radial migration have been identified and described. The non-axisymmetric rotating components, such as spiral arms and bars, which are present also in the MW, are expected to play a very important role for the radial migration. Therefore, we include the Galactic bar and spiral arms in our models of the MW gravitational potential. This makes possible to take into account one of the known mechanisms of radial migration and estimate its possible influence on the orbits.

Closer look at individual clusters reveals many peculiarities. Some of them are common to the whole population, e.g., variations in the chemical composition of GCs, or a presence of unusual objects (as blue stragglers); others make individual clusters exceptional in the whole population. Example of such peculiar case is the open cluster NGC 6791. It is one of the oldest, most metal-rich, and massive OC known and it shows several features unique among the other Galactic OCs. Complete explanation for the complex characteristics and origin of NGC 6791 is still missing. All scenarios suggested to explain the cluster origin involve an exotic Galactic orbit. One of the objectives of this thesis is to derive current orbital parameters of this cluster and investigate the possible influence of the non-axisymmetric disk components on its orbit. This kind of study has not been presented so far and is interesting in the context of the radial migration influence on OCs.[1]

[1] We have presented the results of this investigation (described in Sect. 5 of this thesis) also in the refereed publication Jílková et al. (2012).

Other objective of this thesis is to investigate orbits of a larger sample of OCs. With the growing quality and quantity of the observed data, wide amount of information is available for many OCs. The number of works compiling and further analyzing larger samples of OCs has increased in the recent decade. However, a study describing orbits of OCs calculated using a model including the non-axisymmetric perturbations is missing, even though a significant influence of these on the disk dynamics is expected from the theoretical works. Therefore, first we collect a sample of OCs – compiling and deriving clusters up-to-date characteristics necessary for the orbit calculations. Then, we calculate orbits using our MW model including the non-axisymmetric patterns. We further study the possible connection of orbital parameters with other clusters properties (age or metallicity) and overall characteristics of the OCs system (especially the radial metallicity gradient and its behavior in time).

This thesis is organized as follows. In the first part of Sect. 2 (Sects. 2.1 to 2.5), the present-day general knowledge of the population of OCs is summed up, including their spatial distribution, kinematics, and metallicity distribution. Section 2.6 describes the up-to-date knowledge about the cluster NGC 6791 that is further the main subject of a part of this thesis. Section 3 includes a summary of basic models for the chemodynamical evolution of the galactic disks and a description of the known radial migration mechanisms. In Sect. 4 we describe the model of the Galactic potential and how the orbits are integrated. Section 5 includes the study of the current orbit of NGC 6791 and the investigation of its possible origin in the inner Galactic disk. In Sect. 6, we derive the mean PM vectors for a sample of OCs to investigate their orbital properties in connection with their age and metallicity. Finally, Sect. 7 is the summary and conclusion of the information and work presented in this thesis. Appendices A to C include mostly auxiliary technical information, numbers, and plots which might be useful for a more detailed study or comparison. List of my publications is given in Appendix E.

Chapter 2

Galactic population of open clusters

The Galactic population of OCs has long been of a great interest and its studies provided us an insight to the structure, kinematics, dynamics, formation and evolution of the Galactic disk. It is believed that the Galactic disk is a superposition of two distinct components – the thin and thick disk. This idea was firstly suggested based on the observations of the disk vertical density of stars in the solar neighborhood, which is accurately fitted by two exponentials (Gilmore & Reid, 1983) with scale heights around 300 pc and 900 pc for the thin and thick disk, respectively (Jurić et al., 2008). Stars of the thick disk are generally older and have different chemical composition (lower metallicities) and also different kinematics than the thin disk stars. The surface density of the thick disk is about 7% of that of the thin disk (Binney & Tremaine, 2008). Most of the local stars in the Galactic plane belong to the thin disk population, even though, the fraction of the thick disk stars is still under discussion with values ranging 2–12% (see, e.g., Turon et al., 2008, and references therein). OCs are part of the thin disk population.

In the first part of this chapter (Sects. 2.1–2.5), we give a brief summary of the most important characteristics of the Galactic OCs population as published in the literature. In the second part of this chapter (Sect. 2.6), we describe a particularly interesting case of the open cluster NGC 6791. Additionally, in Sect. 2.7, we give a brief summary about observed abundance variations and multiple stellar generations in GCs, since this phenomenon seems to be important also for the case of NGC 6791.

2.1 General characteristics

As mentioned above, OCs are believed to be a good tracers of the Galactic disk in many points of view. Studies of the Galactic population of OCs have therefore been carried out for several decades, since a bigger sample of observed clusters having basic characteristics measured started to be available. The total number of Galactic OCs is estimated to be of order of 10^5 (Piskunov et al., 2006; Bonatto et al., 2006). By today, thousands of studies

of individual OCs exist in the literature. They are based on data obtained using different observational methods with different precision and further processing, resulting together in a rather inhomogeneous collection. Any analysis of general characteristics of the OCs population should be careful to this inhomogeneity. The observed sample of OCs is naturally also influenced by selection effects, with poorly populated, less luminous (older, less massive) systems being more difficult to identify against the stellar background. The combination of these effects brings complications for any comprehensive analysis of the OCs population and its detailed characteristics are still under discussion (see, e.g., Moitinho, 2010).

Here, we give a brief summary of basic characteristics of the OCs population – its spatial distribution, kinematics, ages, and metallicities – as published in the literature.

2.2 Spatial distribution of OCs

Early studies, e.g., Lyngå (1982), Janes & Adler (1982), or Janes et al. (1988), are compiled in various versions of the Lund Catalog of Open Clusters Data (Lyngå, 1987, the latest 5th edition). Although these datasets were smaller, and they had lower precision and completeness than those available today (compare 300 OCs used by Lyngå, 1982 and about 650 clusters analyzed later by Bonatto et al., 2006 or Piskunov et al., 2006), several characteristic properties of the OCs population have been noticed already in these early works. One of the most important results is that the distribution of young OCs (age $< 20\,\mathrm{Myr}$) in the Galactic plane was found to have three concentrations (Perseus, Sagittarius, and Carina) associated with the spiral arms features. Further, based on their sample of about 300 OCs, Lyngå (1982) found that the horizontal plane of symmetry of the OCs system, the Galactic plane, is displaced by about 20 kpc with respect to the Sun. While the vertical distribution seems to be independent on clusters age up to $\sim 1\,\mathrm{Gyr}$, the older clusters (age $\gtrsim 1\,\mathrm{Gyr}$) tend to have higher vertical distances from the Galactic plane and they are also more frequently found in the outer disk with Galactocentric radii beyond the solar circle. This is partially result of a selection effect – clusters are generally more easily detected at higher vertical distances and in the Galactic center anti-direction – and also of the fact that further from the Galactic plane and further from the Galactic center, clusters are subject of less disruption processes.

With the increasing amount of available data, new catalogs and databases of OCs were created in the last decade. Recently, the most used are: the compilation by Dias et al. (2002a, currently, the latest version V3.2 available was updated in January 2012)[1] listing characteristics of 2135 OCs compiled from various sources; the database WEBDA[2] collecting various information and references about clusters, as well as about their individual stars, from variety of sources; the Catalogue of Open Cluster Data[3] by Kharchenko et al.

[1] Available in electronic form at the CDS (Strasbourg astronomical Data Center) online archive and at `http://www.astro.iag.usp.br/~wilton/`.

[2] `http://www.univie.ac.at/webda/`.

[3] Available in electronic form at the CDS online archive.

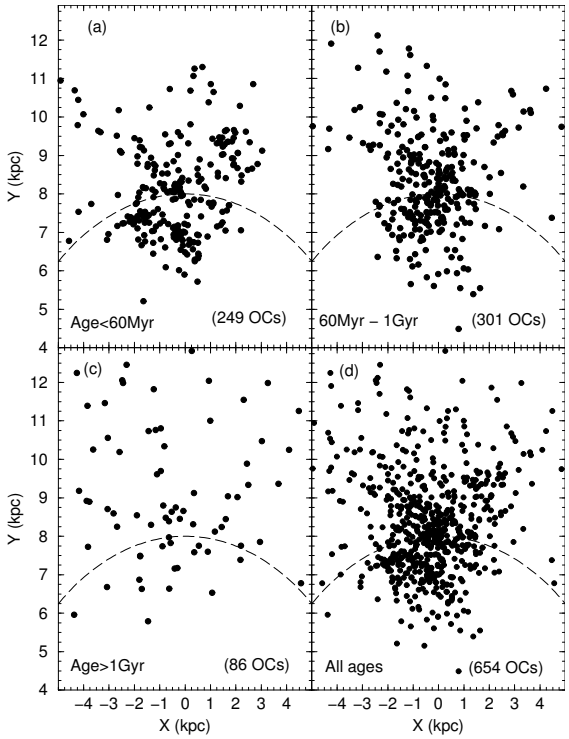

Figure 2.1: Spatial distribution of OCs in the Galactic plane divided into age bins; reproduced from Bonatto et al. (2006, their Fig. 1). A sample of 654 OCs taken from the WEBDA database (clusters with available reddening, distance to the Sun, and age are used) is plotted. Intervals of individual age bins are indicated in the lower left corner of each panel. The dashed curve shows the solar circle with the Galactocentric radius of 8 kpc. Coordinate system is centered at the Galactic center.

(2005a,b), who in a uniform way derived distances, reddening, sizes, ages, and proper motion (PM) for 650 OCs, and radial velocity (RV) for 359 of them.

Using information from the above mentioned compilations, new comprehensive studies of the Galactic population of OCs have been made in the recent years, e.g., Piskunov et al. (2006); Bonatto et al. (2006); Zhu (2009). Bonatto et al. (2006) used OCs with reddening, distance to the Sun, and age available in the WEBDA database (sample of 654 OCs). Their Fig. 1. showing the spatial distribution of the sample in the Galactic plane is reproduced in our Fig. 2.1. Clusters in various age bins are plotted in panels (a)–(c) and the whole sample in the panel (d). Signatures of the spiral structure can be noticed in the distribution – the young clusters with age < 60 Myr, panel (a), trace the local Orion arm (solar circle plotted by the dashed curve is located close its inner edge), and the dip between Orion and Sagittarius-Carina Arms is noticeable around the radius of 7.5 kpc, similarly as in the distribution of the whole sample in the panel (d). The distribution of old OCs with age > 1 Gyr, panel (c), seems to be uniform, with more old clusters detected beyond the solar circle, as it was already noticed in the earlier investigations.

Bonatto et al. (2006) further fitted the completeness corrected OCs radial distribution in the radial range of 5–14 kpc with an exponential profile, resulting in the scale length of about 1.5–1.9 kpc, smaller than it is found for stars (e.g., Jurić et al., 2008, found scale length of 2.6 kpc for the thin disk stars). They also derived completeness corrected number volume density of OCs in the solar neighborhood to be (795 ± 70) clusters per kpc^3. Piskunov et al. (2006) analyzed the spatial distribution and kinematics of the homogeneous sample of Kharchenko et al. (2005a,b), for which they derived completeness limit for the projected distance to the Sun of 0.85 kpc (but see the discussion in Moitinho, 2010). The sample within this limit has a typical number surface density of (100 ± 10) clusters per kpc^2.

Both, Piskunov et al. (2006) and Bonatto et al. (2006), studied the vertical distribution of OCs assuming it can be described with an exponential decay profile. For young clusters (age $<$ 200 Myr) both works found a scale height of about 50 pc. However, while Piskunov et al. (2006) obtained a similar value also for the older population (200 Myr $<$ age $<$ 1 Gyr), Bonatto et al. (2006) found the scale height significantly increasing with the clusters age and obtained value of about 150 pc. The even older (age $>$ 1 Gyr) population is found to distribute almost uniformly with the vertical distance from the Galactic plane. Bonatto et al. (2006) also found that the scale height increases with Galactocentric radius. As mentioned above, older clusters are preferentially found at larger radii and higher vertical distances, probably due to the ability to survive the disruption process further from the Galactic plane in combination with the selection effect (at larger Galactocentric radii, clusters farther from the Galactic plane are more easily detected).

Because the star formation in the MW happens mostly in the spiral arms, the location of the young OCs has long been used as a tracer of the Galactic spiral structure (e.g., Becker & Fenkart, 1970; Palouš et al., 1977). Recently, Dias & Lépine (2005) revised and confirmed this concept, deriving the angular velocity of the spiral pattern from the supposed birth places of OCs (see details in the following Sect. 2.3).

2.3 Kinematics of OCs

Since the early studies, radial velocities of OCs have been used to trace the local kinematics (solar motion, Oort's constant A, or the rotation curve). For example, Hron (1987) presented a compilation of radial velocities for about 100 young OCs (age $<$ 30 Myr), showing that their kinematics agrees with the flat rotation curve of 220 km s^{-1} at solar radius of 9 kpc derived from HII-regions and molecular clouds. Scott et al. (1995) found the rotation of 35 old OCs (older than 1 Gyr) to be consistent with the one of Hron (1987) for young OCs but with a larger dispersion about the mean rotation curve (dispersion of 29 km s^{-1} for the old OCs compared to 10 km s^{-1} for the younger clusters, see also Lyngå & Palouš, 1987 or Friel, 1995 for a summary).

Before the large astrometric surveys started, mean PM vectors were known only for several tens of OCs. The knowledge of the cluster mean PM and RV allows to calculate the cluster orbit. Early investigations in this direction were carried out for example by

Keenan et al. (1973), Keenan & Innanen (1974), Palouš et al. (1977), Allen & Martos (1988), Carraro & Chiosi (1994), Finlay et al. (1995), or Piatti et al. (1995).

The all-sky PM surveys made possible to obtain PMs for a large number of OCs. The Hipparcos and Tycho2 catalogs (Perryman & ESA, 1997), and different versions of the US Naval Observatory CCD Astrograph Catalog (UCAC2 Zacharias et al., 2004, UCAC3 Zacharias et al., 2010, and its final version UCAC4 Zacharias et al., 2012b), belong to the most important catalogs. Measurements of PMs for number of individual stars located within clusters fields have been used to study the cluster membership probabilities and consequently the mean PM vectors of clusters. Depending on the used catalog, its data precision, and method used for the membership analysis – which itself is a crucial step for the correct derivation of the mean value of any cluster parameter – different results might be obtained for individual clusters (see Frinchaboy & Majewski, 2008, for a discussion comparing the catalogs in the context of deriving the open clusters PMs and details of the membership analysis; more details are also given in Sect. 6.4.1). Cataloged PMs data were used by many authors, for studies of individual OCs as well as for homogeneous compilations of many OCs: Baumgardt et al. (2000) used the Hipparcos catalog to derive mean PMs of 205 OCs. Dias et al. (2001, 2002b) and Loktin & Beshenov (2003) used the Tycho2 catalog to obtain mean PMs of 206 and 167 OCs, respectively; Tycho2 catalog was also used by Kharchenko et al. (2005a,b) to create a homogeneous catalog of clusters parameters of 520 OCs (including their mean PMs); Dias et al. (2006) used the UCAC2 catalog to obtain mean PMs for 428 OCs. Comparisons of these PMs compilations can be found, for example, in Kharchenko et al. (2005a) or Dias et al. (2006), who did not find any statistically significant difference among them. More quantitatively, Dias et al. (2006) found the mean difference in PMs between their (using the UCAC2 catalog) and the other published results to be about $1\,\mathrm{mas\,yr^{-1}}$.

Together with the PMs compilations, RVs for a larger clusters sample were derived in a homogeneous way in several studies: Kharchenko et al. (2005a,b), who presented their result in the Catalogue of Open Cluster Data (see also Sect. 2.2); Frinchaboy & Majewski (2008) derived RVs of 71 OCs (using a medium-resolution spectroscopy) together with their PMs (using the Tycho2 catalog); or Mermilliod et al. (2008a), who obtained the mean radial velocities of 166 OCs using the Correlation Radial Velocity (CORAVEL) observations of red giant stars belonging to these systems.

Piskunov et al. (2006) used PMs and RVs from the Catalogue of Open Cluster Data (Kharchenko et al., 2005a,b) within the derived completeness limit of distance to the Sun (0.85 kpc, see Sect. 2.2) to characterize the local kinematics of OCs: Oort's constants, the solar motion, and the velocity ellipsoid are given in their Table 2., and they have values consistent with these obtained for young stars (Cepheids, OB stars) in the Galactic disk.

Wu et al. (2009) analyzed kinematics and calculated orbits in three different axisymmteric Galactic models for a sample of 488 OCs with the initial conditions (current velocity and position vectors) derived mostly from the catalog of Dias et al. (2002a, version 2.9 released in April 2008). By dividing the sample in age bins (younger then 0.5 Gyr, and older than 1 Gyr), they found that each component of velocity dispersion for their sample is higher for the older age bin. This is consistent with Piskunov et al. (2006) and the earlier result of Lyngå & Palouš (1987), who derived the dispersion of radial velocities increasing

with time. The velocity dispersion increasing with age indicates heating of the OCs disk population, similarly as observed for the disk stars (e.g., Binney & Tremaine, 2008).

Clusters orbits were investigated also by Vande Putte et al. (2010), who used a similar sample and initial conditions as Wu et al. (2009) and carried out their integrations in an axisymmetric Galactic model. Since clusters retain the kinematical memory of their origin, Vande Putte et al. (2010) suggested that the orbital parameters of the maximal vertical amplitude (maximal separation from the Galactic plane, $|z|_{\max}$) and eccentricity, e, might be used as indicators of individual clusters origin, finding them correlated with metallicity. They identified several clusters with orbits different from the majority of the sample and with somehow extreme values of the vertical amplitude and eccentricity. They suggested an unusual origin scenarios for these systems (extragalactic origin, origin due to the impact of a high velocity cloud or a GC on the disk, or an origin via some form of merger). Except for these few exceptions (about ten OCs), orbits are found to be close-to-circular with lower value of eccentricity and the vertical amplitude ($e < 0.3$ and $|z|_{\max} < 0.9\,\mathrm{kpc}$).

The kinematic data presented in the catalog of Dias et al. (2002a, and its later versions) were also used to study characteristics of the Galactic thin disk and the spiral arms. Dias & Lépine (2005) derived the spiral pattern angular velocity. They traced the location of spiral arms by backward integrated orbits of a sample of OCs and obtained the location of their birth places as a function of time. They used two methods to find the clusters birth places – first method assumes circular orbits; and the other uses orbits integrated backward in an axisymmetric Galactic potential. Their result confirms that the spiral arms rotate like a rigid pattern, with the angular velocity of about $24\,\mathrm{km\,s^{-1}\,kpc^{-1}}$. Further, assuming that the orbits of OCs can be described by the epicyclic approximation, Lépine et al. (2008) derived the epicycle frequency κ in the Galactic disk. They presented a new method to obtain κ from a correlation between the velocity direction of an object (an OC in this case) on the epicyclic orbit and its age. Therefore, for a given rotation curve they can obtain κ by two independent methods, compare the results and hence check the assumed rotation curve. By this method, they found the circular velocity of $(230 \pm 15)\,\mathrm{km\,s^{-1}}$ and κ of $(43 \pm 5)\,\mathrm{km\,s^{-1}\,kpc^{-1}}$ at the radial range of 7–8 kpc.

2.4 Age, disruption, and lifetime of OCs

Ages of observed OCs have a range of about 1 Myr–10 Gyr. Every star cluster loses mass during its lifetime. The present-day age and mass distribution of OCs is given by their initial mass function (IMF), formation rate, and dissolution rate. Dissolution of a cluster and its disruption time naturally depend on its initial mass and on the environment in which the cluster lives. Many studies of the distribution of ages of OCs have been carried out since the pioneering works of Spitzer (1958), who gave a quantitative theoretical estimates of the disruption time due to clusters interaction with GMCs; and Wielen (1971), who derived a mean dissolution time of 0.2 Gyr from the distribution of clusters age observed within 1 kpc from the Sun (see e.g., Piskunov et al., 2006 or Lamers & Gieles, 2006 for a summary). The understanding and description of various

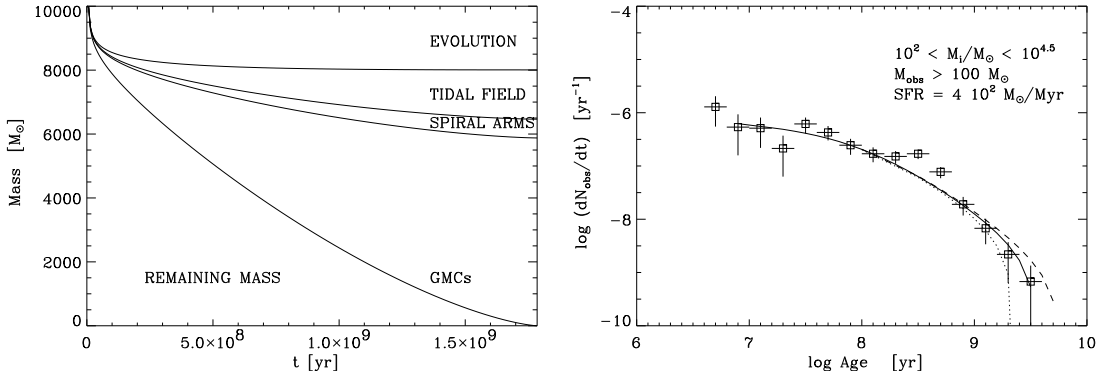

Figure 2.2: *Left*: Mass evolution of a cluster with the initial mass of $10^4\,M_\odot$ living in the solar neighborhood; reproduced from Lamers & Gieles (2006, their Fig. 1). The mass loss due to separate effects of stellar evolution, interaction with the Galactic tidal field, spiral arms shocking, and encounters with GMCs is shown by individual lines. *Right*: Observed age distribution of OCs with mass higher than $100\,M_\odot$ within 600 kpc from the Sun; reproduced from Lamers & Gieles (2006, their Fig. 3). The observed distribution (derived by Lamers et al., 2005, from the catalog of Kharchenko et al., 2005a) is shown by squares and given in units of number of OCs per year. Dotted, full, and dashed lines show the predicted distribution with a cluster star formation rate of $4 \cdot 10^2\,M_\odot\,\mathrm{Myr}^{-1}$ and the maximal initial mass of formed cluster of $1.5 \cdot 10^4$, $3 \cdot 10^4$, and $6 \cdot 10^4\,M_\odot$, respectively.

mechanisms of clusters disruption have significantly improved in the past years. Although a more detailed description of some aspects of these complex topics is given in Sect. 5.3, a complete summary is beyond the scope of this text. Here we focus only on a short description of the most recent and relevant results.

Several mechanisms contribute to the disruption of a star cluster, being differently important during different episodes of cluster lifetime. During the first few 100 Myr the mass loss is dominated by stellar evolution of initially massive stars. The mass fraction that is lost by stellar evolution depends on cluster metallicity and on the adopted IMF (e.g., Lamers et al., 2010).

Mass loss due to tidal disruption is dominant during the later phases of cluster life. It is driven by the two-body relaxation in the galactic tidal field (detailed description given by Baumgardt & Makino, 2003, or Lamers et al., 2005) and by tidal shocks due to interaction with GMCs (Gieles et al., 2006) or with spiral arms (Gieles et al., 2007). Stars in cluster experience a *tidal shock* interaction, when the crossing time of a star in the cluster is much longer compared to the time of the interaction. In such interaction, the cluster gets compressed by the tidal forces and its stars are impulsively heated, they accelerate and some might reach the escape velocity and become unbound. Since the crossing time of a star in cluster increases with its distance from the center of the cluster, stars located in the outer regions of the cluster are more heated. Heating due to the tidal shocks is described by the impulsive approximation (see Gieles et al., 2006 and references therein for more detailed description).

Lamers et al. (2005) presented a simple approximative analytical description of cluster disruption including the mass loss due to two-body relaxation and the stellar evolution. They used the approximation to explain the observed age distribution of OCs in the solar neighborhood. The study was later extended by Lamers & Gieles (2006) who included also the mass loss due to the tidal shocks by spiral arms and encounters with GMCs. Mechanisms of mass loss for a cluster with an initial mass of $10^4\,\mathrm{M}_\odot$ in the solar neighborhood are compared in the left plot of Fig. 2.2, which we adopted from Lamers & Gieles (2006), who conclude: *encounters with GMCs are the dominant dissolution effect contributing about as much the three other effects combined* (referring to the stellar evolution, two-body relaxation, and spiral arms shocking). Naturally, the analytical description of cluster disruption includes various parameters characterizing the cluster itself and the environment in which it lives. Some of the important parameters are: the tidal field strength, characteristics of the spiral pattern (number of arms, their angular velocity, locus and shape, or the mass density of the gas in the spirals), the surface density of a GMC, the mean density of GMCs in the Galactic plane and their velocity dispersion, or the mass density of the cluster (i.e., its mass and radius). Details about various choices of these parameter are discussed in Gieles et al. (2006, 2007), Lamers et al. (2005), or Lamers & Gieles (2006).

Further, to estimate the clusters formation rate and the maximal initial mass of a cluster formed in the solar neighborhood, Lamers & Gieles (2006) compared their theoretical prediction with the observed age distribution of 114 OCs within 600 kpc from the Sun derived from the catalog of Kharchenko et al. (2005a). The theoretical distribution with the cluster star formation rate of $4 \cdot 10^2\,\mathrm{M}_\odot\,\mathrm{Myr}^{-1}$ for clusters in mass range 100–$1.5 \cdot 10^4\,\mathrm{M}_\odot$ reproduces the observed one in the best way (however, they note that the value of the maximal mass is quite uncertain due to questionable completeness for the high age end of the distribution). Both, observed and predicted, distributions are shown in the right plot of Fig. 2.2 (adopted from Lamers et al., 2005) and are in a very good agreement.

2.5 Metallicity gradient in the Galactic disk

Radial abundance gradients are considered to provide important constraints on the understanding of the chemical evolution of the Galactic disk. Since metallicities[4] and solar distances of OCs are relatively easy to measure, OCs have been often used as abundance gradients tracers. They are also covering a relatively large range of metallicities and Galactocentric radii. Despite of the investigation long several decades (the first radial

[4] Metallicity of an object can be measured by the abundance of iron in its matter with respect to the hydrogen, which is often related to that of the Sun. The metallicity is than expressed as

$$[\mathrm{Fe/H}] = \log_{10}\left[\frac{(N_{\mathrm{Fe}}/N_{\mathrm{H}})_\star}{(N_{\mathrm{Fe}}/N_{\mathrm{H}})_\odot}\right],$$

where N_{Fe} and N_{H} are the number of iron and hydrogen atoms per unit volume of the object ($\star$) and the Sun ($\odot$). Metallicity [Fe/H] is a dimensionless quantity, but the unit *dex* is often used (contraction for decimal exponent).

metallicity gradient using OCs was measured by Janes, 1979) and a number of published studies, there are still several unsolved questions about this topic, e.g., the difference of the gradient slope in the inner and the outer parts of the disk, or how the radial abundance gradient evolved with time.

2.5.1 Metallicity versus Galactocentric radius

Though earlier studies were limited by a low number statistic and lower precision of available observations and observational techniques, the negative radial gradient for the metallicity – i.e., the metallicity of OCs is decreasing with their increasing Galactocentric radius – was noticed by all of them. In Table 2.1 we give a summary of studies concerning this topic published till 2003, when higher amount of the high-resolution spectroscopic data started to be available (see also Friel, 1995, for a review of the early studies). The slope of the gradient measured by fitting a linear function has been estimated in a range from about -0.1 to $-0.05\,\mathrm{dex\,kpc^{-1}}$, depending on various details of each study as the used observational methods, size of the OCs sample, or the radial range fitted.

However, a closer inspections of the measured data showed that the basic nature of the radial distribution of OCs metallicity is not as simple as to be described by a single linear function. By dividing their sample into two radial bins (with ranges of 8.5–10, and 10–12.1 kpc), Panagia & Tosi (1981) found that the gradient for the outer bin is steeper than the one for the inner radii. Janes et al. (1988) found different slopes also for different age bins of their sample (using age bins of 0.01–0.2, and 0.2–10 Gyr), with older clusters having steeper gradient than the younger ones. Detailed gradient values found in these studies are given in Table 2.1.

Furthermore, Twarog et al. (1997) suggested that the radial distribution of OCs abundances is described by a step function with discontinuity at about 10 kpc. For radii 6.5–10 kpc their sample shows only a shallow gradient with abundances of individual clusters having a mean value about 0 dex; while beyond the discontinuity at about 10 kpc the mean abundance is about -0.35 dex. Spatial and age variations in the radial gradient were further discussed (usually through dividing the used sample into various age and radial bins) in many other studies, sometimes arriving to contradictory conclusions. In any case, the radial distribution of OCs metallicities is no longer being described by a single linear slope.

As mentioned above, the value of metallicity gradient is obtained by fitting linear functions to (sub)samples of OCs selected using various constrains. However, as noted already by Cameron (1985), since the earlier samples usually contained only a few clusters in the outer disk (with the Galactocentric radii $R > 12$ kpc), such fitting is quite sensitive to points at these extreme radii, especially in the studies using a single linear function fit. Therefore – also keeping in mind the discontinuity at 10 kpc suggested by Twarog et al. (1997) – precise high-resolution spectroscopy of stars, most often in their red giant branch (RGB) stage, in distant OCs in the outer disk, which, at the same time are usually old systems (Sect. 2.2), became of a special interest and importance (e.g., high-resolution studies by Carraro et al., 2004, 2007; Villanova et al., 2005; Sestito et al., 2006, 2008;

Table 2.1: Published values of the radial metallicity gradients of OCs

Reference	d[Fe/H]/dR [dex kpc^{-1}]	R [kpc]	[Fe/H] [dex]	age [Gyr]	#OCs	notes
Janes (1979)	−0.05±0.01	8–14	−0.64–+0.21	0.04–1	41	
Panagia & Tosi (1981)	−0.095±0.034	8.5–12.1		0.008–5.1	20	radial bins, a steeper gradient for the outer OCs
	−0.01±0.05	8.5–10			10	
	−0.13±0.07	10–12.1			10	
Cameron (1985)	−0.11±0.02	6.9–10.9	−0.311–+0.195	0.008–10	38	
Janes et al. (1988)	−0.113	6.5–13.5	−0.7–+0.3	0.01–10	87	age bins, a steeper gradient for the older OCs
	−0.07			< 0.2		
	−0.14			> 0.2		
Friel & Janes (1993)	−0.09±0.02	7.9–14.5	−0.88–+0.19	0.8–8.1	24	
Twarog et al. (1997)	−0.067±0.008 [a]	6.5–15	−0.85–+0.18		75	discontinuity around R of 10 kpc
	−0.023±0.017	< 10	−0.18–+0.19		62	
	−0.004±0.018 [a]	> 10	−0.88–−0.18		13	
Carraro et al. (1998)	−0.085±0.008	7.6–16.0	−0.97–+0.19	0.6–9	37	age bins, no significant changes found
Friel et al. (2002)	−0.059±0.010	7.5–16.4	−0.62–+0.11	0.8–12.6	39	age bins, a slightly steeper gradient for old OCs
Chen et al. (2003)	−0.063±0.008	6.8–23.0	−0.83–+0.46	0.01–12	119	age bins, a steeper for the older OCs (age > 0.8 Gyr); radial bins, a steeper for the outer OCs (R < 10 kpc)

Notes. [(a)] Values without Berkeley 21.

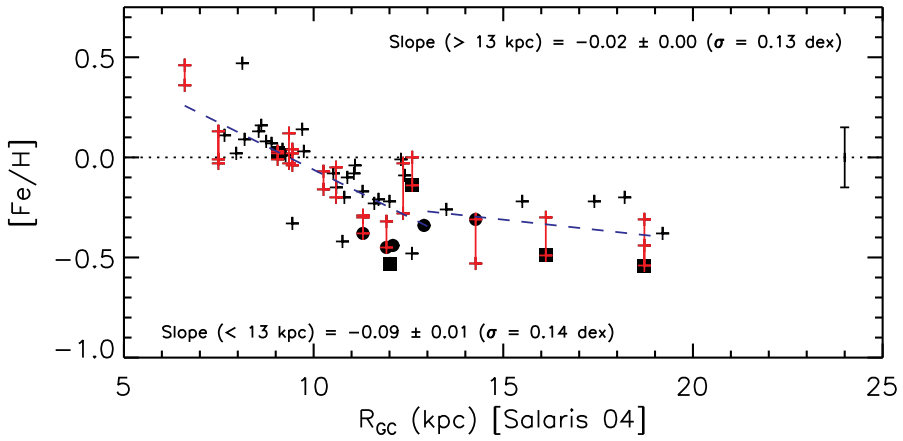

Figure 2.3: Radial distribution of [Fe/H] for OCs; reproduced from Yong et al. (2012, their Fig. 19). Different symbols show data from different sources (filled circles – Yong et al., 2012; filled squares – Yong et al., 2005; plus signs – data from other literature, see Table 13 in Yong et al., 2012). Red plus sign symbols connected by line represent multiple measurements of the same cluster. Slopes of linear fits for radii $R < 13$ kpc and $R > 13$ kpc are given. A representative error-bar is shown in the right part of the plot. Clusters Galactocentric radii are taken from Salaris et al. (2004). The sample consists of 49 clusters.

Bragaglia et al., 2008; Yong et al., 2005, 2012; Jacobson et al., 2008, 2009, 2011b; Friel et al., 2005, 2010).

Using samples containing more of these outer disk clusters, most of the recent studies agree that the radial distribution of OCs metallicity has a spatial transition between the inner and the outer disk located around 12–13 kpc. Combining the high-resolution metallicity measurements from various sources, several authors measured that the metallicity gradient flattens or even become a flat plateau beyond the Galactocentric radii $R \sim 12$–13 kpc, see Yong et al. (2005), Carraro et al. (2004, 2007), Sestito et al. (2008), Magrini et al. (2009), Jacobson et al. (2009, 2011b), Pancino et al. (2010), Friel et al. (2010), Carrera & Pancino (2011), Lépine et al. (2011), or Yong et al. (2012). To illustrate this result, the radial distribution of metallicity from Yong et al. (2012) is reproduced in Fig. 2.3.

Recently, Lépine et al. (2011) suggested an explanation of the step-like shape of the radial metallicity gradient. Using the literature data on OCs (mostly from the catalog of Dias et al., 2002a), they found the change in the gradient at 8.5 kpc, somehow smaller radii than mentioned above (assuming the solar radius of 7.5 kpc). They associate the transition radius with a ring-shaped region of void of gas located at the corotation radius of a long-lived – minimal lifetime of order of 3 Gyr – four-armed spiral pattern (see also Amôres et al., 2009). The rotating spiral arms create a barrier isolating the gas at each of the sides and so the gas is evolving independently in these two regions. However, the stars are scattered and migrated across the disk (blurring and churning, see Sect. 3.2.1 for more detailed description of these mechanisms but note that Lépine et al., 2011 consider the spi-

ral arms long-lived and hence their corotation radius does not change with time). Lépine et al. (2011) further suggested that the star formation in the Galactic disk has a clumpy distribution (implying also an azimuthal metallicity gradient in the disk), happening in a limited number of regions located in the spiral arms and having a specific metallicity. Later, the radius of stars and OCs is changed by the interaction with the spiral pattern. They propose two explanation for the flatness of the gradient in the outer disk: a flow of gas from the corotation due to the interaction with the spiral structure, which is mixing the gas in the outer disk; or that the OCs were formed in the inner region and moved to the outer disk, where the condition for star formation are not fulfilled. The latter is supported by the fact that mostly old OCs are found at larger radii beyond the transition.

The study of Lépine et al. (2011) points out that the spiral structure plays an essential role in the explanation of the observed radial metallicity gradient of OCs. However, many aspects of the mechanism are still not understood, e.g., Sellwood & Binney (2002) or Roškar et al. (2008b) showed that the radial migration due to transient spirals affects gas as well as stars (see Sect. 3.2.1). Moreover, together with the spiral arms, presence of the Galactic bar plays an important role for the mechanisms of radial migration (Sect. 3.2.2).

Time evolution of the radial metallicity gradient

Earlier studies suggested slightly steeper metallicity gradients for older clusters (Janes et al., 1988; Friel et al., 2002; Chen et al., 2003, see Table 2.1) or no significant evidence for time evolution (Carraro et al., 1998). More recently, Magrini et al. (2009) found a similar behavior based on high-resolution spectroscopic data. They do not find any significant time evolution over the past $\sim 10\,\mathrm{Gyr}$ for the outer part ($R > 12\,\mathrm{kpc}$) of the distribution. For the more local part of the disk (7–12 kpc), the gradient is only slightly flatter for the young OCs (ages $\leq 0.8\,\mathrm{Gyr}$ they found the slope of $(-0.053 \pm 0.029)\,\mathrm{dex\,kpc^{-1}}$, while for two older age bins of 0.8–4 and 4–11 Gyr the slope is $(-0.094 \pm 0.008)\,\mathrm{dex\,kpc^{-1}}$ and $(-0.091 \pm 0.006)\,\mathrm{dex\,kpc^{-1}}$, respectively). Flatter slope for younger ages of the inner disk part was also found by Carrera & Pancino (2011), who analyzed a sample of 89 OCs with the metallicity estimates based on high-resolution spectroscopy. Using a sample of 42 OCs, Jacobson et al. (2011b) focused on the transition zone between the inner and the outer disk having 18 clusters with Galactocentric radii in the range of 9–14 kpc. They compared metallicity radial distribution in various age bins and they suggested that the transition might changed its location to larger Galactocentric radii over time (for ages in the range of 0.8–4 Gyr, the transition occurs near or beyond 14 kpc; while for the clusters older than 4 Gyr, it is located at smaller radii of $\sim 10\,\mathrm{kpc}$).

Radial gradient of abundances of other elements

Apart from iron, the abundances of other metals are also measured in OCs,[5] such as the α-elements (O, Mg, Si, Ca, and Ti), the iron peak elements (Mn, Co, Ni), Al, or

[5] These are often measured by the ratio of the given element abundance to that of iron and compared to the same ratio of the Sun, for example, for the oxygen,

$$[\mathrm{O/Fe}] = \log_{10}\left[\frac{(N_\mathrm{O}/N_\mathrm{Fe})_\star}{(N_\mathrm{O}/N_\mathrm{Fe})_\odot}\right],$$

where N_O and N_Fe are the number of oxygen and iron atoms per unit volume of the object ($\star$) and the Sun ($\odot$).

Na. Recent works using the results of the high-resolution spectroscopy usually find no or only weak trends of these abundances with the Galactocentric radius (Friel et al., 2010; Jacobson et al., 2011b; Yong et al., 2012). They also do not find significant differences for the dependencies in the inner and outer disk. Similarly to [Fe/H], no significant time evolution was found for other elements abundances radial distributions. Abundances of individual clusters from different literature sources often have large variations (~ 0.3 dex, Jacobson et al., 2011b). High-quality, homogeneous dataset of abundances of other elements for a larger sample of OCs is needed to measure possible radial and age variations in their distributions.

Comparison with other tracers

The radial metallicity gradients have been measured using several different tracers, Cepheids being among the most popular next to the OCs. With their ages up to ~ 100 Myr, Cepheids represent a young population and they reflect the current chemical composition of the thin disk. Recent studies (e.g., Luck & Lambert, 2011, or Yong et al., 2012, and references therein) find gradient with values around $-0.06\,\mathrm{dex\,kpc^{-1}}$ and no evidence for a change (flattening) in the radial metallicity distribution of Cepheids. However, the dispersion of metallicity beyond the Galactocentric radius of 10 kpc is increased (Luck & Lambert, 2011) and some works even find a discontinuity in the radial metallicity distribution – similar to the one found using OCs (e.g., Pedicelli et al., 2009). Yong et al. (2012) further compared the radial distribution of OCs to the one traced by the field giant stars in the solar neighborhood and found similar trends for both populations.

2.5.2 Metallicity versus the vertical height

Another characteristic of the OCs population that could bring some information about the chemical evolution of the disk, is the behavior of clusters metallicity with their distance from the Galactic plane (given by the absolute value of the vertical cylindrical coordinate, $|z|$). Existence of the vertical gradient can help to distinguish among various scenarios of the thick disk formation (no gradient is expected in the thick disk formed by heating due to accretion or merger events; in contrast to the thick disk formed by the gradual heating of the thin disk). However, a conclusive evidence of the vertical metallicity gradient of OCs is still missing and the literature includes controversial results. Some authors found gradient approximately about $-0.3\,\mathrm{dex\,kpc^{-1}}$, e.g., Piatti et al. (1995), or Chen et al. (2003); others found no significant evidence for the gradient, e.g., Jacobson et al. (2011a), or Carrera & Pancino (2011). Moreover, as noted by Carraro et al. (1998), when estimating the vertical gradient of the OCs, clusters metallicity should first be corrected for the radial and age trends. This was not done in all studies prior to that time and makes the literature comparison difficult.

More recently, Carrera & Pancino (2011) investigated the vertical gradient for their sample of 89 OCs. They corrected the contribution of the radial gradient and investigated the vertical gradients in four annuli with different Galactocentric radii. Except for the expected increased number of OCs with higher vertical distance in the outer annuli (with

R of 10–13 kpc, and $R > 13$ kpc), they do not find any convincing vertical gradient in either of the radial annuli.

2.5.3 Age–metallicity relation

Apart from the metallicity trends with the Galactocentric radius or the vertical height, the age–metallicity relation (AMR) of OCs was also investigated since the ages and metallicities of enough numerous sample started to be available. The earlier studies, which observed the radial metallicity gradient as a simple linear slope, obtained the AMR at the solar radius through the correction of metallicities from various radii by the measured radial gradient. However, in contrast to the radial abundance gradient clearly found in all of these early studies, OCs seemed to show no relation between their age and metallicity, unlike the field stars (Cameron, 1985, Friel & Janes, 1993, see Friel, 1995, for a summary of results available by that time).

Later, Carraro et al. (1998) found the AMR measured from their sample to be consistent with the one for the nearby stars, both showing similar *trend* having a rather large scatter in their metallicity for all ages up to 9 Gyr (e.g., Edvardsson et al., 1993, see also Sect. 3.1). However, they also mentioned the sensitivity of the metallicity correction to the possible time dependence of the radial metallicity gradient. The influence of the time dependent radial gradient on the AMR of OCs is also discussed by Friel et al. (2002), who confirm no clear correlation between age and metallicity derived from their sample. Similar result was also reached by Chen et al. (2003) and Yong et al. (2005). This lead to a conclusion that for the metallicity of OCs, their birth radii (considered the same as their present-day observed radial location) is more important than their age (Friel et al., 2002); or that possibly the stars in OCs could be of different stellar population with different origin and chemical enrichment than the field stars (Yong et al., 2005).

Extending the clusters sample by five old systems in the outer disk, Carraro et al. (2007) confirmed the lack of AMR for OCs. They found no clear relation among clusters having metallicities with a spread of about 0.4 dex for all ages in their sample (0.8 – 5 Gyr). Using a compilation of 57 clusters, Pancino et al. (2010) suggested that there might be a very weak trend in their AMR with a slope *very gentle at most still compatible with no trends at all.* Similarly, Yong et al. (2012) found no significant trend in their age versus metallicity distribution based on 48 OCs.

To sum up, the number of systems having metallicities (and abundances of other elements) derived from a precise high-resolution spectroscopy have significantly increased in the recent years. There are several working groups obtaining and analyzing these data, and a big progress have been made in the field of the disk chemical evolution as traced by OCs. However, many questions remain to be answered and more observational as well as theoretical effort is needed to better understand these interesting and complex problems.

Table 2.2: Metallicity of NGC 6791 from different spectroscopic studies.[a]

Reference	[Fe/H]	Stars used
Worthey & Jowett (2003)	+0.320±0.023	24 RGB, RC
Origlia et al. (2006)	+0.35±0.02	6 RGB
Carraro et al. (2006)	+0.39±0.05	10 RGB, RC
Gratton et al. (2006)	+0.47±(0.04, 0.08) [b]	4 RC
Boesgaard et al. (2009)	+0.30±0.08	2 turn-off

Notes. [(a)] All listed studies used a high-resolution spectroscopy except for the mid-resolution measurements of Worthey & Jowett (2003). [(b)] Two error estimates represent random and systematic terms respectively.

2.6 The case of NGC 6791

NGC 6791 is unique in the Galactic system of OCs from several points of view – it is very old, metal-rich, massive, and it shows several interesting features not observed in any other OC. Due to its unique properties, NGC 6791 has been subject of many observational and theoretical studies. In this section, we (not exhaustively) review the cluster characteristics and relevant references.

2.6.1 Basic characteristics

NGC 6791 is found in the constellation of Lyra (upper image of Fig. 2.4). The cluster location within the MW is at 4 kpc from the Sun, close to the solar circle, at 8 kpc from the Galactic center and about 0.8 kpc above the Galactic plane (derived from Brogaard et al., 2011, see Sect. 5.1.1 and Table 5.1 for details). The first photometric study of the cluster was made by Kinman (1965) and many others followed since than. The color–magnitude diagram (CMD) of NGC 6791 is complex, showing several puzzling features, some of which are discussed below. Using a comprehensive photometry and PMs, Platais et al. (2011) made a membership analysis for stars down to $g' \sim 22$ mag. They estimated the total mass of the cluster to be $5000\,M_\odot$ and the tidal radius $(23.1 \pm 1.0)'$. An older estimate of the cluster mass was made by Kaluzny & Udalski (1992), who obtained a lower-limit value of about $4000\,M_\odot$.

NGC 6791 is one of four OCs in the field of view of the NASA *Kepler* mission (Gilliland et al., 2010) designed to discover transiting exoplanets. The data collected by *Kepler* lead to several astroseismological studies of stars in NGC 6791, e.g., Basu et al. (2011) or Miglio et al. (2012).

2.6.2 Metallicity of NGC 6791

The cluster metallicity has been subject of several studies since the mid-80s (starting with Janes, 1984). Taylor (2001) critically revised earlier metallicity estimates published

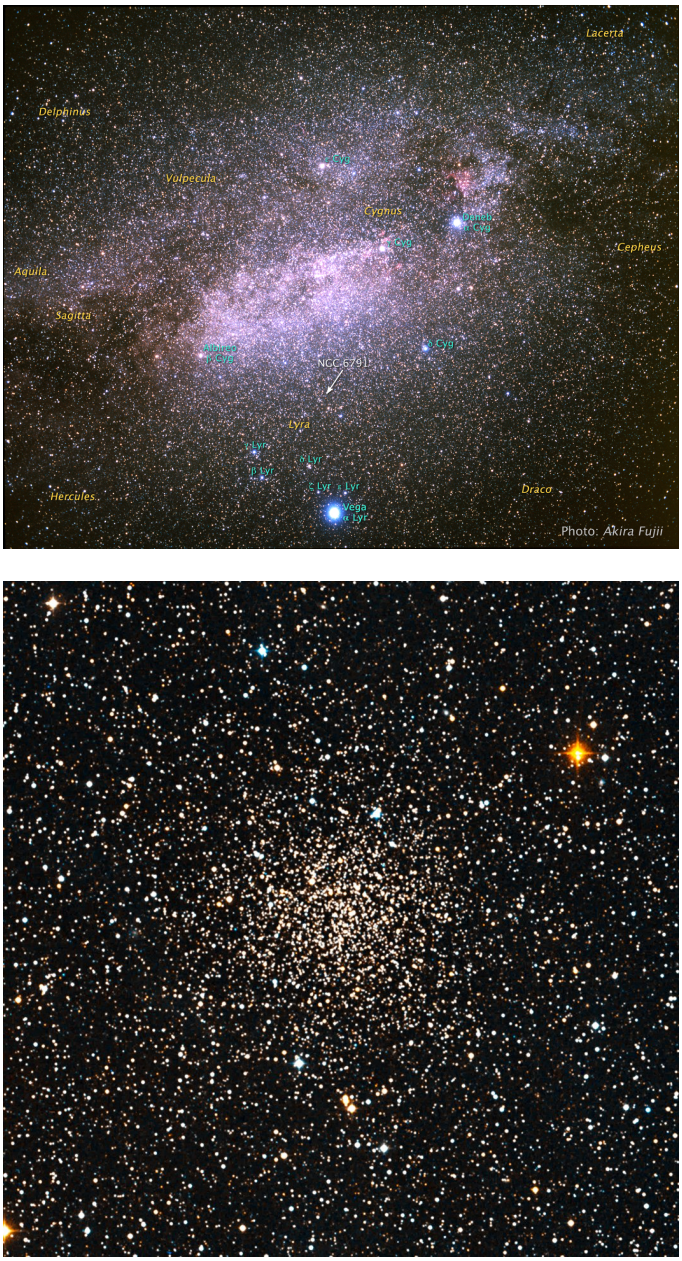

Figure 2.4: Ground-based view of NGC 6791. *Up:* Location of the cluster on the night sky (field of view of 45° × 35°, centered on the constellation of Cygnus). Names of constellations and of several bright stars are marked. NGC 6791 can be found in Lyra. Credit: NASA, ESA, A. Fujii, and Z. Levay (STScI). *Bottom:* NGC 6791 (field of view $25' \times 25'$). Credit: Digitized Sky Survey (DSS), STScI/AURA, Palomar/Caltech, UK-STU/AAO. Both images are taken from the HubbleSite News Release Archive, Number: STScI-2008-25, Credit: NASA, ESA, L. Bedin (STScI).

during the period 1984–1999, concluding that: *the metallicity of NGC 6791 is somewhere between +0.16 and +0.44 dex*, with some results clearly indicating extreme values, though, a significant spread among different studies is present. Some more recent results using accurate high-resolution spectroscopy of cluster stars in various evolutionary stages reached generally more consistent values. We give a summary of these results in Table 2.2. Apart from the spectroscopy, the metallicity was also measured using the color-metallicity relations for the CCD photometry by Anthony-Twarog et al. (2007) obtaining $[\mathrm{Fe/H}] = (+0.45 \pm 0.04)$ dex, a value consistent with the high-resolution spectroscopic results (Table 2.2). In summary, NGC 6791 has extremely high metallicity, [Fe/H] $\sim +0.4$ dex and belongs among the most metal-rich OCs (see Fig. 2.3, where metallicities obtained from high-resolution spectroscopy for 49 OCs are indicated).

2.6.3 Age, reddening, and distance modulus

The age of NGC 6791 has been measured by many authors using the classical method of the CMD isochrone fitting. From these results there is no doubt that the cluster belongs to the oldest known OCs. However, the isochrone method is sensitive to the used model of stellar evolution and it requires estimates of reddening and distance modulus. The scatter in these parameters obtained in the last three decades is quite large: for reddening and distance modulus, 0.09–0.225 and 12.66–13.6 respectively, resulting in age estimates in the range of 6–12.5 Gyr (e.g., Anthony-Twarog & Twarog, 1985; Kaluzny, 1990; Demarque et al., 1992; Meynet et al., 1993; Carraro et al., 1994; Montgomery et al., 1994; Tripicco et al., 1995; Kaluzny & Rucinski, 1995; Chaboyer et al., 1999; Salaris et al., 2004, see, e.g., King et al., 2005 or Anthony-Twarog et al., 2007 for a summary on various references).

In principle, it is not easy to constrain the precise age of a cluster based only on the isochrone fitting method, although several up-to-date studies tend to converge on a value around 8 Gyr (Carney et al., 2005; King et al., 2005; Carraro et al., 2006; Anthony-Twarog et al., 2007). Recently, reddening and distance independent age estimates based on observations of detached eclipsing binary cluster members were published by Grundahl et al. (2008) and Brogaard et al. (2012) (see also Brogaard et al., 2011), both giving results around 8 Gyr. Another independent age estimate by García-Berro et al. (2010) coming from the method of white dwarf (WD) cooling sequence gives value about 8 Gyr, consistent with the above mentioned results (see Sect. 2.6.4 for details about the cluster WD population). Yet a different method for age determination was investigated by Basu et al. (2011), who used the astroseismic data of 34 RGB cluster stars observed by the NASA *Kepler* mission to obtain their ages (the method requires the knowledge of reddening and metallicity) and found ages between 6.8 and 8.6 Gyr, with the most models giving age around 7 Gyr.

Therefore, let us conclude that NGC 6791 is about 8 Gyr old and it belongs to one of the oldest OCs known (see Sect. 2.4 and also Fig. 2.2). For our later investigation (Sect. 5.1.1), we adopt the distance modulus given by Brogaard et al., 2011 (and also Brogaard et al., 2012), which leads to the cluster solar distance of (4.01 ± 0.14) kpc.

2.6.4 Peculiarities in the CMD

The white dwarf population

The WD population of NGC 6791 was observed for the first time by Bedin et al. (2005). Studying the WD luminosity distribution they obtained the cooling sequence below 3 Gyr, in a significant contrast to the turn-off point age estimates of about 8 Gyr (Sect. 2.6.3). To explain this discrepancy, Hansen (2005) suggested that NGC 6791 contains He-core WDs with a significantly longer cooling time scales compared to the classical CO-core WDs. He-core WDs might be result of an enhanced mass loss of stars in their RGB phase, which is caused by the high metallicity of the cluster. This scenario was further supported by Kalirai et al. (2007), who found part (about two-thirds) of the cluster WD population to have masses lower then the He-core flash limit (and so these stars could not start burning He in their cores and later result to classical CO-core WDs).

However, Bedin et al. (2008a) observed an extended double-peaked WD luminosity distribution. In the classical CO-core WD picture, each of the luminosity distribution peaks corresponds to the WDs with a different age (about 4 and 6 Gyr). Bedin et al. (2008b) demonstrated that this shape of the luminosity distribution can be explained if a significant fraction (about one third) of WDs is actually in binaries. Van Loon et al. (2008) used the Spitzer Space Telescope infrared photometry to search for the evidences of an enhanced mass loss of the RGB stars – circumstellar dust, differences in the observed and theoretical (without an enhanced mass loss) luminosity distributions – but they found neither of these, concluding that there is no evidence for a high mass loss of the RGB stars in the cluster. García-Berro et al. (2010) presented a complex modeling of the classical CO-core WD cooling, which led to a significant increase of the cooling age, resolving the age discrepancy without the necessity for the He-core WDs.

The WD binary population as an explanation of the double-peaked WD luminosity distribution was further favored by theoretical study of the evolutionary cooling sequences by García-Berro et al. (2011), who did not find any evidence for a substantial fraction of He core WDs in NGC 6791. Moreover, using the stellar masses obtained from astroseismology measured by the NASA *Kepler* mission, Miglio et al. (2012) estimated the mass loss during the RGB stage to be rather small and insufficient for the formation of a significant number of He-core WDs.

Extreme horizontal branch stars and the UV upturn

Many extreme horizontal branch (HB) stars were discovered in the cluster (Kaluzny & Udalski, 1992; Liebert et al., 1994; Kaluzny & Rucinski, 1995; Buson et al., 2006; Buzzoni et al., 2012). Number of observational and theoretical studies have been made to understand the details about these stars and their formation, see, e.g., D'Cruz et al. (1996), Maxted et al. (2001), or Heber (2009), and references therein. Briefly, stars in the extreme HB stage are hot subdwarfs of B and O type (with effective temperatures more than $3 \cdot 10^4$ K), He-core burning, with masses of about $0.5\,M_\odot$, and with tiny H envelopes (too thin to sustain H burning). It is believed that they result from low-mass stars that experienced an enhanced mass loss (probably due to some kind of interaction in

binaries) that removes all but a tiny fraction of their H envelope during the RGB phase. Hot subdwarfs in the extreme HB phase burn He in their cores under high temperatures and produce a large amount of UV flux.

The UV upturn (or UV excess) is an excess in the far UV part of the spectral energy distribution (with a wavelength shorter then 2500 Å) and is observed in some elliptical galaxies and spiral bulges (including the MW one). Hot subdwarf stars are commonly suggested as an explanation of this phenomenon and therefore the UV flux was unexpected in the early-type systems, which are supposed to be composed of old, red stars. Recently, Buzzoni et al. (2012) measured a significant UV upturn also in the spectral energy distribution of NGC 6791, as in the only case among the Galactic OCs.

Possible prolonged star formation

Twarog et al. (2011) analyzed the CMD of NGC 6791 based on the photometric database compiled by Stetson et al. (2003). The upper main sequence (MS) and the turn-off region of the cluster were found much wider than expected from the photometric errors and binary stars. By separating the stars lying inside the cluster core and outside it, they found that the inner stars occupy the red edge of the upper MS, while the outer stars occupy the blue edge. Twarog et al. (2011) suggested a possible explanations for this occurrence: an age spread of about 1 Gyr between the stars in the inner and the outer regions of the cluster, in the sense that the inner stars formed before the outer stars. However, an explanation by a variable reddening cannot be excluded either.

2.6.5 Abundance spread

While the RGB of NGC 6791 is broad in color (Janes, 1984), statistically significant evidence for an abundance spread within the cluster – which would support a self-enrichment scenario – has been reported only very recently by Geisler et al. (2012). Using high S/N spectra of 21 member stars of different evolutionary stages – lower and upper RGB, red clump, and asymptotic giant branch (AGB) stars – they found that NGC 6791 shows an intrinsic spread in its O and Na content. Figure 2.5 reproduces their results. The Na distribution exhibits bimodality, and moreover, the Na-rich group seems to follow the Na–O anti-correlation trend typically observed in GCs (the red curve in Fig. 2.5, see Sect. 2.7 for more details on the Na–O anti-correlation observed in GCs). While, on the other hand, the Na-poor group has similar abundances as observed for the field stars (green circles in Fig. 2.5).

With these results of Geisler et al. (2012), NGC 6791 became the first OC with observed intrinsic spread in any element. On the other hand, this phenomena is commonly observed in the Galactic GCs (Sect. 2.7), which makes the classification of the NGC 6791 system quite confusing. To better understand a possible implications of the described observational characteristics for the evolution history of NGC 6791, a brief summary of the nowadays understanding of the abundance variations in GCs is reviewed in Sect. 2.7.

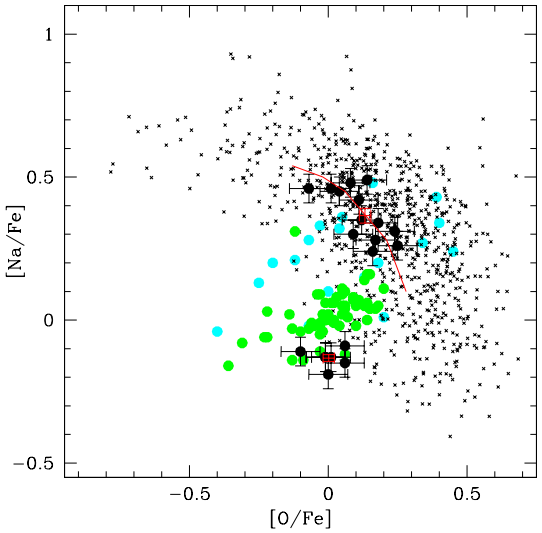

Figure 2.5: Comparison of the [Na/Fe] versus [O/Fe] abundances in NGC 6791 and other objects; reproduced from Geisler et al. (2012, their Fig. 4b). Individual stars in NGC 6791 as observed by Geisler et al. (2012) – black circles with error-bars; abundances of red giant stars in GCs from Carretta et al. (2009) – black crosses; metal-rich (with [Fe/H] > -0.2) field stars from Reddy et al. (2003, 2006) – green circles; mean values for OCs from de Silva et al. (2009, see references therin) – blue circles; mean GCs Na-O anti-correlation – red curve; mean values for the two populations in NGC 6791 with uncertainty – red crossed with error-bars.

2.6.6 Origin of NGC 6791

The wealth of unique properties of NGC 6791 clearly poses the basic question of the origin of this system. Basically, three main theories have been suggested so far.

- The inner disk origin: the inner disk, close to the Galactic bulge, is a high-density region where the star formation is very efficient and the metal enrichment fast (Bensby et al., 2010). Therefore, a system with characteristics similar to NGC 6791 could have formed in the inner regions of the MW about 8 Gyr ago and then migrated outward, to its current location. A brief summary of migration mechanisms, which could influence the cluster orbit is given in Sect. 3. The main goal of Sect. 5 than is to investigate this scenario more in detail.

- The extra-galactic origin: Carraro et al. (2006) suggested that NGC 6791 could be a left-over of a dwarf elliptical galaxy that was engulfed by the MW some time ago and lost most of its mass by the tidal interaction. This scenario seems to be supported by the extreme HB stars and UV upturn measured in the system (Sect. 2.6.4).

- The origin due to the impact of a GC: Based on their study of NGC 6791 orbital parameters, Vande Putte et al. (2010) suggested that the cluster might result from

a gas compression caused by the impact of a GC on the Galactic disk. An OC originating from such mechanism is expected to have its metallicity similar to the disk. Vande Putte et al. (2010) based their suggestion on the NGC 6791 metallicity value of $(+0.11 \pm 0.10)$ dex (listed in the catalog of Dias et al., 2002a, V2.10, released on February 2009), originally obtained by Friel et al. (2002) using a medium-resolution spectroscopy of 39 cluster member stars. However, more recent metallicity estimates based on the high-resolution spectroscopy favor somehow higher value about +0.4 dex (Sect. 2.6.2, Table 2.2), which makes this scenario less probable.

The study of the orbit of NGC 6791 did not reveal much to clarify the origin so far. Depending on the quality of the available kinematic data, backward calculation could produce different orbits – a regular orbits with different eccentricities $e \sim 0.5$ or ~ 0.3 by Bedin et al. (2006), and Wu et al. (2009), respectively, both reaching Galactocentric radii of ~ 10 kpc; or an orbit by Carraro et al. (2006) extending to more than 20 kpc in the Galactic disk (see Sect. 5.1.3 for a more detailed comparison of the published studies of the cluster orbit). The aim of Sect. 5 is to obtain the orbit of NGC 6791 using the most up-to-date kinematic data and to investigate the possible origin of the current orbit through a particular kind of the radial migration mechanisms.

Another important point to consider in the context of the cluster origin and evolution scenarios is a significant mass loss that the system must have experienced experience during its lifetime of about 8 Gyr. The cluster was originally much more massive than its current mass of about $5000\,M_\odot$ (Sect. 2.6.1). This aspect is briefly investigated in Sect. 5.3.

2.7 Multiple stellar generations in GCs

GCs have long been considered as good examples of a single stellar population systems. However, star-to-star variations in the abundances of light elements (e.g., C, N, O, Na, Mg, Al, or F) were discovered already in the late 70s (Cohen, 1978). A spread in the light elements abundances can be found even when the Fe abundance is observed to be homogeneous among the stars in a single cluster. Moreover, an anti-correlation between the abundances of O and the one of Na (O–Na anti-correlation) has been found in most of the MW GCs surveyed (see black crosses in Fig. 2.5 that mark the abundances of red giants in 15 GCs observed by Carretta et al., 2009). Al–Mg anti-correlation has also been discovered in some GCs.

Moreover, multiple sequences were recently observed in the CMDs of several GCs. The first and probably the most known example of such cluster is the most massive Galactic GC – ω Centauri (e.g., Bedin et al., 2004; Villanova et al., 2007; Bellini et al., 2010b, and references therein). Two (and later even three) separated MSs – the blue and the red sequence – were found in the CMD based on the high accurate Hubble Space Telescope (HST) photometry. Furthermore, spectroscopic analysis of Piotto et al. (2005) showed that the stars of the blue sequence are of about +0.3 dex more metal-rich then the stars belonging to the red sequence. Few more GCs (NGC 2808, NGC 6388, or NGC 6441) with photometrically distinguishable multiple stellar populations have been observed by

today. With their present-day masses greater then $10^6\,M_\odot$, all these examples belong to the most massive GCs observed in the MW.

The rich, intermediate-age star clusters of the Magellanic Clouds do not seem to be an exception (Milone et al., 2009), although in this case signatures of prolonged star formation are more common than evidences of discrete episodes of star formation. In the CMDs of Magellanic Clouds clusters the MS is much broader than expected from the photometric errors and binary stars, but does not separate into discrete sequences unlike in the Galactic globulars.

Accepted explanation for the observed anti-correlations is that they are generated via proton capture reactions of the CNO, NeNa, and MgAl chains at high temperatures (in hot H-burning environment). The high temperature necessary for these processes occurs in stellar interiors of stars massive enough. However, since the Na–O anti-correlation is found also in the unevolved low-mass stars (observed for the first time in NGC 6752 by Gratton et al., 2001), which cannot reach such temperatures, their material must have originated in other (more massive) stars of some previous generation. This requires that the stars in GCs form in more than one generation. The second generation of stars forms from material polluted by the gaseous ejecta of the first – primordial – generation of stars. Discrete episodes of star formation could also explain the multiple sequences observed in CMDs of some GCs.

Number of observational and theoretical studies of the multiple stellar generations phenomena have been made and their comprehensive summary is beyond the scope of this thesis. The topic has been reviewed several times, e.g., by Gratton et al. (2004, 2012), where we refer the reader for further details and references. Here we give only a very brief information needed to see the NGC 6791 properties in a wider context. To sum up, the stars in GCs of various evolutionary stages show observational signatures of multiple stellar populations (spectroscopic and/or photometric). The single stellar population picture is no more sufficient to explain the formation and evolution of these complex systems and the idea of the multiple generation scenario is nowadays generally accepted. However, details of this scenario are still not completely understood. For example, an issue under discussion is the nature of the first generation polluters. Two most popular candidates are AGB stars, with time scale for the secondary star formation $\sim$30–300 Myr; and fast rotating massive stars (FRMS), with shorter time scale of few Myr; although the AGB scenario is favored by some recent studies (see, e.g., Renzini, 2008, for a comparison). Other still unsolved questions of the multiple generation scenario are: the initial mass of systems and the form of their IMF, formation of peculiar objects observed in GCs (for example of the blue stragglers, see Glebbeek et al., 2010), or the role of binaries and their fraction.

Theoretical studies need to satisfy a number of observational constrains and explain the variety of observed characteristics among GCs. One of the important issues is that the observed mass of the residual first generation stars is much less then the second generation one (e.g., Carretta et al., 2009, and references therein). Both of the most accepted first generation polluters (AGB stars and FRMS) in combination with the classical IMF do not eject sufficient amount of gas to produce enough of the second generation stars (Gratton et al., 2012, and references therein). A possible solution to overcome this contrast

is that GCs were originally much more massive (10–100 times) systems then observed today and most of the first generation stars were preferentially lost. This scenario was theoretically investigated by, e.g., D'Ercole et al. (2008), Bekki (2011), Vesperini et al. (2010), or Valcarce & Catelan (2011). These studies also show, that the initial mass of the system, $M_{\rm ini}$, is a crucial characteristic that determines how much of the ejecta of the first generation stars the system is able to retain and how efficiently is later transformed to the second generation stars. The initial mass then consequently determines the different abundance variations which can be observed in systems with different present-day mass. Bekki (2011) examined the scenario, where GCs are born in larger systems (Galactic building blocs, as massive dwarf galaxies, later destroyed during the Galactic evolution) and set the theoretical limiting cluster initial mass of $(6\text{–}10) \cdot 10^5\,\mathrm{M}_\odot$, to be the mass necessary for the system to form the second stellar generation and consequently to show the abundance spread in its light elements. This threshold mass is roughly consistent with other theoretical study by Vesperini et al. (2010) who obtained a slightly lower value of $10^{4.8}$–$10^5\,\mathrm{M}_\odot$.

Chapter 3

Radial migration

One of the suggested scenarios for the origin of the peculiar open cluster NGC 6791 is that the cluster have formed in the inner Galactic disk regions and later it was migrated outward in the disk to its current location (Sect. 2.6.6). More generally, it seems that *radial migration* plays an important role in the evolution of the disk galaxies. Several mechanisms causing radial migration are known. In this chapter, we give a brief literature summary on this topic.

3.1 Classical picture of the Galactic disk evolution

The classical understanding of characteristics and radial distribution of stars in the Galactic disk was based the on the assumption that stars are formed *in situ*, i.e., they are born mostly on circular orbits and they stay moving on them for the most of their life. However, it has been observed that the kinematics of stars in the solar neighborhood systematically varies with age (stellar type) – the velocity dispersions of generally younger groups of stars are smaller than of the older stars (e.g., Wielen, 1974 and references therein). These correlations have been described through the diffusion of stellar orbits in the velocity space caused by local irregularities and fluctuations in the Galactic gravitational field (interaction and scattering by the GMCs or transient spiral arms). Wielen (1977) found that a star located in the solar neighborhood can change its velocity by more than $10\,\mathrm{km\,s^{-1}}$ with respect to its unperturbed regular orbit on a time scale of 200 Myr (approximately the same time as its revolution around the Galactic center). Such a diffusion in the velocity space results into a change in the position of the star of about 1.5 kpc.

This picture of stars on diffused stellar orbits, increasing their non-circularity with age, and the *inside-out* scenario of the formation of the Galactic disk are the key ideas of the classical models of the chemical evolution of the disk. In the inside-out scenario of disk formation, the central regions are formed first, with an earlier star formation and a faster chemical enrichment than the outer disk regions. The outer disk is formed later by infall

of gas and the abundances of heavy elements are decreasing with Galactocentric radius (having negative metallicity gradients). The evolution of the disk is further influenced by gas infall and radial flows, which can make the metallicity gradient more shallow.

The classical models of the thin disk chemical evolution assume that the disk can be divided into concentric cylindrical annuli evolving independently of each other (e.g., Matteucci & Francois, 1989; Chiappini et al., 1997, 2001 and references therein). The disk is formed by infalling gas (from the halo, interstellar medium of the thick disk, and from the intergalactic medium). The time scale of the formation is assumed to be a function of Galactocentric distance which produce an inside-out formation where the inner disk parts (inner annuli) evolve faster than the outer regions (outer annuli). The infalling gas has a low metallicity. Over time, stars form from the gas in individual annuli, evolve, and finally enhance the remaining gas with heavy elements. The annuli have width approximately equal to the characteristic length of the orbital diffusion (2 kpc in Chiappini et al., 1997) and they do not exchange material between each other. This leads to the formation of a radial metallicity gradient in the disk, which is generally moderated, for example, by further gas infall from the intergalactic space.

The gas within any annuli is assumed to be well mixed at any time and so each star at the given annuli has metallicity corresponding to the composition of the gas at the moment of the formation of the star. Since the material (neither stars nor gas) does not exchange between annuli, this predicts that a relation between age and metallicity should be present at given radius in the disk. However, it has been found by Edvardsson et al. (1993) that the stars in the solar neighborhood do not show any tight AMR but rather a considerable scatter of metallicities at all ages (for stars of the solar age, the scatter is about 0.24 dex, Wielen et al., 1996). A possible explanation of this spread in the AMR is that the disk stars can change their Galactocentric radius more than predicted by the epicyclic approximation for close-to-circular orbits (so-called *blurring*, see Sect. 3.2.1) and by the orbital diffusion (Wielen, 1977). This was suggested and confirmed by Wielen et al. (1996), who investigated the initial Galactocentric radius of the Sun. Based on the anomalous metallicity of the Sun, which is of about 0.17 dex higher than observed for the nearby stars of the same age, and assuming the presence of a radial metallicity gradient of stars formed in the same time, they found that the Sun was migrated outward from its birth radius by (1.9 ± 0.9) kpc. Since the solar metallicity anomaly lies well within the observed spread of metallicities of the stars of a similar age and location, such a change in Galactocentric radius should be rather typical. Below, we continue with a more detailed description of known physical mechanisms causing these changes and their consequences for the evolution of the Galactic disk and galactic disks in general.

3.2 Radial migration in galactic disks

The change of the mean orbital radius (also called *home radius*) of a star (or other object living in the Galactic disk, such as a star cluster or a GMC) without any significant dynamical heating (i.e., without dramatic increase in eccentricity or inclination) is called radial migration.

3.2.1 Radial migration due to transient spirals

In their seminal work, Sellwood & Binney (2002) described radial migration mechanism due to transient spiral waves in disks. Firstly, they theoretically derived and confirmed using an N-body simulation, that in the disk with a single spiral mode, the z-component of angular momentum of a star (or gas) on a close-to-circular orbit corotating with the spiral can change, while its radial kinetic energy does not change to the first order. In other words, at the corotation radius of spirals, the mean orbital radius of a star can change while there is there is no (or only a little) increase in its random motion and the star still follows close-to-circular orbit, however, with a different mean orbital radius. Star moving on a more general orbit is scattered in a more general way and changes of its z-component of angular momentum are accompanied by changes of its radial kinetic energy; if these stars are on close-to-circular orbits, they are scattered into non-circular orbits. Furthermore, simulation of Sellwood & Binney (2002) showed that the angular momentum change at the corotation happens symmetrically – the particles are transfered from one side of the corotation radius to the other at similar rates – and hence there is no significant change in the overall angular momentum distribution. A more general simulation developing a succession of transient spirals, each of them swapping orbits around its corotation, led to the overall *churning* of the disk (stars and gas), when stars can migrate significant distances in the disk (2–3 kpc) while remaining on close-to-circular orbits. Such a radial migration has an important implications for the classical view of the chemical evolution of disks, e.g., it is expected to flatten any metallicity gradient within the disk and to erase the AMR.

Roškar et al. (2008a) presented results of a high-resolution SPH (smoothed particle hydrodynamics) simulations of isolated MW-like spiral galaxy formation (without a strong central bar). They focused on the disk outskirts and showed that an exponential surface density profile with a break associated with a rapid decrease of gas surface density and of star formation is formed fast. Such a downward bending profile (Type II in the classical Freeman, 1970 classification) further persists during the simulation and the outer disk is populated by stars that have migrated there from the inner disk due to the transient spirals. Further, by mapping the surface density of cool gas, they confirmed that the cool gas also participates in the radial migration.

The same simulation as in Roškar et al. (2008a) was further investigated by Roškar et al. (2008b) who described more consequences of the radial migration due to transient spiral arms. They focused on the stars in the *solar neighborhood* (region between radii of 7 and 9 kpc), summarizing that *roughly 50% of all 'solar neighborhood' stars have come from elsewhere, primarily from the disk interior*. The radial migration substantially alters the properties of stars in the solar neighborhood with respect to the classical view assuming that most of the stars remain at the same disk radii throughout their lifetime. Significant changes of radii result in flattening of the AMR and increasing of its dispersion, and in a broadening of the metallicity distribution function in the solar neighborhood.

Schönrich & Binney (2009) extended the classical chemical evolution models of the MW to include the radial migration of stars and gas in the disk. Following Sellwood & Binney (2002), they introduced terminology to classify the changes in the radial position

of stars and gas: the changes in epicycle amplitude of orbit lead to *blurring*; while changes of the angular momentum of orbit cause *churning*. Their model accounts for both these processes by introducing a certain exchange of stars and gas between the disk annuli (see Sect. 3.1). The model provides a good fit of the metallicity distribution of the solar neighborhood stars (based on the Geneva–Copenhagen survey).

The character of the spiral pattern in galactic disks – long-lived spiral arms; recurrent, transient spiral arms; or possibly a combination of both these modes – is still under discussion (see, e.g., Binney & Tremaine, 2008 or Foyle et al., 2011 and references therein). Lépine et al. (2003) investigated the radial migration at the corotation radius of a long-lived spiral pattern (i.e., the mechanism described by Sellwood & Binney, 2002, for a single spiral mode). They focused on the MW with a single steadily rotating spiral arms with the corotation radius close to the solar circle (8.5 kpc) and confirmed that stars are migrated around the corotation radius, with the radial change of ∼2–3 kpc *in a time of ∼1 Gyr or even much less*. Using a 2-dimensional test-particle integrations in the Galactic plane, they further investigated the evolution of originally linear radial abundance gradient finding that a plateau of flat abundance distribution forms around the corotation radius (7.5–11 kpc). The study of Lépine et al. (2003) was further extended by Lépine et al. (2011), see Sect. 2.5.1 for detailed description.

3.2.2 Radial migration due to resonance overlap

Quillen (2003) showed that the presence of two non-axisymmetric perturbations rotating with different angular velocities can induce a chaotic orbits in a galactic disk, especially close to the resonant radii of one of the rotating pattern. Further, through their direct numerical integrations of test-particles initially on close-to-circular orbits, Minchev & Quillen (2006) studied the radial heating (increase of the radial velocity dispersion) in a disk with multiple spiral patterns (two-armed and weaker four-armed). They found that the effect of the non-axisymmetric perturbations is not summed up linearly – the radial heating present in the case of multiple patterns is higher than the one resulting from adding up the heatings present in the cases of single spiral pattern. The heating also spreads in a wider range of radii compared to the cases of single perturbations. The authors also found that the coupling of two spiral perturbations causes a radial diffusion of particles.

The role of multiple rotating patterns for radial migration have been further described by Minchev & Famaey (2010). Using a test-particles on originally close-to-circular orbits in various 2-dimensional gravitational potential models – including a single steady-state non-axisymmetric perturbation (bar or spiral arms); or two perturbations together, each steady-state and each rotating with a different angular velocity – they mapped the angular momentum change induced in the disk. The amplitudes of the non-axisymmetric perturbations were grown during the time of 0.4 Gyr at the beginning of the calculations and were in other respects time independent (with constant angular velocities). Firstly, Minchev & Famaey (2010) showed that in the cases with a single perturbation, a significant angular momentum changes occur only in the regions near the corotation radius of the given perturbation. This radial migration mechanism is similar to the one de-

scribed by Sellwood & Binney (2002) for the case of a single spiral mode. However, when both bar and spiral arms are present in the disk, the angular momentum changes occur not only close to the corotation radii of each of the perturbations, but they basically spread throughout the whole disk. The distribution of the change of angular momentum is found bimodal, with peaks close to the corotation of the bar and its outer Limdblad resonance (regardless the pattern speed of the spiral arms). Important characteristics of the radial migration due to resonance overlap are that the effects of individual rotating perturbations add up nonlinearly (as already noticed by Minchev & Quillen, 2006); that the level of the final radial migration is strongly dependent on strengths (amplitudes) of the individual perturbations; and that the migration is stronger when the resonant radii of individual perturbations lie very close to each other.

Signatures of the resonance overlap radial migration mechanism were confirmed using self-consistent Tree-SPH N-body simulations of Minchev et al. (2011). They analyzed and compared simulations of isolated disk galaxies developing bar and spiral structure(s) of various strengths. The simulations that developed a long-lived central bar all show bimodality in the distribution of the angular momentum change – signature of the resonance overlap radial migration. This mechanism is identified as independent to the migration due to transient spirals (Sect. 3.2.1). The resonance overlap mechanism is found to be efficient on shorter time scales comparing to the mechanism due to transient spirals (Minchev & Famaey, 2010, compare their disk mixing time scale of 3 Gyr to 9 Gyr for that of the transient spirals radial migration).

3.2.3 Radial migration due to satellites

Real galaxies are not isolated systems. Quillen et al. (2009) investigated the radial migration induced tidally by orbiting satellite galaxy. They simulated a stellar galactic disk (with characteristics consistent with the MW one) by test-particles and perturbed it with a low mass satellite (few times $10^9\,M_\odot$) on a tight eccentric orbit. The satellite induces a warp and spiral structure in the outer disk of the bigger galaxy and also streams in its velocity distribution. Further, through the investigation of correlations between angular momentum change and orbital eccentricity, they found that some particles can be migrated from the outer disk to inner radii, while having orbit of low eccentricity (close-to-circular orbit).

The analysis of Quillen et al. (2009) was extended by Bird et al. (2012), who carried out self-consistent simulations of both isolated and tidally perturbed MW-like disk galaxies. By comparing the radial migration in these simulations, they identified the migrating mechanism induced by the satellite bombardment as an independent process, different to that induced by transient spirals or multiple rotating patterns. They found the orbital dynamics of migrated particles to be different than for the other mechanisms. The radial migration due to satellites also shows a different distribution of probability for particles to migrate. Bird et al. (2012) conclude that: *In the isolated disc models, the probability of migration traces the disc's radial mass profile, but in perturbed discs migration occurs preferentially at large radii, where the disc is more weakly bound.*

3.2.4 Radial migration and OCs

As mentioned in Sect. 2.3, Wu et al. (2009) analyzed the kinematics and orbits of 488 OCs, a sample mainly taken from the compilation by Dias et al. (2002a, the version available at given time). They found the radial metallicity gradient for OCs currently located at $R < 13.5$ kpc to be similar to the one derived from the apogalacticon distances of their orbits (only clusters with current radii $R < 13.5$ kpc were considered). From this result, Andreuzzi et al. (2011) implied that orbits of OCs are not affected by the radial migration and therefore they claim that: *apart from a few exceptions, it appears safe to use OCs and their present-day positions to define the metallicity distribution now and in the past.* However, as noted by Jacobson et al. (2011b), this implication is not obvious, since the processes of radial migration can move the orbital radius by several kiloparsecs while the orbit remains circular (or close-to-circular). Therefore, a cluster currently moving on close-to-circular orbit could have been born on close-to-circular orbit with different Galactocentric radii. Since Wu et al. (2009) used time independent axisymmetric gravitational potentials, the influence of the radial migration cannot be estimated from their results.

Jacobson et al. (2011b) pointed out that in the presence of radial migration one would expect the metallicity gradient to be *washed out* with time, and the older clusters to have a flat radial metallicity distribution. However, since this is not observed in the current results, they suggest that OCs should not have been affected by radial migration in the same way as the field stars are. On the other hand, Lépine et al. (2003, 2011, see also Sects. 2.5.1 and 3.2.1) assumed a long-lived spiral pattern (inducing radial migration at the corotation radii) and suggested its effect on the OCs forming a step-like radial distribution of metallicity with the transition close to the corotation radius of the spiral pattern (8.5 kpc).

Recently, Fujii & Baba (2012) investigated the radial migration of OCs directly through N-body simulations of clusters in live disks with multiple transient spiral arms. They concluded that clusters can be migrated by few kpc in few hundred Myr – *open clusters in the Galactic disk older than ∼100 Myr are expected to have already migrated from their initial galocentric radii.*

3.2.5 Signatures of radial migration observed in external disk galaxies

Apart from the MW, signatures of radial migration have been recently observed also in external disk galaxies. Yoachim et al. (2012) presented an integral field unit spectroscopy of 12 nearby disk galaxies. They constructed age and metallicity radial profiles of the outer disks of six galaxies and compared their shape with the location of the (downward) break in the radial surface brightness profiles. Three of these galaxies show an increase of stellar age beyond the break radius of the radial surface brightness profile, while the interior is dominated by active star formation. Such increase of stellar age beyond the break radius is predicted by the simulations of Roškar et al. (2008a, see Sect. 3.2.1) and it could indicate that the outer disk was formed by the radial migration due to transient spirals (similar conclusion was obtained by Radburn-Smith et al., 2012 for galaxy NGC 7793). However,

Yoachim et al. (2012) also found that in several galaxies from their sample, the outer disk is dominated by young stars and the star formation is active inside as well as outside the break radius. Consistent results were found by Roediger et al. (2012), who analyzed 64 disk galaxies in the Virgo cluster. They found that the inversion in the stellar age radial profile is present only in some of their galaxies.

Chapter 4

Galactic model and orbit integrator

To compute any Galactic orbit, it is necessary to adopt a model for the MW gravitational potential. While the general picture of the present-day MW structure is more or less well established and supported by observations, a more detailed description is still under lively discussion, see, e.g., Schönrich et al. (2010) or Coşkunoğlu et al. (2011) for the recent analysis of the velocity of the local standard of rest (LSR),[1] Reid et al. (2009), Carlin et al. (2012), or Bovy et al. (2012) for the up-to-date description of the MW rotation curve. These unresolved issues naturally bring uncertainties for the construction of any MW gravitational potential model.

We implemented a relatively simple empirical models of the gravitational potential. Details are presented in this chapter. The axisymmetric time independent part of the potential was modeled by a bulge, disk, and halo (Sect 4.1). Additionally, we included a non-axisymmetric components – bar (Sect. 4.2) and spiral arms (Sect. 4.3) – that can act separately or together. For each component, an analytic expression for the mass density or the gravitational potential is provided, from which the corresponding force can be derived.

The main idea of our study is to qualitatively estimate the viability of the migration induced by the bar and spiral arms resonance overlap mechanism relative to the migration in simpler potentials, either purely axisymmetric or containing just one type of non-axisymmetric perturbation. Through our choice of model and its parameters, we do not aim to reproduce the MW mass distribution and properties precisely. Precise values of some of the MW parameters are not known anyway and they obey significant uncertainties. Therefore, our models attempt to qualitatively reproduce the main features consistent with the recent picture of the MW.

[1] The LSR is an inertial reference frame centered on the Sun and moving on a circular orbit in the Galactic potential in the direction of the Galactic rotation (Binney & Tremaine, 2008).

4.1 Axisymmetric model

Two different models for the 3-component axisymmetric time independent part of the potential were considered. The main model is based on the one presented by Flynn et al. (1996). Additionally, we also implemented a model based on Allen & Santillan (1991), which, in some aspects follows the recent knowledge of the MW mass distribution less precisely. However, we tested this model for the sake of comparison, since it has been often used by the community (see Sect. 4.1.2 for details). The results presented in Sects. 5 and 6 are calculated using the axisymmetric model based on Flynn et al. (1996), however, their general nature stays very similar when the model by Allen & Santillan (1991) is used.

4.1.1 Model based on Flynn et al. (1996)

The first model we implemented for the axisymmetric time independent potential is the model introduced by Flynn et al. (1996) and which was also used by, for example, Gardner & Flynn (2010). The model is composed of bulge, disk and halo. The bulge is modeled as a superposition of two Plummer (1911) spheres; the disk is modeled as a superposition of three Miyamoto & Nagai (1975) disks; and the dark halo is modeled as a spherical logarithmic potential. The equations for each component of the axisymmetric potential are:

$$\phi_0 = \sum_{i=1}^{2} \phi_{\mathrm{C}_i} + \sum_{i=1}^{3} \phi_{\mathrm{D}_i} + \phi_{\mathrm{H}}, \tag{4.1}$$

$$\phi_{\mathrm{C}_n} = -\frac{GM_{\mathrm{C}_n}}{\sqrt{r^2 + r_{\mathrm{C}_n}^2}}, \quad n = 1, 2, \tag{4.2}$$

$$\phi_{\mathrm{D}_n} = -\frac{GM_{\mathrm{D}_n}}{\sqrt{\left\{R^2 + \left[a_n + \sqrt{(z^2 + b^2)}\right]^2\right\}}}, \quad n = 1, 2, 3, \tag{4.3}$$

$$\phi_{\mathrm{H}} = \frac{1}{2} V_{\mathrm{H}}^2 \ln\left(r^2 + r_0^2\right), \tag{4.4}$$

where r is the radius in spherical the coordinates, R is the Galactocentric radius defined in the cylindrical coordinates, and z the vertical distance from the Galactic plane ($r^2 = R^2 + z^2$). G is the gravitational constant. M_{C_n} and r_{C_n} are the bulge components masses and scale radii of, respectively (n goes from 1 to 2; the letter C in the subscript stays for central). M_{D_n} and a_n are the disk components masses and scale lengths, respectively (n goes from 1 to 3; the letter D in the subscript denotes disk). The parameter b is related to the scale height of the disk and is the same for all three components of the disk. r_0 is the halo core radius and V_{H} its asymptotic circular velocity (at large radii relative to r_0).

Flynn et al. (1996) chose the parameters of their model to reproduce the MW observations as known at that time. We modified values of some parameters to achieve a model consistent with a more up-to-date MW observations. As for the recent observations of the rotation curve at the solar Galactocentric radius $R_\odot$, Reid et al. (2009) estimated

Table 4.1: Parameters of the axisymmetric model based on Flynn et al. (1996).

Component	Parameter	Value
Bulge	M_{C_1}	$0.3{\cdot}10^{10}\mathrm{M}_\odot$
	r_{C_1}	2.7 kpc
	M_{C_2}	$1.6{\cdot}10^{10}\mathrm{M}_\odot$
	r_{C_2}	0.42 kpc
Disk	M_{D_1}	$8.9{\cdot}10^{10}\mathrm{M}_\odot$
	a_1	5.0 kpc
	$M_{\mathrm{D}_2}{}^a$	$-6.9{\cdot}10^{10}\mathrm{M}_\odot$
	a_2	15.8 kpc
	M_{D_3}	$2.8{\cdot}10^{10}\mathrm{M}_\odot$
	a_3	33.0 kpc
	b	0.3 kpc
Halo	V_{H}	225 $\mathrm{km\,s^{-1}}$
	r_0	8.4 kpc

Notes. $^{(a)}$ Note that the mass M_{D_2} is negative. The resulting total density is nevertheless positive everywhere.

$R_\odot = (8.4{\pm}0.6)\,\mathrm{kpc}$ and the circular velocity at solar radius as $v_\mathrm{c}(R_\odot) = (254{\pm}16)\,\mathrm{km\,s^{-1}}$. To derive these values, they used the solar motion with respect to the LSR, $\mathbf{v}_{\odot,\mathrm{LSR}}$, as determined by Dehnen & Binney (1998) from a set of Hipparcos stars. The same Hipparcos data set was later re-examined by Schönrich et al. (2010), who obtained slightly different values for the $\mathbf{v}_{\odot,\mathrm{LSR}}$ components. The analysis of Schönrich et al. (2010) takes into account the correlation between the color of the stellar population and the radial gradients of its mean rotation velocity and velocity dispersion. This correlation was not considered by Dehnen & Binney (1998). Schönrich et al. (2010) updated the vector of the solar motion and found the velocity component in direction of the Galactic rotation to be of about $7\,\mathrm{km\,s^{-1}}$ higher than that of Dehnen & Binney (1998).

Considering these more recent results, we changed the original Flynn et al. (1996) values for the halo circular velocity V_H and the disk parameters (masses and scale radii) to obtain the circular velocity of $v_\mathrm{c}(R_\odot) = 243\,\mathrm{km\,s^{-1}}$ at the solar Galactocentric radii $R_\odot = 8.4\,\mathrm{kpc}$. These values are also consistent with the circular velocity at solar radius derived from the apparent proper motion of Sgr A* (Reid & Brunthaler, 2004) using $R_\odot = 8.4\,\mathrm{kpc}$ and the Schönrich et al. (2010) solar motion.

The superposition of three Miyamoto & Nagai disks builds up a disk with an exponential falloff of the radial surface density on a wide range of radii. Similarly as Gardner & Flynn (2010), we chose the disk parameters to obtain the scale length of the exponential falloff of the disk consistent with the recent observations. Our disk gives a radial surface density profile approximately corresponding to the exponential falloff with the scale length of 2.6 kpc for radii of 5–18 kpc. This falloff is consistent with the recent mapping of the MW stellar density distribution from the SDSS by Jurić et al. (2008). See

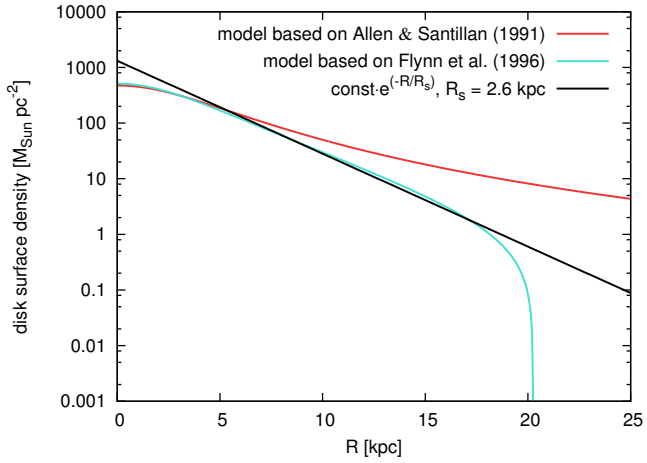

Figure 4.1: Radial profile of the disk surface density for the two axisymmetric models described in the text. Red and blue line show the model based on the Allen & Santillan (1991) and Flynn et al. (1996), respectively. Black line shows the surface density with the exponential falloff with the scale length of 2.6 kpc, which is consistent with the recent analysis of the MW stellar density distribution by Jurić et al. (2008). Note that the vertical axis is logarithmic.

Fig. 4.1 for the comparison of the radial surface density profiles of our implementations of the Flynn et al. (1996) and Allen & Santillan (1991, discussed in Sect. 4.1.2), and the exponential falloff.

Values for all parameters of the axisymmetrical components are given in Table 4.1. The described axisymmetric potential was also used in the models including the non-axisymmetric components. However, when we include the bar perturbation, the central component mass M_{C_2} was reduced and the bar replaces most of the bulge mass. We kept the axisymmetric components unaltered when we turn the spiral arms perturbation on (see Sect. 4.3).

4.1.2 Model based on Allen & Santillan (1991)

In the Allen & Santillan (1991) model, the bulge has form of a single Plummer (1911) sphere, see Eq. (4.2); the disk is a single Miyamoto & Nagai (1975), see Eq. (4.3); and the halo has a special spherically symmetric form:

$$\phi_{\mathrm{H}} = -\frac{M(r)}{r} - \frac{M_{\mathrm{H}}}{1.02 a_{\mathrm{H}}} \left[-\frac{1.02}{1+(r/a_{\mathrm{H}})^{1.02}} + \log\left\{1+(r/a_{\mathrm{H}})^{1.02}\right\} \right]_{r}^{100\,\mathrm{kpc}}, \tag{4.5}$$

$$\text{and} \quad M(r) = \frac{M_{\mathrm{H}}\,(r/a_{\mathrm{H}})^{2.02}}{1+(r/a_{\mathrm{H}})^{1.02}}, \tag{4.6}$$

where M_{H} is the halo mass parameter and a_{H} the halo scale length. Eq. (4.6) includes an arbitrary cut-off for the halo at 100 kpc.

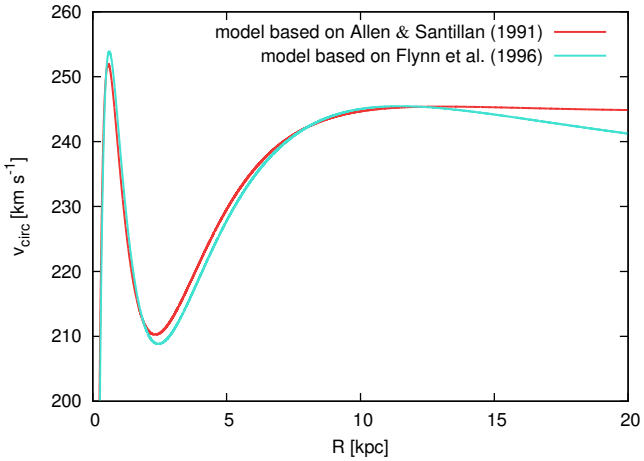

Figure 4.2: Rotation velocity curve for the two axisymmetric models described in the text. Red and blue line show the model based on the Allen & Santillan (1991) and Flynn et al. (1996), respectively.

Table 4.2: Parameters of the axisymmetric model based on Allen & Santillan (1991).

Component	Parameter	Value
Bulge	M_{C}	$1.4{\cdot}10^{10}\mathrm{M}_{\odot}$
	r_{C}	0.39 kpc
Disk	M_{D}	$8.6{\cdot}10^{10}\mathrm{M}_{\odot}$
	r_{D}	5.32 kpc
	b	0.25 kpc
Halo	M_{H}	$1.8{\cdot}10^{11}\mathrm{M}_{\odot}$
	a_{H}	12.0 kpc

Allen & Santillan (1991) assumed the solar Galactocentric radius $R_{\odot}$ of 8.5 kpc and the circular velocity at the solar radius $v_{\mathrm{c}}(R_{\odot})$ of 220 km s^{-1}. However, as already discussed in Sect. 4.1.1, more recent studies suggest different values for these quantities. Considering these, we scaled the halo mass parameter M_{H} up to obtain $v_{\mathrm{c}}(R_{\odot}) = 243\,\mathrm{km\,s^{-1}}$ at $R_{\odot} = 8.4\,\mathrm{kpc}$ (see Fig. 4.2). The halo mass parameter M_{H} in Eq. (4.6) was increased from $1.07{\cdot}10^{11}\mathrm{M}_{\odot}$ to $1.8{\cdot}10^{11}\mathrm{M}_{\odot}$. Except for M_{H}, the set of parameters characterizing the axisymmetric model is the same as derived by Allen & Santillan (1991). All the parameters are given in Table 4.2.

Figure 4.2 shows that the rotation curves for both axisymmetric models are very similar. On the other hand, Fig. 4.1 shows that the disk of the Allen & Santillan (1991) model does not resemble the exponential falloff as is expected for the Galactic disk. However, the model based on Allen & Santillan (1991) has been recently and extensively used by several teams dealing with orbits of the MW clusters (Allen et al., 2006, 2008; Wu et al., 2009; Pichardo et al., 2012; Bellini et al., 2010a), with the solar neighborhood

kinematics (Antoja et al., 2009, 2011), or the inner Galactic disk Bensby et al. (2010). For this reason, we tested our integrations using the Allen & Santillan (1991) model. As noted, the nature of the general results presented in Sects. 5 and 6 stay the same like for the model based on Flynn et al. (1996). Further, we describe only the results of the Flynn et al. (1996) model.

4.2 Galactic bar

For the bar model we adopted the Ferrers potential (see paragraph 2.5.3 (a) of Binney & Tremaine, 2008, where we choose $n = 2$) of an inhomogeneous triaxial ellipsoid. A general Ferrers potential arises from the mass density of a form (see, e.g., Pfenniger, 1984):

$$\rho_{\mathrm{B}}(m^2) = \begin{cases} \rho_{\mathrm{c}}(1-m^2)^2 & \text{for } m \leq 1, \\ 0 & \text{for } m > 1, \end{cases} \tag{4.7}$$

$$\text{where} \qquad m^2 = x^2/a^2 + y^2/b^2 + z^2/c^2, \quad a > b \geq c. \tag{4.8}$$

x, y, z are Cartesian coordinates, and a, b, c are the semi-axes of the ellipsoid. ρ_{c} is the central density related to the total mass of the bar M_{B}, by

$$\rho_{\mathrm{c}} = \frac{105}{32\pi}\frac{M_{\mathrm{B}}}{abc}. \tag{4.9}$$

The mass density of the form given by Eq. (4.7) has a smooth decrease to zero value at a finite distance (outside the ellipsoid given by semi-axis a, b, c, where $m > 1$). The numerical procedures, which we used for the calculation of the potential and forces are given by Pfenniger (1984) and de Zeeuw & Pfenniger (1988).

Except for its shape and size (given by the semi-axes a, b, c), and its mass M_{B}, the bar is defined by its angular velocity Ω_{B} and its orientation in the Galactic plane. The latter is characterized by the angle φ_{B}, given with respect to the direction from the Galactic center to the Sun. For all bar parameters, listed in Table 4.3, we adopted the same values as reported by Pichardo et al. (2004) and refer the reader to their original paper for a justification of the various choices.

4.3 Spiral arms

Parameters of the Galactic spiral structure are much more uncertain than for the Galactic bar. Most observational studies suggest two- or four-armed spiral pattern, or their superposition (see, for example, Vallée 2005; Vallée 2008; Allen et al. 2008; Grosbol et al. 2011).

We model the spiral arms as described by Cox & Gómez (2002) – the mass density of the spiral arms is considered as a perturbation of the axisymmetric disk (part of the stellar mass of the disk is redistributed into the mass of the spiral arms). We use a two-armed spiral pattern rotating with a constant angular velocity and the perturbation has

Table 4.3: Parameters of non-axisymmetric components in the present-day MW model.

Parameter	Value	Reference
Galactic bar		
Bar mass $M_{\rm B}$	$0.98{\cdot}10^{10}{\rm M}_\odot$	(2)
Bulge mass $M_{\rm C_2}$	$0.62{\cdot}10^{9}{\rm M}_\odot$	(2)
Angular velocity $\Omega_{\rm B}$	$60.0\,{\rm km\,s^{-1}\,kpc^{-1}}$	(2)
Major semi-axis a	$3.14\,{\rm kpc}$	(2)
Minor semi-axis b	$1.178\,{\rm kpc}$	(2)
Minor semi-axis c	$0.81\,{\rm kpc}$	(2)
Bar angle $\varphi_{\rm B}$	20°	(2)
Spiral arms		
Number of spiral arms	2	(3)
Pitch angle α	15.5°	(3)
Density amplitude ρ_0	$3.36\cdot10^{7}{\rm M}_\odot\,{\rm kpc^{-3}}$	
Angular velocity $\Omega_{\rm SA}$	$20.0\,{\rm km\,s^{-1}\,kpc^{-1}}$	(1), (5)
Scale length $R_{\rm SA}$	$2.6\,{\rm kpc}$	(4)
Scale height $h_{\rm SA}$	$0.3\,{\rm kpc}$	(4)
Scale radius R_0	$5.6\,{\rm kpc}$	(3)

References. (1) Pichardo et al. (2003); (2) Pichardo et al. (2004); (3) Drimmel (2000); (4) Jurić et al. (2008); (5) Gerhard (2011).

the shape of a logarithmic spiral. Cox & Gómez (2002) found an approximative solution for the perturbation of the gravitational potential of density given by

$$\rho_{\rm SA}(R,z,\varphi,t) = \rho_{\rm A}(R,z)\cos\left\{2\left[\varphi+\Omega_{\rm SA}t-\frac{\ln(R/R_0)}{\tan(\alpha)}\right],\right\} \tag{4.10}$$

$$\text{where}\quad \rho_{\rm A}(R,z) = \rho_0\exp\left(-\frac{R-R_0}{R_{\rm SA}}\right)\operatorname{sech}^2\left(\frac{z}{h_{\rm SA}}\right), \tag{4.11}$$

where R, φ, z are the cylindrical coordinates, t is the time, ρ_0 is the amplitude of the density perturbation (arms mass density in the Galactic plane at the point $(R,\varphi) = (R_0,0)$, at the time $t=0$), $R_{\rm SA}$ is the radial scale length, $h_{\rm SA}$ the scale height, and α the pitch angle. $R_{\rm SA}$, $h_{\rm SA}$, and α define the shape of the density spiral arms pattern, while radius R_0 specifies the initial orientation of the pattern. $\Omega_{\rm SA}$ is the angular velocity of the spiral arms rotation.

Following Cox & Gómez (2002), the approximate solution for the gravitational potential given by the density perturbation (4.10) is

$$\phi_{\mathrm{SA}}(R,z,\varphi) = -4\pi G h_{\mathrm{SA}} \rho_0 \exp\left(-\frac{R-R_0}{R_{\mathrm{SA}}}\right) \frac{1}{KD} \cos(\gamma) \left[\operatorname{sech}\left(\frac{Kz}{\beta}\right)\right]^{\beta}, \tag{4.12}$$

$$\text{where} \quad \gamma = 2\left[\varphi + \Omega_{\mathrm{SA}} t - \frac{\ln(R/R_0)}{\tan(\alpha)}\right]. \tag{4.13}$$

K, β, and D are functional parameters dependent on the Galactocentric radius:

$$K = \frac{2}{R\sin(\alpha)}, \tag{4.14}$$

$$\beta = K h_{\mathrm{SA}}(1 + 0.4 K h_{\mathrm{SA}}), \tag{4.15}$$

$$D = \frac{1 + K h_{\mathrm{SA}} + 0.3(K h_{\mathrm{SA}})^2}{1 + 0.3 K h_{\mathrm{SA}}}. \tag{4.16}$$

The corresponding force vector can be found as the negative gradient of the gravitational potential (4.12) and is given in Appendix A. The mass density exactly corresponding to the potential given by Eq. (4.12) can be found using the Poisson equation, either numerically or analytically as described by Cox & Gómez (2002).

To get a model consistent with the current picture of the MW spiral structure, we based our choice of parameters – listed in Table 4.3 – mostly on studies of Drimmel (2000) and Drimmel & Spergel (2001). Using the K band emission profiles recovered from the COBE/DIBRE data, Drimmel (2000) identified features associated with arm tangents at Galactic longitudes of 30° and −53°. These features are consistent with a two-armed logarithmic spiral structure with a pitch angle of 15.5°. The two-armed picture was later favored also by the results of the Spitzer Space Telescope GLIMPSE (Galactic Legacy Infrared Mid-Plane Survey Extraordinaire) surveys at wavelengths of 3.6–24 μm, see, e.g., the summary by Churchwell et al. (2009). Drimmel & Spergel (2001) presented a 3-dimensional model for the MW fitted to the COBE far-infrared and near-infrared emission. They found that a two-armed structure dominates the near-infrared emission. The arm–interarm density contrast of their modeled stellar spiral arms has a value of about 1.8 at the solar radius (see Fig. 15 in Drimmel & Spergel, 2001). Our choice of parameters (the density amplitude ρ_0 and the scale length R_{SA}, for the pitch angle of 15.5°) for the Cox & Gómez (2002) model gives 2.0 for the same ratio. This value is further consistent with the observations of external galaxies with a weaker spiral structure (see, e.g., Block et al., 2004). Finally, we chose the scale height h_{SA} similar to the thin disk scale height of the axisymmetric model (0.3 kpc from Jurić et al., 2008).

As for the angular velocity of the spiral arms, a recent review of the methods and results published within 1999 and 2007 was given by Gerhard (2011), the angular velocity having values from 17 to 30 $\mathrm{km\,s^{-1}\,kpc^{-1}}$. We decided to use the value of 20 $\mathrm{km\,s^{-1}\,kpc^{-1}}$, which is also favored by models (e.g., Pichardo et al., 2003).

To determine the initial orientation of the spiral arms pattern, given by the radius R_0, we once again followed the results of the study of the COBE/DIRBE K band emission presented by Drimmel (2000). The spiral arms density is defined by Eg. (4.10) and

the initial orientation of the arms corresponds to the term $\ln(R_0)/\tan(\alpha)$. The features associated with arm tangents are located at the Galactic longitudes of 30° and −53°. From a geometrical consideration, using the logarithmic spiral with the pitch angle of 15.5°, we obtain R_0 of 5.6 kpc (which corresponds to the spiral angle offset of 4.1°, measured with respect to the direction from the Galactic center to the Sun in the anti-direction of the Galactic rotation).

4.4 Strength of rotating patterns

An illustrative way of estimating the strength of the non-axisymmetric components in models was proposed by Combes & Sanders (1981). To measure the torques of bars, they defined a quantity of bar strength at radius R,

$$Q_{\mathrm{T}}(R) = \frac{F_{\varphi}^{\max}(R)}{F_R^0(R)}, \tag{4.17}$$

where

$$F_{\varphi}^{\max}(R) = \left| \frac{\partial\phi(R,\varphi,0)}{R\,\partial\varphi} \right|_{\max}, \tag{4.18}$$

is the maximum tangential force at radius R. $\phi(R,\varphi,z)$ is the gravitational potential. Further,

$$F_R^0(R) = \left\langle \frac{\partial\phi(R,\varphi,0)}{\partial R} \right\rangle_{\varphi}, \tag{4.19}$$

is the mean radial force at radius R (the subscript φ signalizes that the mean value is calculated over the full azimuth). Both forces, $F_{\varphi}^{\max}(R)$ and $F_{\varphi}^{\max}(R)$, are measured in the galactic plane ($z = 0$). In other words, $Q_{\mathrm{T}}(R)$ measures the maximal tangential force due to the non-monopole part of the potential in units of the radial force due to the monopole part at the same radius R. $Q_{\mathrm{T}}(R)$ depends on radius but often its maximal value is used as a single measure of the bar strength in the galaxy and is referred to as the *bar strength parameter*.

Equation (4.17) can be generalized to map the torques strength in the 2-dimensional plane as, e.g., in Buta & Block (2001). The tangential force in units of the monopole radial force is mapped in the whole galactic plane

$$Q_{\mathrm{T}}(R,\varphi) = \frac{F_{\varphi}(R,\varphi,0)}{F_R^0(R)}. \tag{4.20}$$

In a similar way, the radial force due to the non-monopole part of the potential can be mapped as

$$Q_{\mathrm{R}}(R,\varphi) = \frac{F_R(R,\varphi,0) - F_R^0(R)}{F_R^0(R)}. \tag{4.21}$$

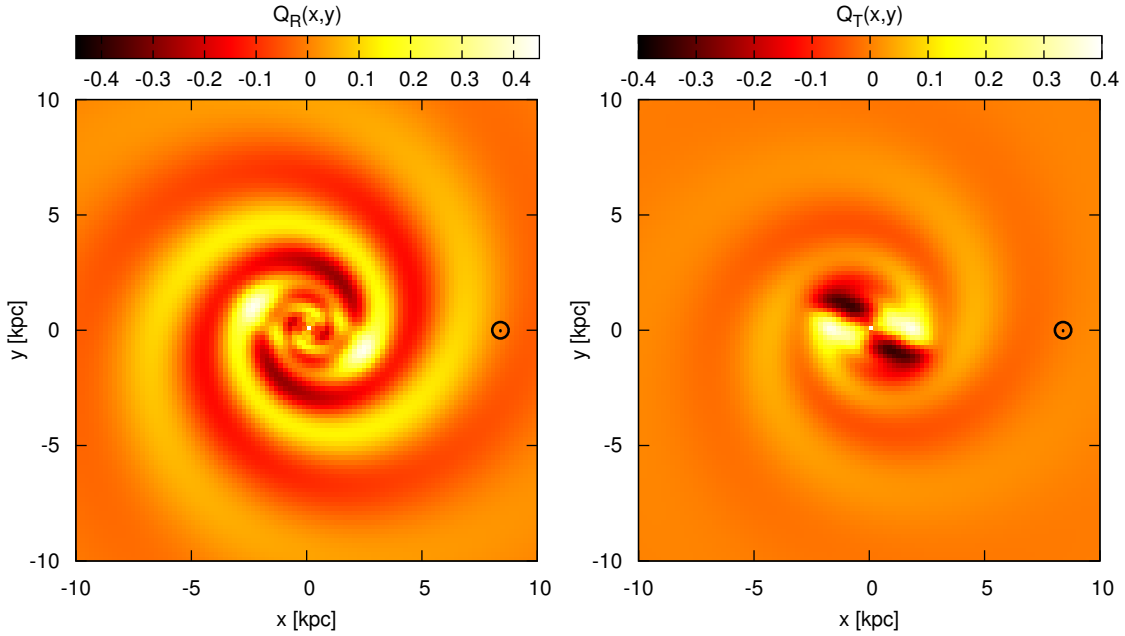

Figure 4.3: Maps of strength of the non-axisymmetric components in the combined (including the bar and spiral arms) present-day MW model (noted as MW1 in Sect. 5.2). Color scales map the ratio between the radial (*left*) and the tangential (*right*) force resulting from the non-monopole part of the gravitational potential to the radial force due to the monopole part at the same radius. Maps are plotted for the Galactic plane. Symbol $\odot$ marks the position of the Sun.

Figure 4.3 shows maps of $Q_{\mathrm{T}}(R, \varphi)$ and $Q_{\mathrm{R}}(R, \varphi)$ for our combined MW model (including both, the bar and the spiral arms) potential. Our choice of bar model gives the bar strength parameter of 0.4. The model of spiral arms gives the value of 0.05 for an analogical parameter (using the tangential force from the spiral arms instead of the bar in the definition of the bar strength parameter).

4.5 Orbit calculation

To see and understand the differences caused by the bar and spiral arms, we calculated the orbits in four versions of the MW model – the axisymmetric potential, the potential including the bar, the potential including the spiral arms, and finally, a combined model including both, bar and spiral arms.

4.5.1 Equations of motion

We have considered the cluster as a point-mass living in the gravitational field of the Galaxy. Once a model of gravitational potential is adopted, the corresponding equations

of motion can be constructed. The gravitational potential ϕ is modeled as a sum of potentials of individual components. Eq. (4.1) describes the potential in the axisymmetric case. When a non-axisymmetric perturbation is present, its potential is added to the axisymmetric background and the non-axisymmetric perturbation rotates steadily with a constant angular velocity around the z axis. In the case when the bar is included, the mass of the bulge component is reduced (see Sect. 4.1). When a single non-axisymmetric perturbation is present, then the gravitational potential is static in the reference frame steadily co-rotating with the perturbation (the bar or the spiral arms). Below, we derive the equations of motion (following Binney & Tremaine, 2008) which we integrate numerically to obtain the Galactic orbit.

Let the Cartesian coordinates in the rotating reference frame be noted $\boldsymbol{r}_\mathrm{r} = (x_\mathrm{r}, y_\mathrm{r}, z_\mathrm{r})$, the velocity in the rotating reference frame is $\boldsymbol{v}_\mathrm{r} = (v_{x,\mathrm{r}}, v_{y,\mathrm{r}}, v_{z,\mathrm{r}})$, and $\boldsymbol{\Omega} = (0, 0, \Omega)$ is the constant angular velocity of the non-axisymmetric perturbation. Then the velocity in the inertial non-rotating reference frame is $\boldsymbol{v} = \boldsymbol{v}_\mathrm{r} + \boldsymbol{\Omega} \times \boldsymbol{v}_\mathrm{r}$ and the Lagrangian,

$$L = \frac{1}{2} \left| \boldsymbol{v}_\mathrm{r} + \boldsymbol{\Omega} \times \boldsymbol{v}_\mathrm{r} \right|^2 - \phi(\boldsymbol{r}_\mathrm{r}). \tag{4.22}$$

The canonical momentum,

$$\boldsymbol{p} = \frac{\partial L}{\partial \boldsymbol{v}_\mathrm{r}} = \boldsymbol{v}_\mathrm{r} + \boldsymbol{\Omega} \times \boldsymbol{v}_\mathrm{r}, \tag{4.23}$$

coincides with the velocity in the inertial frame $\boldsymbol{v}$. The Hamiltonian of the system is

$$H(\boldsymbol{p}, \boldsymbol{r}_\mathrm{r}) = \frac{1}{2}\boldsymbol{p}^2 - \boldsymbol{\Omega} \cdot (\boldsymbol{r}_\mathrm{r} \times \boldsymbol{p}) + \phi(\boldsymbol{r}_\mathrm{r}). \tag{4.24}$$

Since the Hamiltonian does not explicitly depend on time, it is an integral of motion, so-called *Jacobi constant* (or also the Jacobi energy or Jacobi integral, see, for example, Binney & Tremaine, 2008 for more details).

Finally, the equations of motion are

$$\frac{\mathrm{d}\boldsymbol{r}_\mathrm{r}}{\mathrm{d}t} = \boldsymbol{p} - \boldsymbol{\Omega} \times \boldsymbol{r}_\mathrm{r}, \qquad \frac{\mathrm{d}\boldsymbol{p}}{\mathrm{d}t} = -\boldsymbol{\Omega} \times \boldsymbol{p} - \nabla\phi, \tag{4.25}$$

or when writing for each components individually,

$$\begin{aligned}
\frac{\mathrm{d}x_\mathrm{r}}{\mathrm{d}t} &= v_x + \Omega y_\mathrm{r}, & \frac{\mathrm{d}v_x}{\mathrm{d}t} &= -\frac{\mathrm{d}\phi}{\mathrm{d}x_\mathrm{r}} + \Omega v_y, \\
\frac{\mathrm{d}y_\mathrm{r}}{\mathrm{d}t} &= v_y - \Omega x_\mathrm{r}, & \frac{\mathrm{d}v_y}{\mathrm{d}t} &= -\frac{\mathrm{d}\phi}{\mathrm{d}y_\mathrm{r}} - \Omega v_x, \\
\frac{\mathrm{d}z_\mathrm{r}}{\mathrm{d}t} &= v_z, & \frac{\mathrm{d}v_z}{\mathrm{d}t} &= -\frac{\mathrm{d}\phi}{\mathrm{d}z_\mathrm{r}},
\end{aligned} \tag{4.26}$$

where we used that the momentum $\boldsymbol{p}$ coincides with the velocity in the inertial frame $\boldsymbol{v}$.

To calculate the orbits, we used the set of first-order differential equations (4.26), which we integrated using a Bulirsch-Stoer integrator with adaptive time steps (Press

et al., 1992, specifically their `subroutine bsstep`). In the axisymmetric case, obviously, the pattern angular velocity $\boldsymbol{\Omega} = \mathbf{0}$, and the equations reduce to the non-rotating case and the Jacobi constant reduces to the energy. When a single rotating pattern is present in the model, $\boldsymbol{\Omega}$ equals the angular velocity of the given pattern – in the presence of the bar, $\boldsymbol{\Omega} = (0, 0, \Omega_{\rm B})$; and in the presence of the spiral arms; $\boldsymbol{\Omega} = (0, 0, \Omega_{\rm SA})$. The relative change in the Jacobi constant for the models with a single rotating pattern is of the order of 10^{-10}. In the case when both rotating perturbations are present, there is no integral of motion along any orbit, and we integrate Eqs. (4.26) using $\boldsymbol{\Omega} = (0, 0, \Omega_{\rm B})$ and $\boldsymbol{r}_{\rm r}$ is the position vector in the reference frame rotating with the bar.

Chapter 5

The orbit and origin of NGC 6791

In the first part of this chapter (Sect. 5.1) we calculate and characterize the recent orbit of the open cluster NGC 6791. In the second part (Sect. 5.2) we aim at investigating in details the scenario in which NGC 6791 formed close to the Galactic center and later migrated outward (to its current position in the disk) due to the radial migration caused by the resonance overlap of the bar and spiral arms. Finally, in the third part (Sect. 5.3) we present a simple estimate of the cluster initial mass.

5.1 Recent orbit of NGC 6791 from backward integration

To calculate the recent orbit of NGC 6791, we first derive the initial conditions (Sect. 5.1.1). Then, we integrate its orbit using axisymmetric time independent model of the present-day MW as well as models including the bar or spiral arms. We derive orbital parameters and their uncertainties given by the errors of the input observational data (Sect. 5.1.2). Finally, we compare our results with these published in the literature (Sect. 5.1.3).

5.1.1 Initial conditions

To investigate the shape and properties of the recent orbit of NGC 6791, we integrate its orbit backward for 1 Gyr, starting from the cluster current position and velocity vectors. These initial vectors were obtained from up-to-date observational data found in the literature: equatorial celestial coordinates (α and δ for J2000.0 equinox), distance to the Sun $d_\odot$, radial velocity v_r, and cluster mean PM vector with components $\mu_\alpha \cos\delta$ and μ_δ. As described in Sect. 2.6, NGC 6791 has been subject of an intense study in the past. Up-to-date values for aforementioned parameters are listed in Table 5.1 together with their sources. These input observational quantities need to be transformed into an appropriate coordinate system, so they can be used as the initial conditions for orbit integration.

For our orbit integrations, we use a Cartesian Galactocentric right-handed coordinate system: the x axis points from the Galactic center outward, in the direction of the Sun;

Table 5.1: Observational data for NGC 6791

Quantity	Adopted value	Reference
α	290.22083°	(1)
δ	37.77167°	(1)
v_r	$-47.1\pm0.7\,\mathrm{km\,s^{-1}}$	(2)
$\mu_\alpha \cos\delta$	$-0.57\pm0.13\,\mathrm{mas\,yr^{-1}}$	(2)
μ_δ	$-2.45\pm0.12\,\mathrm{mas\,yr^{-1}}$	(2)
$d_\odot$	$4.01\pm0.14\,\mathrm{kpc}$	(3)

Notes. Equatorial coordinates α, δ (J2000) of the cluster photometric center; radial velocity v_r; PM components $\mu_\alpha \cos\delta$, μ_δ; distance to the Sun $d_\odot$.

References. (1) WEBDA; (2) Bedin et al. (2006, see also references therein); (3) Brogaard et al. (2011).

Table 5.2: Initial conditions for the NGC 6791 orbit

x	σ_x	y	σ_y	z	σ_z	v_x	σ_{v_x}	v_y	σ_{v_y}	v_z	σ_{v_z}
[kpc]		[kpc]		[kpc]		[km s^{-1}]		[km s^{-1}]		[km s^{-1}]	
7.05	0.04	−3.70	0.13	0.76	0.03	−39.7	2.7	−197.7	1.3	−12.1	2.6

Notes. Given values of initial conditions are derived for the mean observational input data (Table 5.1), together with the standard deviations of their distributions.

the y axis points in the anti-direction of the LSR motion; and the z axis points toward the North Galactic Pole. The position of the Sun is given by vector $(x, y, z)_\odot = (8.4, 0, 0)\,\mathrm{kpc}$ in this coordinate system (the solar Galactocentric radius is taken from Reid et al., 2009, see Sect. 4.1.1). The transformation of the observational data to the Cartesian coordinate system centered on the Sun was performed following the Johnson & Soderblom (1987) algorithm updated to the International Celestial Reference System (with the coordinates of the North Galactic Pole: $\alpha = 192.85948^\circ$, $\delta = 27.12825^\circ$, Binney & Merrifield, 1998). Adopting the solar motion with respect to the LSR from Schönrich et al. (2010): $\mathbf{v}_{\odot,\mathrm{LSR}} = (U, V, W)_\odot = (11.1, 12.24, 7.25)\,\mathrm{km\,s^{-1}}$ (right-handed system, with U in the direction to the Galactic center and V in the Galactic rotation direction), the velocity vector with respect to LSR was obtained. Finally, using the solar Galactocentric radius $R_\odot = 8.4\,\mathrm{kpc}$ and the LSR circular velocity $v_\mathrm{c}(R_\odot) = 243\,\mathrm{km\,s^{-1}}$ (see Sect. 4.1), the position and velocity vectors were transformed into the coordinate system of the integrations (denoted as x, y, z, v_x, v_y, v_z).

The input observational data come naturally with some associated uncertainties, which translate into uncertainties in the initial condition vectors. To take the observational uncertainties into account, we followed Dinescu et al. (1999, see also Wu et al., 2009; Vande Putte et al., 2010), and calculated a set of 1000 initial conditions realizations.

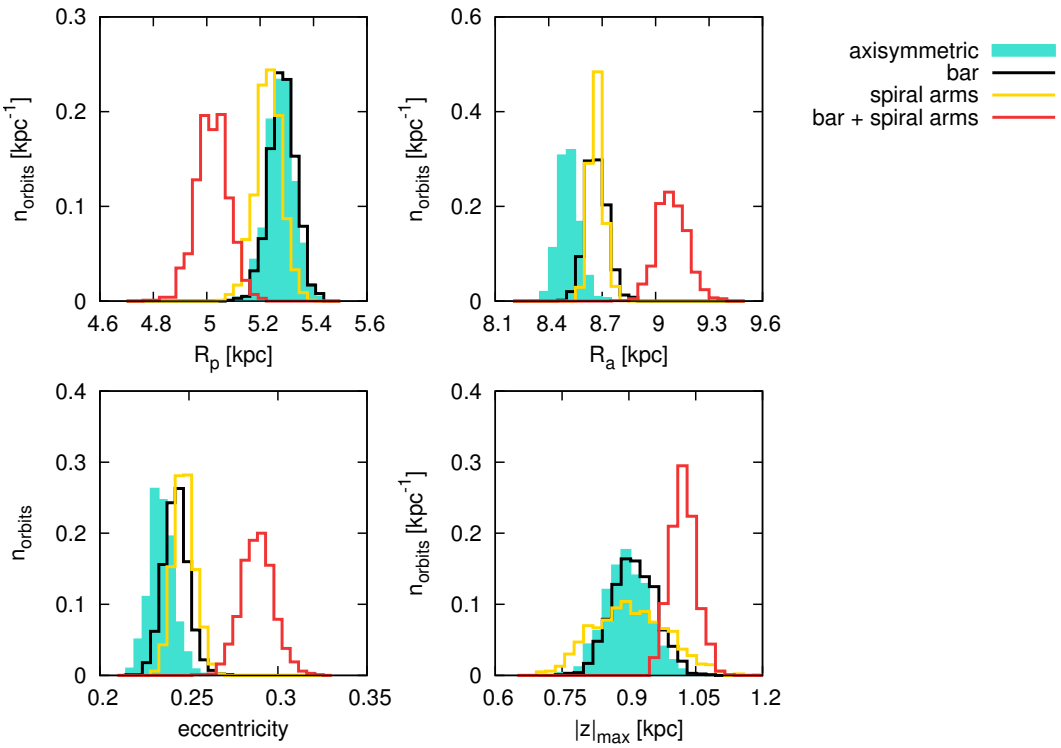

Figure 5.1: Distributions of cluster recent orbital parameters. The distributions for perigalacticon distance $R_{\rm p}$, apogalacticon distance $R_{\rm a}$, vertical height of the orbit $|z|_{\rm max}$, and eccentricity e, are plotted. Different colors show results for different MW models: axisymmetric model – light blue, model with bar – black, model with spiral arms – yellow, combined model with bar and spiral arms – red.

The initial velocity and position vectors were extracted from normally distributed values of radial velocity, PM components, and the distance to the Sun. The standard deviation of each distribution was taken as the observational uncertainty of the given input data from Table 5.1. The initial positions and velocities (x, y, z, v_x, v_y, v_z) derived from the mean observational input data are given in Table 5.2. We integrated an orbit for each initial conditions vector backward for 1 Gyr.

5.1.2 Orbits and orbital parameters

Galactic orbits are routinely described by a set of orbital parameters, which can characterize each cycle (revolution) of the orbit. One cycle of orbit is completed when the azimuthal coordinate change is 2π. Orbital parameters are: the perigalacticon distance $R_{\rm p}$ – the minimal radius R in the Galactic plane; the apogalacticon distance $R_{\rm a}$ – the maximal radius R in the Galactic plane; the vertical amplitude $|z|_{\rm max}$ – the maximal distance from the Galactic plane; and the eccentricity e – defined as $(R_{\rm a} - R_{\rm p})/(R_{\rm a} + R_{\rm p})$. De-

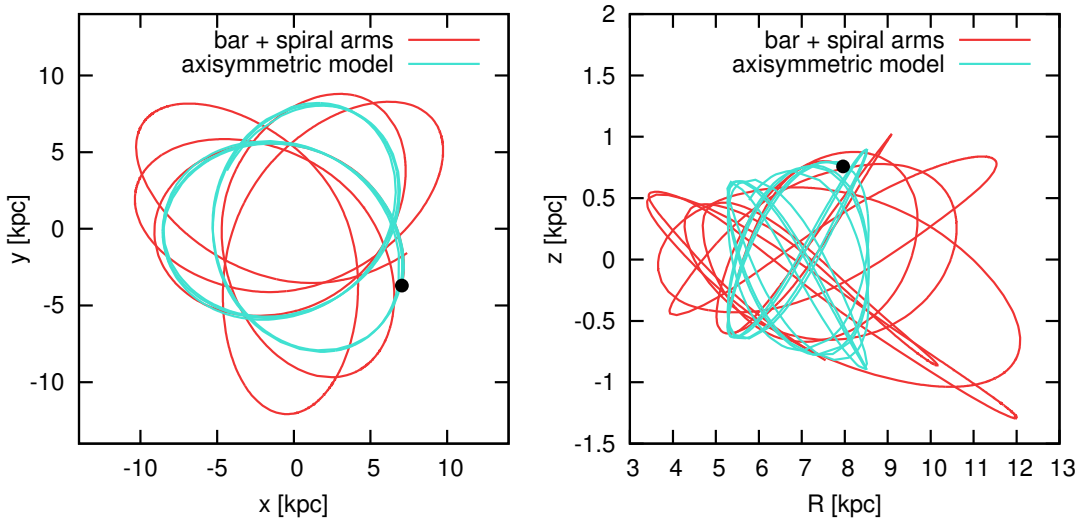

Figure 5.2: Recent portion of the orbit of NGC 6791. Orbit projection into the Galactic and the meridional (R, z) plane is plotted on the left and right, respectively. Orbit in the axisymmetric potential is plotted with the blue line. The red line shows the combined model (bar and spiral arms). The initial conditions (Table 5.2) are given by the mean input observational data (Table 5.1). The black dot marks the initial position. Integration was backward for time of 1 Gyr.

pending on the symmetry of the underlying potential and the type of orbit, values of the orbital parameters can differ for individual cycles.

Most of the orbits in a realistic axisymmetric galactic potentials ($\phi(R, z)$, also the case of our basic potential described in Sect. 4.1) posses three integrals of motion – the z-component of angular momentum, L_z; the total energy; and a third, so-called, *non-classical* integral, which does not have a general analytical expression as a function of the phase-space variables (see Binney & Tremaine, 2008, Sect. 3.2). The 3-dimensional motion of such *regular orbit* can be reduced to the 2-dimensional motion in the (R, z) plane (the meridional plane), where it is restricted to a limited area defined for given potential by the orbit angular momentum and energy. Therefore, for every regular orbit, there are a physically limited ranges of R and z where the orbit is bounded. The values of orbital parameters are naturally also limited by these constrains.

In some axisymmetric potential, orbits that do not have the third non-classical integral of motion can exist. These are called *irregular orbits* (also chaotic or stochastic orbits). Irregular orbits can also be present when an axisymmetric potential is perturbed by a non-axisymmetric pattern. This is particularly the case if the orbit is near some resonance radius for a single pattern or near a resonance overlap for multiple rotating patterns (see Sect. 3.2.2). Since a chaotic behavior of orbits is expected in these regions, it is impossible to precisely recover or predict such an orbit on a longer time scale.

To see the current orbital history, we calculated the orbital parameters for the most recent cycle (defined by azimuthal change of 2π) for each set of initial conditions. Fig-

ure 5.1 shows the distributions of these orbital parameters. Figure 5.2 shows the orbit in the axisymmetric and the combined model with the initial conditions derived from the mean values of the input observational data (Table 5.2 and 5.1, respectively).

The orbits in models including only the bar or spiral arms differ only slightly (around 10% difference for their orbital parameters) from the results of the axisymmetric model (see distributions of orbital parameters in Fig. 5.1). With the increasing model complexity there is a trend of having a larger apogalacticon distance and a lower perigalacticon distance, which, in turn, yields a higher eccentricity. However, this is never higher than 0.33, which seems to make highly eccentric orbits for NGC 6791 implausible.

According to these calculations, NGC 6791 is not expected to move much outside the solar circle, at odds with some of the previous suggestions (see Sect. 5.1.3). The orbit is presently located close to its apogalacticon and this remains inside the solar circle on average, but never gets very close to the bulge. However, a scenario in which NGC 6791 formed close to the bulge and then migrated outward deserves a closer look, which we shall present in Sect. 5.2.

5.1.3 Comparison with previous orbit integrations

To our knowledge, the orbit of NGC 6791 was studied four times – by Carraro et al. (2006), Bedin et al. (2006), Wu et al. (2009), and by Vande Putte et al. (2010).

Carraro et al. (2006) used a complex potential derived from an N-body gas-dynamical model (Fux, 1997, 1999). They obtained an eccentric orbit ($e = 0.59$) extending far beyond the solar circle (up to about 20 kpc). However, the initial conditions were derived from absolute PM and radial velocity values available at that moment and admittedly less precise than the ones we use in this work. Therefore their results cannot be compared directly with these presented here.

Bedin et al. (2006) used a purely axisymmetric model of Allen & Santillan (1991) with the most up-to-date PM and radial velocity (the same values as we use here). However, reviewing the details of the initial conditions setup, we identified a problem (mis-definition of the x axis orientation), which prevents a proper comparison with our results.

Wu et al. (2009) calculated the orbit using the model of Allen & Santillan (1991) and two other axisymmetric potential models. As Carraro et al. (2006), they derived the initial conditions from less precise data than we use here. Still their orbital parameters for the Allen & Santillan (1991) potential are within uncertainties consistent with the results given in this study.

Similarly to Carraro et al. (2006) and Wu et al. (2009), Vande Putte et al. (2010) used an axisymmteric Galactic potential model (three-component model of Fellhauer et al., 2006, with the bulge modeled by a Hernquist potential, the disk as the Miyamoto-Nagai potential, and the halo represented by a logarithmic potential) and input data from the catalog of Dias et al. (2002a, version 2.10). They derived rather eccentric orbit with $e = (0.58 \pm 0.22)$ and vertical amplitude $|z|_{\max} = (1.4 \pm 1.1)$ kpc. Despite the difference in the initial conditions, these values are within their (rather large) uncertainties consistent with our results. As mentioned in Sects. 2.3 and 2.6.6, Vande Putte et al. (2010) presented a diagnostic method of a possible unusual origin of OCs based on values of their orbital

Table 5.3: Parameters of initial conditions distributions.

Coordinate	Distribution	Center	Dispersion, width
R	uniform	4.0 kpc	1.0 kpc
φ	equidistant distribution, 0–2π		
z	Gaussian	0 kpc	0.05 kpc
v_R	Gaussian	0 km s^{-1}	10 km s^{-1}
v_φ	Gaussian	$v_\mathrm{c}(R)$	6 km s^{-1}
v_z	Gaussian	0 km s^{-1}	4 km s^{-1}

Notes. We used the cylindrical Galactocentric coordinates – Galactocentric radius R, azimuth φ, vertical coordinate z, and corresponding velocities v_R, v_φ, v_z. The tangential velocity v_φ was calculated as the circular velocity $v_\mathrm{c}(R)$ in the axisymmetric potential described in Sect. 4.1 (even when the model includes a non-axisymmetric component) at a given radius and then a random velocity with the dispersion of 6 km s^{-1} was added.

parameters – vertical amplitude and eccentricity – together with their metallicities. For the case of NGC 6791, they suggested that the cluster might be due to an impact of a GC on the disk. This scenario would be supported with cluster metallicity resembling the disk value and they refer to [Fe/H]$= (0.11 \pm 0.10)$ dex (from the catalog of Dias et al., 2002a, version 2.10). However, the more up-to-date high-resolution spectroscopic studies favor a rather higher metallicity for NGC 6791 (about +0.4, see Sect. 2.6.2).

In any case, the present study supersedes any previous one, by adopting the non-axisymmetric Galactic models together with the initial conditions derived from the up-to-date observational data.

5.2 Forward orbits integration and radial migration

The inner disk, close to the bulge, is a high-density region where the star formation is very efficient and the metal enrichment fast (Bensby et al., 2010). It is therefore conceivable that NGC 6791 could formed there and then moved outward. To estimate the probability and efficiency of the resonance overlap radial migration mechanism, we carried out a forward orbits integration. More specifically, we integrated forward in time a number of orbits with an initial location close to the Galactic center. By comparing their orbital properties with the recent NGC 6791 orbital parameters obtained in Sect. 5.1, we attempted to estimate the probability that the radial migration moved the NGC 6791 orbit outward from the inner Galactic regions.

5.2.1 Initial setup

We followed 10^4 initially close-to-circular orbits distributed between 3 and 5 kpc from the Galactic center. First, the azimuth of the initial position vector was generated, with values equidistantly distributed over the full extend of 2π. Then, the radius was

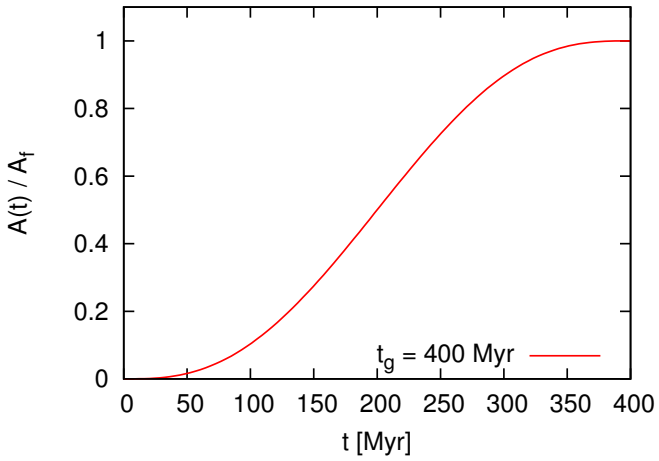

Figure 5.3: Gradual growth of the non-axisymmetric components amplitudes, given by Eq. (5.1) (Eq. (4) of Dehnen, 2000).

generated randomly for each azimuth, from a uniform distribution between 3 and 5 kpc. The vertical coordinate has a Gaussian distribution with dispersion of 50 pc, consistent with the exponential scale height estimated for the young OCs distribution (Piskunov et al., 2006; Bonatto et al., 2006, see Sect. 2.2). Finally, the initial velocity vector was generated to be close to the velocity vector for the circular orbit at given radius. The distributions of each velocity component is Gaussian with dispersion consistent to the one of observed young OCs (Piskunov et al., 2006). In Table 5.3 we give a summary and the numbers characterizing the initial conditions distributions.

To quantify the relative influence of different non-axisymmetric components, we followed the orbits in all four flavors of the Galactic potential model described in Sect. 4 (axisymmetric, barred, spiral, combined). When included, the amplitude of the non-axisymmetric component grows in time for 0.4 Gyr, from 0 to its maximum value with the time dependency described by Dehnen (2000, given by Eq. (4) there),

$$A(t) = A_{\mathrm{f}} \left(\frac{3}{16}\xi^5 - \frac{5}{8}\xi^3 + \frac{15}{16}\xi + \frac{1}{2} \right), \quad \xi = 2\frac{t}{t_{\mathrm{g}}} - 1, \tag{5.1}$$

where $A(t)$ denotes the time dependent amplitude, t_{g} is the time of the growth, and A_{f} is the final value of the amplitude (i.e., $A_{\mathrm{f}} = A(t_{\mathrm{g}})$). See Fig. 5.3 for the plot of the amplitude time dependency. If the spiral pattern is present in the model, the growth is realized by the time dependency of its density amplitude ρ_0. In the presence of the bar, its mass M_{B} is growing, while the mass of one of the central components M_{C_2} (Sect. 4.1.1) is decreasing in the opposite manner to complete the total common mass of the central component (when the model of Allen & Santillan, 1991 is used, the mass M_{C} is decreasing). The gradual growth of non-axisymmetric perturbations is introduced to allow a progressive adaptation of initially nearly circular orbits to the presence of the non-axisymmetric perturbations. The growth of a real bar and real spiral arms is certainly much more complex and not

Table 5.4: Parameters for MW models used for the forward integrations.

Parameter	MW1	MW2	Unit
Bar angular velocity $\Omega_{\rm B}$	60.0	45.0	$\mathrm{km\,s^{-1}\,kpc^{-1}}$
Bulge mass $M_{\rm C_2}$	0.62	0	$10^{10}\mathrm{M_\odot}$
Bar mass $M_{\rm B}$	0.98	1.6	$10^{10}\mathrm{M_\odot}$
Major semi-axis a	3.14	5.0	kpc
Spiral arms angular velocity $\Omega_{\rm SA}$	20	30	$\mathrm{km\,s^{-1}\,kpc^{-1}}$
Spiral arms amplitude ρ_0	3.36	5.14	$10^{7}\mathrm{M_\odot\,kpc^{-3}}$
Spiral arms pitch angle α	15.5	20.0	$^\circ$

Notes. Both models have the same form and are characterized by the same parameters as the model used for forward integrations described in Sect. 4 (denoted as model MW1 here). In the MW2 model, the listed parameters are changed (the rest of model parameters are kept the same as for MW1 model, see Table 4.3).

simultaneous, and modeling these time dependencies is beyond the scope of our model. We tested that our results are not significantly sensitive, apart from the first few hundreds of Myr, to the above gradual growth when compared to orbit integrations in which the bar or spiral arms were switched on abruptly to their full strength from the beginning.

According to Minchev & Famaey (2010), 3 Gyr should be time sufficient for the disk radial mixing. On the other hand, the age of NGC 6791 is estimated to be about 8 Gyr (Sect. 2.6.3). Therefore, we integrated the orbits forward in time for 8 Gyr. Finally, the orbital parameters were calculated for individual cycles of each orbit as described in Sect. 5.1.2.

5.2.2 *Migration tuned* MW model

Properties of the bar and spiral arms that we used for integrations of the orbit of NGC 6791 (as listed in Table 4.3) are based on the recent observations of the MW (Sect. 4). We indicate this present-day MW model as MW1 further in this manuscript. From N-body simulations and observations of external galaxies at various red-shifts, we can infer the evolution of bar and spiral arms with time. For example, owing to the expected increase of stellar velocity dispersion with time, the disk becomes more stable and thus its spiral structure weakens. On the other hand, gas inflow can cool down the disk and the spiral structure can strengthen again. Central mass concentrations (triggered, for example, by gas inflow) can decrease bar amplitudes (e.g., Athanassoula et al., 2005; Debattista et al., 2006) and even destroy bars, reforming later from the newly formed stars, but with a decreased strength and size (e.g., Bournaud & Combes, 2002; Combes, 2008).

Therefore, although we do not know the Galactic bar and spiral structure history, we can assume that those were stronger in the past. For this reason, we also followed orbits in a potential including stronger and faster spiral arms, as well as a stronger bar. This model is denoted as MW2. In Table 5.4 we list values of the parameters for that

Table 5.5: Most important resonance radii.

Resonance	MW1		MW2	
	bar	spiral arms	bar	spiral arms
$R_{\rm CR}$	3.6	12.3	5.1	8.1
$R_{\rm ILR}$	1.4	2.8	1.7	2.2
$R_{\rm OLR}$	6.9	20.4	9.4	13.9

Notes. Radii given in kpc – corotation, $R_{\rm CR}$; inner Lindblad resonance, $R_{\rm ILR}$; and outer Lindblad resonance, $R_{\rm OLR}$. Values for both non-axisymmetric components and both MW models are given. See Tables 4.3 and 5.4 for the angular velocities and other model characteristics.

the models MW1 and MW2 differ. We decided to show an example of a model that is deliberately tuned to favor the radial migration caused by stronger bar and spiral arms and also by the choice of the angular velocity of the spiral arms pattern, bringing its resonances closer to the Galactic center. We note that the parameter space (the bar and spiral arms shape, extent, strength, and pattern speed) within the framework of our test-particle integrations in analytically expressed potentials is very large and its systematic exploration is above the scope of our work.

In detail, for the MW2 model the bar semi-major axis is chosen to be longer, of 5 kpc (but the axis ratio for other two axes was kept as for MW1 model) and the bar itself is more massive – so that on the time scale of 0.4 Gyr it replaces the whole mass of the bulge. As a consequence, the strength parameter of this bar is 0.5. The spiral pattern is set to have a higher amplitude and higher pitch angle. The angular velocity of the bar is decreased to $45\,{\rm km\,s^{-1}\,kpc^{-1}}$. This brings the bar corotation radius to 5.1 kpc – so the ratio of the bar corotation radius to its semi-major axis is consistent with the value of 0.9–1.3 found in most barred galaxies (see paragraph 6.5.1 in Binney & Tremaine, 2008, and references therein). On the other hand, the spiral arms angular velocity is increased to $30\,{\rm km\,s^{-1}\,kpc^{-1}}$. The resonances of spiral arms are therefore closer to the Galactic center where the orbits are originally distributed. Table 5.5 lists the for resonance radii in both models.

5.2.3 Results

Before starting to comment more on the results of the forward integrations, we recall the reader that we aimed to search for similarities between the present-day orbital parameters of NGC 6791 and the orbital parameters of orbits that started close to the Galactic center and then migrated outward. If there were similarities, we could claim that the scenario in which NGC 6791 could form in the very inner disk is plausible also from a dynamical point of view, and supported not only by the observed chemical characteristics of the cluster.

The outcome of the forward integration experiments is illustrated in Figs. 5.4 – 5.9. Figs. 5.4 and 5.5 map the time evolution of the mean probability of finding an orbit with

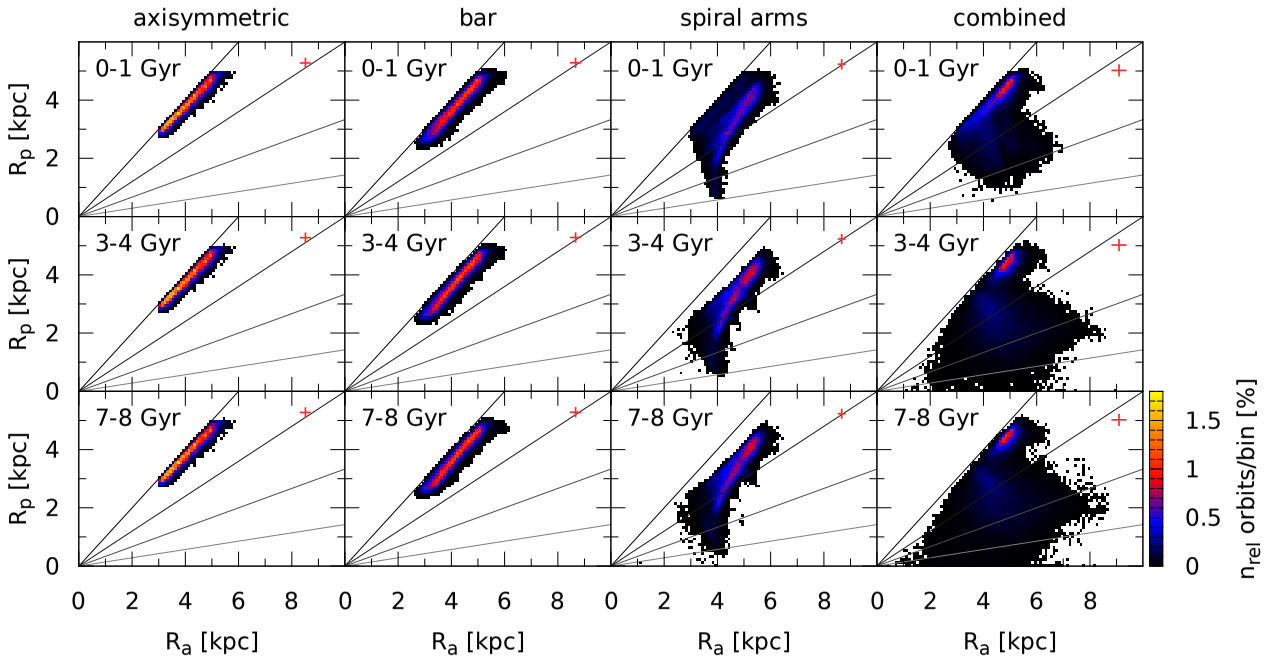

Figure 5.4: Time evolution of the apogalacticon distance R_a versus the perigalacticon distance R_p for the MW1 model. A mean probability of finding an orbit within a given bin of R_a and R_p is mapped (where the mean is calculated over the indicated 1 Gyr time interval). See text for the exact description of how the probability is calculated. The bin size is 0.1×0.1 kpc. Each column shows orbits for models including different components – axisymmetric model, model with bar, model with spiral arms, and bar and spiral arms combined model. Orbits are mapped within time intervals of 1 Gyr (0–1, 3–4, and 7–8 Gyr) as indicated in the left upper corner of each plot. The NGC 6791 values of R_a and R_p with their 3σ error-bars are plotted with the red cross in each plot. The four lines in each of the plots show the lines of constant eccentricity for values 0.0 (circular orbits), 0.25, 0.5, and 0.75, respectively, with decreasing slope.

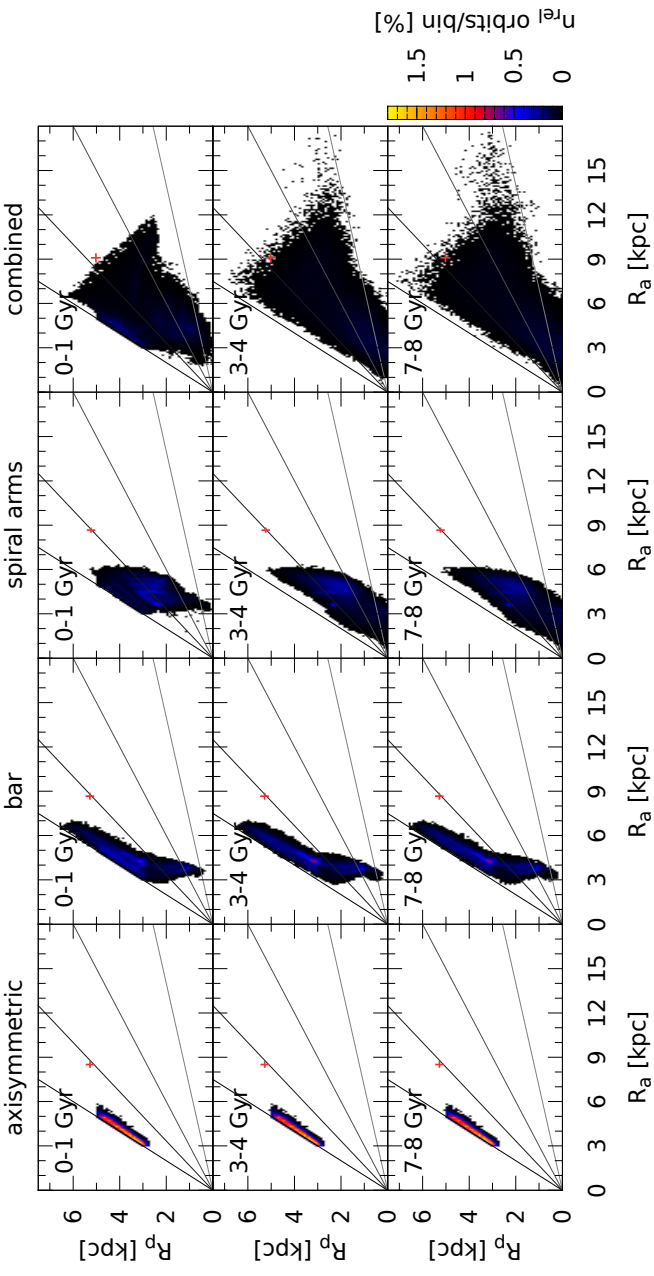

Figure 5.5: Time evolution of the apogalacticon distance $R_{\rm a}$ versus the perigalacticon distance $R_{\rm p}$ for the MW2 model. See Fig. 5.4 for a detailed description of the plot.

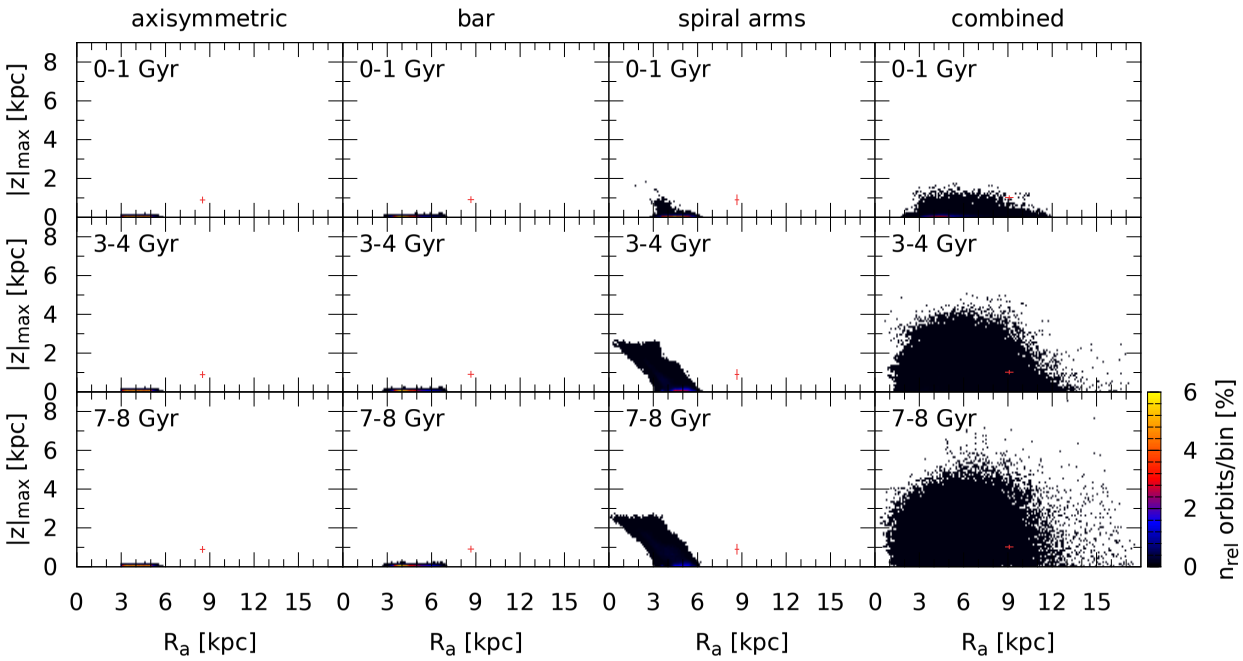

Figure 5.6: Time evolution of the apogalacticon distance R_a versus the vertical amplitude $|z|_\mathrm{max}$ for the MW2 model. See Fig. 5.4 for a detailed description of the plot.

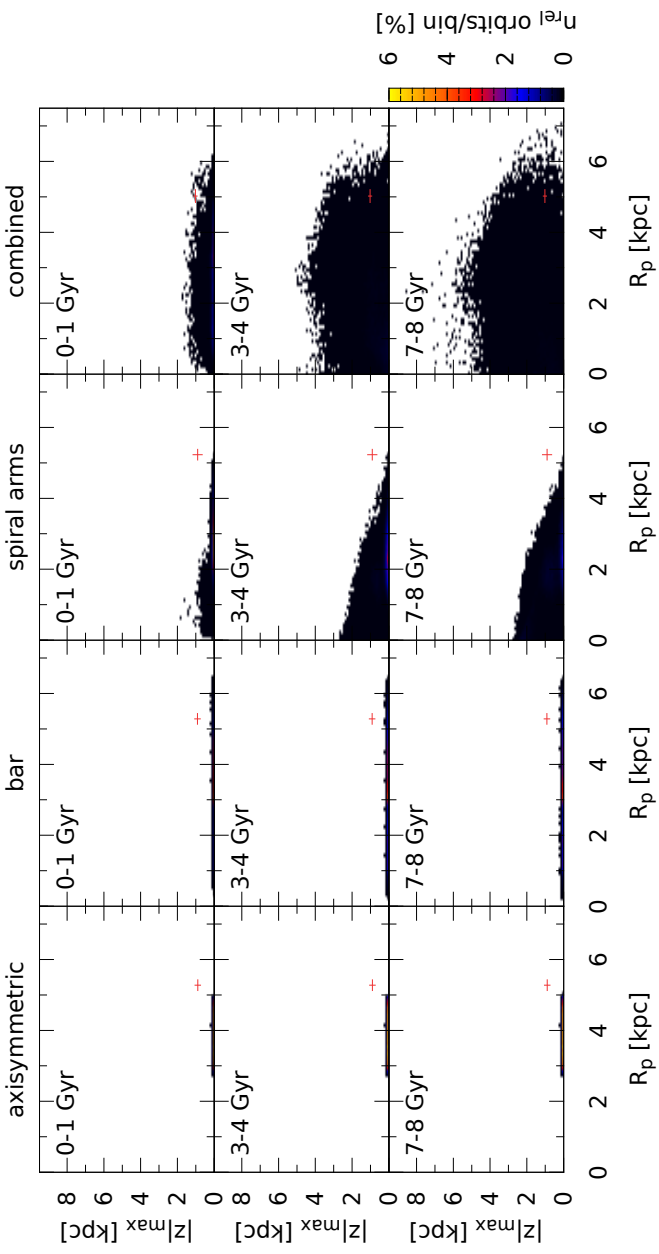

Figure 5.7: Time evolution of the perigalacticon distance R_p versus the vertical amplitude $|z|_\mathrm{max}$ for the MW2 model. See Fig. 5.4 for a detailed description of the plot.

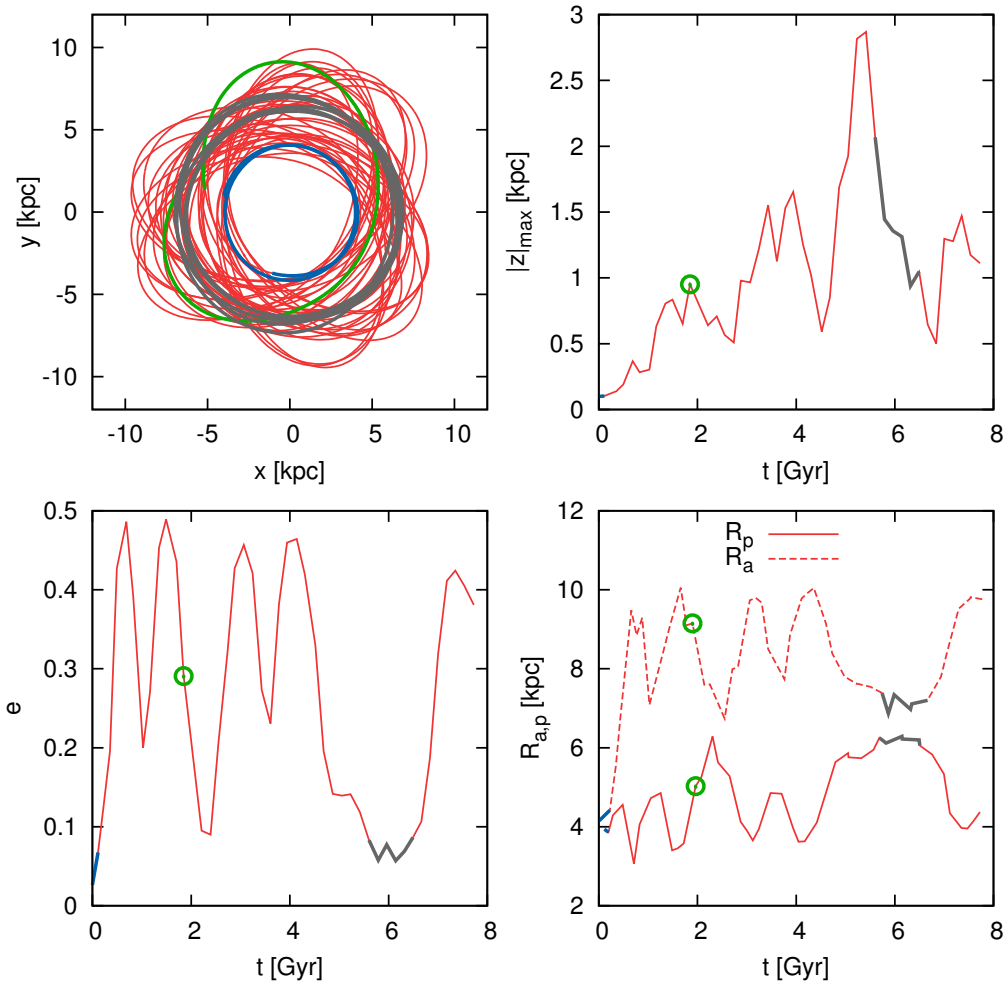

Figure 5.8: One of the orbits and its orbital parameters evolution calculated in the MW2 model including bar and spiral arms. The upper left plot shows the orbit in the Galactic plane; upper right plot shows the time evolution of the vertical amplitude; the bottom row shows the evolution of eccentricity, and the perigalacticon and apogalacticon distances in the left and right plot, respectively. For one of its cycles, this orbit fits the 3σ intervals for perigalacticon distance, apogalacticon distance, and vertical amplitude of the NGC 6791 orbit. This orbital cycle is highlighted in green in the plot of the orbit, and its orbital parameters are marked with the green circle symbols. Additionally, two other parts of the orbit are highlighted in blue and gray colors. The orbit is close-to-circular in both of these cases, however, it evolves from the initial radii of about 4 kpc (blue part) to radii about 7 kpc (gray part), having also a different vertical amplitude (0.1 and 1.5 kpc, respectively).

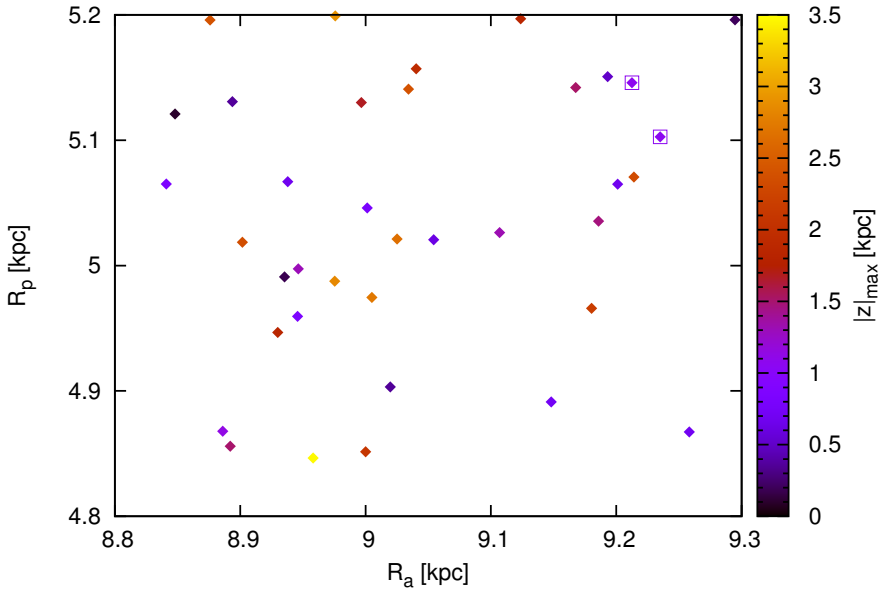

Figure 5.9: Apogalacticon distance R_a versus perigalacticon distance R_p for orbits integrated in the MW2 model during the time interval of 7–8 Gyr. The range of R_a and of R_p is limited to the 3σ intervals of values for NGC 6791. Each revolution with its R_a and R_p within these limits is shown by a point. The points are color-coded by the vertical amplitude $|z|_\mathrm{max}$. Revolutions that match NGC 6791 for all three orbital parameters (within their 3σ intervals) are marked with squared boxes.

a given combination of R_a and R_p. The probability is calculated for time intervals of 1 Gyr and for 0.1×0.1 kpc bins in the $R_\mathrm{a} \times R_\mathrm{p}$ space. For every given bin, the number of orbits with R_a and R_p values within the bin is calculated. The contribution of each orbit is further divided by the total number of cycles per the orbit within the time interval (so the total contribution of each orbit to each map is equal to 1). Finally, the probability is normalized to the total number of orbits 10^4 and converted to %. For the direct comparison with the recent orbital parameters of NGC 6791 we also indicate its values with the red cross in the maps. Figs. 5.6 and 5.7 map the mean probability of the vertical amplitude $|z|_\mathrm{max}$ versus R_a and R_p, respectively, for the MW2 model and they are calculated analogically as for the R_a versus R_p space.

As mentioned above, we chose the model MW2 to obtain an enhanced migration. Comparison of Figs. 5.4 and 5.5 shows that this is indeed the case, illustrated by the higher values of apogalacticon distance seen in Fig. 5.5. Moreover, some orbits have cycles with similar R_a and R_p as we derived for NGC 6791 (the position of the red cross in the R_a versus R_p plane is within the area populated by some of the forward integrated orbits).

From Figs. 5.6 and 5.7 we see that (only) the MW2 combined model can produce orbits that also show a vertical amplitude similar to NGC 6791. Only very few orbits (169 out of 10^4) can at least once per the total integration time of 8 Gyr reproduce the

R_a and R_p values similar to NGC 6791, and only some of these orbits (13 out of the 169) meet all three orbital parameters, R_a, R_p, and $|z|_{max}$, together. To investigate these orbits in more detail, we display all three orbital parameters together in Fig. 5.9, for the time interval of 7–8 Gyr of the integration.

The experiment with forward integrated orbits illustrated in Figs. 5.4 to 5.9 helps us to provide the following considerations:

- only the model MW2 that includes bar and spiral arms produces the apogalacticon distances, perigalacticon distances, and eventually also the vertical amplitude similar to the backward integration of the current orbit of NGC 6791 (see the maps for the combined model in the rightmost column of Figs. 5.4–5.7).

- Figure 5.8 shows an example of an orbit that migrated close to the recent NGC 6791 one. Initially, the orbit is close-to-circular with the radius of 4 kpc (in Fig. 5.8, this part of the orbit highlighted in blue), and later it starts to oscillate between very eccentric and close-to-circular again but has a radius of about 7 kpc (in Fig. 5.8, this part of the orbit highlighted in gray).

- from our experiment, we estimate the probability for the MW2 model including bar and spiral arms to produce the present orbit of NGC 6791 restricted to 2-dimensional Galactic plane (constrained by R_a and R_p) to be about 0.04% (during the total integration time of 8 Gyr). This probability is calculated in the same way as for the maps in Figs. 5.4–5.7: as a number of orbits reaching R_a and R_p within the 3σ intervals of NGC 6791, where the contribution of each orbit is divided by the total number of cycles per orbit within the total integration time of 8 Gyr (so the total contribution of each orbit is equal to 1). Finally, the probability is normalized to the total number of orbits 10^4. If the vertical amplitude is taken into account, the probability has even a lower value, below 0.01%.

5.3 Preliminary results on the initial mass

Based on the work of Lamers et al. (2005), we attempt to calculate a lower-limit estimate of the initial mass of NGC 6791. The initial mass is an important characteristics of any cluster, and it is particularly interesting for NGC 6791, in the context of its recently discovered abundance spread indicating the possible connection with GCs (Geisler et al., 2012, see Sects. 2.6.5 and 2.7). The approximative method of Lamers et al. (2005) cannot cover the real mass loss history for NGC 6791, however, it can provide a first approximation of this quantity and, to our knowledge, an estimate of the initial mass of NGC 6791 has not been presented so far.

Lamers et al. (2005) described an approximative solution for cluster disruption including the mass loss due to its stellar evolution and due to the two-body relaxation by the Galactic tidal field, provided its tidal strength is constant. The mass loss due to the stellar evolution and the tidal effects of galaxy, can be described as

$$\frac{\mathrm{d}M}{\mathrm{d}t} = \left(\frac{\mathrm{d}M}{\mathrm{d}t}\right)_{\mathrm{ev}} + \left(\frac{\mathrm{d}M}{\mathrm{d}t}\right)_{\mathrm{tidal}}, \tag{5.2}$$

where M is the cluster mass, and the subscripts *ev* and *tidal* denote the disruption due to stellar evolution and the Galactic tidal field, respectively.

Mass loss by stellar evolution

Mass loss due to stellar evolution of cluster members can be calculated using cluster evolution models. Lamers et al. (2005) used an approximation based on the Padova isochrones for a single stellar population with the Selpeter IMF with individual stars mass range of 0.15–85 $\mathrm{M}_\odot$. The fraction of cluster initial mass, $M_{\rm ini}$, lost due to the stellar evolution, $q_{\rm ev}(t) \equiv (\Delta M(t))_{\rm ev}/M_{\rm ini}$, can be approximated by a function (Eq. (2) from Lamers et al., 2005)

$$\log_{10} q_{\rm ev}(t) = (\log_{10} t - a)^b + c, \quad \text{for } t > 12.5 \text{ Myr}, \tag{5.3}$$

where t is the time in yrs, a, b, and c are coefficients of the approximation and are given for different cluster metallicities (see Table 1 in Lamers et al., 2005). The mass loss by the stellar evolution is then given by

$$\left(\frac{\mathrm{d}M}{\mathrm{d}t}\right)_{\rm ev} = -M(t)\frac{\mathrm{d}q_{\rm ev}}{\mathrm{d}t}. \tag{5.4}$$

Mass loss by galactic tidal field

Baumgardt & Makino (2003) calculated a set of N-body simulations of cluster disruption due to the tidal field; calculations were carried out for different cluster initial masses and different density profiles, and for clusters following circular and elliptical orbits at various Galactocentric radii. Gieles et al. (2004) have shown that the disruption time scale, $t_{\rm dis}$ – defined as $t_{\rm dis} \equiv (\mathrm{d}\ln M/\mathrm{d}t)^{-1}$ – for the theoretical models of Baumgardt & Makino (2003) can be expressed as an exponential function of the cluster mass, $t_{\rm dis} = t_0 M^\gamma$. t_0 is a normalization constant – the dissolution time scale parameter – and is determined by the tidal field strength (it is constant for a cluster on a circular orbit). The exponent γ is a dimensionless index defining the mass dependence of the disruption time scale. It depends on the cluster density profile and has typical values of about 0.6–0.8 from the theoretical studies (Baumgardt & Makino, 2003; Gieles et al., 2004), as well as from the observations (Boutloukos & Lamers, 2003). The mass loss by the galactic tidal field can be then expressed as

$$\left(\frac{\mathrm{d}M}{\mathrm{d}t}\right)_{\rm tidal} = -\frac{M}{t_{\rm dis}} = -\frac{M^{1-\gamma}}{t_0}. \tag{5.5}$$

Constant tidal field

Lamers et al. (2005, their Eq. (6)) presented an analytical formula that very accurately approximates the solution of Eq. (5.2) in the case of the constant dissolution time scale t_0,

$$\frac{M(t)}{M_{\rm ini}} \simeq \left\{[1 - q_{\rm ev}(t)]^\gamma - \frac{\gamma t}{t_0} M_{\rm ini}^{-\gamma}\right\}^{1/\gamma}, \tag{5.6}$$

where the cluster (initial) mass is given in $M_\odot$. If the first term in brackets, describing the mass that remains after the mass loss due to stellar evolution, is smaller than the second term, describing the mass loss due to the Galactic tidal field, than $M(t) = 0$ and the cluster is completely disrupted. Cluster initial mass can be expressed by inverted Eq. (5.6) as

$$M_{\rm ini} \simeq \left[M^\gamma + \frac{\gamma t}{t_0}\right]^{1/\gamma} [1 - q_{\rm ev}(t)]^{-1}\,, \tag{5.7}$$

where, again, masses are expressed in $M_\odot$.

The first estimate on the initial mass of NGC 6791 (or the mass loss up to certain time) can be made following the results of Lamers et al. (2005) given by Eqs. (5.6) and (5.7). This corresponds to the case when the tidal field can be assumed to be constant (cluster on a circular orbit) during the whole cluster life. Looking at its suggested origin scenarios (Sect. 2.6.6) and the results of previous sections, this does not seem very probable for NGC 6791. However, the initial mass calculated via Eq. (5.7) can serve as a conservative lower-limit estimate of the real value.

To calculate Eq. (5.7), we need to assess values of the involved constants characterizing the cluster and the Galactic tidal field. The parameters a, b, and c determine the mass loss rate due to stellar evolution, Eq. (5.3), and depend on cluster metallicity. Lamers et al. (2005) give their values for metallicity in the range $0.0004 < Z < 0.05$ in their Table 1. The [Fe/H] abundance of NGC 6791 is about +0.4 (Sect. 2.6.2), which corresponds to Z [1] of about 0.05 and leads to values of $a = 0.05$, $b = 0.25$, and $c = -1.82$.

The dissolution time scale parameter t_0 determines the mass loss rate due to the given tidal field and is assumed to be constant. Comparing the observed age distribution of OCs in the solar neighborhood, with the theoretical one predicted through Eq. (5.6), Lamers et al. (2005) obtained $t_0 = 3.3^{+1.4}_{-1.0}$ Myr (corresponding to the disruption time of 1.3 ± 0.5 Gyr for a cluster with the initial mass of $10^4 M_\odot$). This value is about a factor five shorter than obtained by Baumgardt & Makino (2003) from their N-body simulations (they obtained the disruption time of 6.9 Gyr for a $10^4 M_\odot$ cluster). Lamers & Gieles (2006) have shown that this discrepancy is probably mostly because Lamers et al. (2005) did not include the mass loss due to the tidal shocks. When the tidal shocks (interaction with GMCs and spiral arms) are considered, the observed age distribution of OCs is reproduced using the dissolution time scale consistent with Baumgardt & Makino (2003). Therefore, the value of $t_0 = 3.3^{+1.4}_{-1.0}$ Myr by Lamers et al. (2005) – which is shorter than the actual time scale for two-body relaxation due to the Galactic tidal field – could successfully reproduce the observed age distribution of OCs in the solar neighborhood, even though the shocks were not included. Since the current Galactocentric radius of NGC 6791 is about 8 kpc that roughly corresponds to solar distance, we adopt the t_0 of Lamers et al. (2005), which through its shorter value, in a way, also covers the tidal shock interaction.

For the coefficient γ, we adopt the value of 0.62 which corresponds to a typical OCs (e.g., Kruijssen et al., 2011). The exponent γ depends on the cluster mass density profile

[1] The proportion of matter of an object made up from chemical elements other than hydrogen and helium.

and is usually given for different values of the King parameter W_0, which characterizes the concentration of the King models (King, 1966). The typical value of King parameter for OCs is $W_0 = 5$ and it corresponds to $\gamma = 0.62$ (e.g., Baumgardt & Makino, 2003). GCs are generally more concentrated with $W_0 = 7$ (Kruijssen & Mieske, 2009), which corresponds to $\gamma = 0.70$. To our knowledge, the only presented density profile and King model of NGC 6791 is the one by Platais et al. (2011). They constructed a stellar number density profile complete to $g' \sim 22$ mag, within the radius of $15'$ from the cluster center. They derived the King parameter $W_0 = (3.4 \pm 0.3)$, a value rather low compared to a typical OCs. A possible cause of this discrepancy might be that while the cluster tidal radius is estimated to be $(23.1 \pm 1.0)'$, the density profile was constructed using data within the radius of only $15'$. Estimating the tidal radius beyond the radial extend of the available data is rather unstable and the real tidal radius of the cluster might be larger. We constructed the stellar number density profile independently using the catalog of Stetson et al. (2003, about 15 000 stars up to $V \sim 24$ mag). The radial range of the density profile is up to about $12'$ from the cluster center and the we estimate the tidal radius to be $(18 \pm 5)'$. So the data suffer from the same spatial incompleteness with respect to the tidal radius as in the work of Platais et al. (2011). Our best fitting King model has the concentration parameter consistent with the result of Platais et al. (2011), however, we expect the real King parameter of NGC 6791 to be larger. Furthermore, the exponent γ is not estimated for system with that low concentration since such systems with $W_0 \sim 3$ are predicted to disrupt rapidly by mass loss due to stellar evolution (e.g., Baumgardt & Makino, 2003). Therefore we use $\gamma = 0.62$ as predicted for a typical OC.

Apart from the parameters characterizing the mass loss process, Eq. (5.7) is calibrated by a known cluster mass at a given time, i.e., the cluster current mass and its current age. We adopt values of 5000 $M_\odot$ and 8 Gyr for these quantities, respectively (Sects. 2.6.1 and 2.6.3). Even though, precise values are still under discussion and these numbers posses significant errors, the final uncertainty in the initial mass estimate is driven mostly by the uncertainty in the dissolution time scale parameter t_0. The dependence of the cluster initial mass for the dissolution time scale parameter t_0 within the range of $3.3^{+1.4}_{-1.0}$ Myr is plotted in Fig. 5.10, together with the uncertainties caused by the error of the current cluster mass (interval 4000–6000 $M_\odot$ considered) and its current age (interval 7–9 Gyr considered).

Figure 5.10 shows that the estimate of NGC 6791 initial mass is about $(1.5\text{–}4)\cdot 10^5 M_\odot$. This mass range was estimated using Eq. (5.7), which assumes a constant Galactic tidal field with its strength corresponding to the solar neighborhood. Eq. (5.7) does not includes the tidal shocks directly, but it indirectly covers the tidal shock interaction through a shorter dissolution time scale. The mass range of $(1.5\text{–}4) \cdot 10^5 M_\odot$ can be consider as a lower-limit estimate of the real value of the initial mass of NGC 6791. This is interesting in the context of the theoretical considerations about the initial mass of GCs as mentioned in Sect. 2.7. Bekki (2011) suggested that the limiting initial mass necessary for the system to form the second stellar generation, and consequently to show the abundance spread – observed also in the case of NGC 6791 (Sect. 2.6.5) – is $(6\text{–}10) \cdot 10^5\, M_\odot$; Vesperini et al. (2010) obtained a slightly lower value of $\sim 10^{4.8}$–$10^5\, M_\odot$. Our lower-limit estimate lies somehow in between these theoretically derived limits, suggesting that NGC 6791 proba-

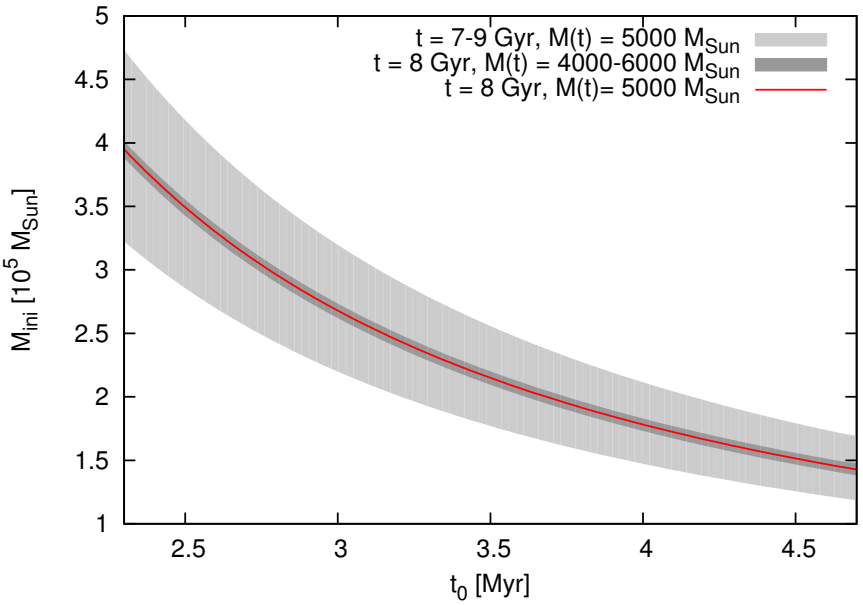

Figure 5.10: Cluster initial mass given by Eq. (5.7) as a function of the dissolution time scale parameter t_0. The red curve shows the dependence derived for the current cluster mass of 5000 $M_\odot$ and its age of 8 Gyr; the dark-gray colored area corresponds to values derived for mass within 4000–6000 $M_\odot$ at age of 8 Gyr; the light-gray area corresponds to values derived for the mass of 5000 $M_\odot$ at an age within 7–9 Gyr.

bly had the initial mass sufficient to form the second stellar generation and is resembling the evolution of GCs in this aspect. However, the analysis done here is only the very basic one and the topic of the cluster initial mass deserves a more realistic investigation (including the galactic tidal effects corresponding to a more realistic orbit and the tidal shocks).

Chapter 6

Orbits of open clusters

With the increasing quality and quantity of available data, several works investigated the chemical properties and the radial metallicity gradients of the Galactic disk as defined by OCs using a sample having abundances obtained by various high-resolution spectroscopy studies (see Sect. 2.5.1 for the literature summary). Among others, Magrini et al. (2009) studied a sample of 45 OCs with their Galactocentric radii of 7–22 kpc and compared their characteristics with a *classical* chemical evolution model of the Galactic disk (a model based on assumptions similar to these described in Sect. 3.1). The same model was used by Magrini et al. (2010), who focused on the inner disk properties using a sample of 11 OCs with their radii within the range of 6.5–8 kpc. Pancino et al. (2010) collected abundances for 57 OCs, and this sample was further extended by Carrera & Pancino (2011) to 89 OCs. Yong et al. (2012) compiled the high-resolution abundances for 49 OCs. As described in Sect. 2.5.1, these studies generally reach consistent results, with the main conclusions of the slope change of the radial metallicity gradient; with no significant difference of the metallicity gradient between younger and older OCs (or only a slightly more flat gradient for the younger OCs); as well as with no significant gradients with the vertical distance from the Galactic plane (Sect. 2.5.2); and with a lack of the AMR (Sect. 2.5.3).

Kinematics and orbital properties are an important part of clusters characterization, together with the chemical composition, spatial distribution, or the age. Orbital properties can bring an insight into clusters origin and evolution in the context of the Galactic disk (Sect. 2.5.1). As mentioned in Sect. 2.3, many authors investigated orbits of OCs. The most recent systematical studies are by Wu et al. (2009) or Vande Putte et al. (2010), who both used the catalog of Dias et al. (2002a, its version available by the time of their study) as the main source of the input data and other clusters characteristics (metallicity and age). Both studies also included an analysis and discussion of clusters orbital characteristics in the connection with their metallicity. The metallicities in the catalog of Dias et al. (2002a) are compiled from various sources for individual clusters, and no distinction between the quality of the metallicity measurements was made. Therefore,

their conclusions could be influenced by the less precise measurements (e.g., metallicities obtained from the CMDs or the low-resolution spectroscopy). Wu et al. (2009) compared the radial metallicity gradient for OCs currently located at $R < 13.5\,\mathrm{kpc}$ derived using their current Galactocentric radii and the apogalacticon distances of their orbits, finding both to be similar, $(-0.07 \pm 0.011)\,\mathrm{dex\,kpc^{-1}}$ and $(-0.082 \pm 0.014)\,\mathrm{dex\,kpc^{-1}}$, respectively (see Sect. 3.2.4 for a consequent discussion). Vande Putte et al. (2010) suggested that the orbital parameters of the maximal vertical amplitude and eccentricity can be correlated with the metallicity and might be used as indicators of individual clusters origin; see Sect. 2.3 for a more detailed summary, and Sect. 5.1.3 where their result for the case of NGC 6791 is discussed.

In this chapter, we present orbits for a sample of 34 OCs. The main selection criterion for the sample was the availability of at least one high-resolution metallicity measurement in the literature. Further, we obtained a new mean PM vector estimates based on the UCAC4 catalog for all clusters in the sample. Although, the mean PM vector is available in the literature almost for all sample clusters, sometimes the values are obtained using only few stars (less then 10). Therefore, we carried out an independent analysis to obtain the mean PM vectors for all sample clusters in a consistent way. The description of the methods used to obtain the mean PM vectors is given in Sect. 6.3 and a comparison of our results with previous studies in Sect. 6.4.1. To calculate the orbits, we also collected up-to-date solar distances and radial velocities of the OCs in our sample.

We calculated orbits for the sample clusters in our model of the Galactic potential (including non-axisymmetric components, see Sect. 4 for the model description) and analyzed orbital properties in the context of their high-resolution metallicities (Sect. 6.5.2). To our knowledge, with the exception of Magrini et al. (2010), where we used the Allen & Santillan (1991) version of our barred model to calculate orbits of the inner disk sample of 11 OCs, none of the previous studies have investigated orbits of a sample of OCs in a non-axisymmetric Galactic potential model.[1]

6.1 Sample of clusters

As already mentioned, the key selection criteria for our OCs sample is the availability of a high-resolution spectroscopic metallicity measurement. Carrera & Pancino (2011) found about 90 of such systems with $R \geq 15\,000$,[2] which is, to our knowledge, the biggest sample compiled. We investigated the mean PM vector for these clusters using the UCAC4 catalog (Zacharias et al., 2012a) as the source of the PM data for individual stars, and using the methods described in Sect. 6.3. It was possible to obtain reliable PM information for our final sample of 34 OCs.

[1] 48 GCs in a barred potential have been investigated by Allen et al. (2006); 6 GCs in combined bar and spiral arms model by Allen et al. (2008). Both studies used the bar model presented by Pichardo et al. (2004) and the spiral arm model of Pichardo et al. (2003) together with the Allen & Santillan (1991) axisymmetric background. Similar model was also used by Bellini et al. (2010a) to calculate the Galactic orbit of the OC M 67, and by Pichardo et al. (2012) to investigate and compare the present-day orbital characteristics of the Sun and M 67.

[2] The spectral resolution or spectral resolving power, R, of a spectrograph is defined by the smallest difference in wavelength, $\Delta\lambda$, that can be distinguished at a wavelength λ: $R = \lambda/\Delta\lambda$.

Table 6.1: Characteristics of OCs collected from the literature.

Cluster	$d_\odot$ [pc]	$\sigma_{d_\odot}$	Ref. $d_\odot$	age [Gyr]	$\sigma_{\rm age}$	Ref. age	v_r [km s^{-1}]	σ_{v_r}	Ref. v_r
Blanco 1	207	12	(28)	0.132	0.024	(38)	+5.53	0.11	(24)
IC 2602	149	2	(28)	0.046	0.006	(29)[g]	+18.12	0.30	(24)
IC 4651	1010	50	(21)	1.7	0.2	(21)	−30.76	0.2	(21)
Melotte 66	4370	600	(7)[d]	4.0	1.0	(7)	+21.2	0.4	(15)[e]
Melotte 71	2090	210	(33)	0.9	0.1	(33)	+50.71	0.12	(8)
NGC 188	1700	80	(18)	7.0	0.5	(18)	−42.36	0.04	(19)
NGC 752	450	20	(17)	1.2	0.2	(10)	+5.04	0.08	(8)
NGC 1039	540	40	(34)	0.23	0.03	(35)[i]	−16.8	0.01	(36)
NGC 1545	711	70	(32)[h]	0.089	0.005	(39)	−11.58	0.17	(8)
NGC 1817	1510	420	(16)	1.1	0.1	(16)	+65.31	0.09	(8)
NGC 2099	1490	120	(14)	0.49	0.03	(14)	+8.3	0.2	(8)
NGC 2204	4100	400	(11)	2.0	0.3	(10)	+89.09	1.2	(9)[c]
NGC 2243	3600	200	(9)	4.7	1.2	(10)	+57.7	0.2	(9)[b]
NGC 2355	1930	130	(13)	0.8	0.2	(10)	+35.4	0.5	(13)
NGC 2360	1887	190	(32)[h]	0.85	0.15	(10)	+27.28	0.18	(8)
NGC 2420	2500	300	(13)	2.2	0.3	(10)	+73.6	0.6	(13)
NGC 2447	1050	40	(40)	0.4	0.05	(40)	+22.08	0.18	(8)
NGC 2477	1260	230	(7)[d]	1.0	0.3	(7)[a]	+7.26	0.12	(8)
NGC 2539	1100	110	(41)	0.63	0.06	(41)[d]	+28.89	0.21	(8)
NGC 2632	180	10	(10)	0.7	0.1	(10)	+34.76	0.07	(24)
NGC 2660	2750	130	(23)	1.0	0.3	(23)[f]	+21.2	0.6	(6)
NGC 2682	850	40	(20)	4.2	0.7	(20)	+33.67	0.09	(20)
NGC 3114	920	50	(42)	0.16	0.02	(43)[j]	−1.72	0.13	(8)
NGC 3680	1100	50	(30)	1.75	0.1	(31)	+1.28	0.11	(8)
NGC 3960	2090	100	(5)	0.9	0.3	(5)	−22.6	0.9	(6)
NGC 5822	805	60	(44)	0.9	0.1	(44)	−29.31	0.18	(8)
NGC 6134	1050	60	(25)	0.79	0.10	(25)	−25.70	0.19	(8)
NGC 6192	1660	150	(26)	0.13	0.03	(26)	−7.93	0.21	(8)
NGC 6253	1620	190	(1)	3.0	0.5	(1)	−29.4	1.3	(2)
NGC 6475	340	20	(36)	0.2	0.05	(36)	−14.78	0.23	(24)
NGC 6633	400	20	(44)	0.56	0.07	(45)[g]	−28.96	0.09	(8)
NGC 6705	1890	260	(27)	0.25	0.03	(27)	+35.08	0.32	(8)
NGC 6819	2340	60	(3)	2.2	0.2	(3)	+2.34	0.05	(4)
NGC 7789	2200	200	(12)	6.3	0.3	(10)	−54.7	1.3	(13)

Notes. [(a)] Originally, Kassis et al. (1997) estimated the age of $1^{+0.3}_{-0.2}$ Gyr; we took the larger error. [(b)] The mean value (and its dispersion) of RVs of 16 member stars presented in Jacobson et al. (2011a) is used; this result agrees well with the result of Mermilliod et al. (2008a, $(+59.84 \pm 0.41)\,\mathrm{km\,s^{-1}}$, based on 2 member stars), and Friel et al. (2002, $(+55 \pm 5)\,\mathrm{km\,s^{-1}}$, based on the mid-resolution spectroscopy of 9 stars). [(c)] Mean value (and its dispersion) of RVs of 18 member stars presented in Jacobson et al. (2011a) is used; this result is consistent with the result of Mermilliod et al. (2008a, $(+92.35 \pm 0.52)\,\mathrm{km\,s^{-1}}$, based on 25 member stars). [(d)] Asymmetrical interval of the distance modulus estimated by Kassis et al. (1997); we took the larger error to estimate the uncertainty in the distance (Melotte 66: the distance modulus of $13.2^{+0.3}_{-0.1}$ mag, error of 0.3 mag taken; NGC 2477: the distance modulus of $10.5^{+0.4}_{-0.3}$ mag, error of 0.4 mag taken). [(e)] Avarage value (and its dispersion) of RVs of 5 member stars presented in Sestito et al. (2008) is used; this result compares well with an older estimate by Friel & Janes (1993) of $(+23 \pm 6)\,\mathrm{km\,s^{-1}}$, based on a mid-resolution spectroscopy of 4 stars. [(f)] Age interval of (1.0±0.3) Gyr taken to cover the best age estimates resulting from various isochrone models presented in Table 4 of Sandrelli et al. (1999).

$^{(g)}$ Asymmetrical interval for age error given by Jeffries et al. (2002); we take the larger error to estimate the uncertainty. $^{(h)}$ There is no error estimate given in Kharchenko et al. (2005a, where they refer to private communication with Loktin, 2004, as the source of the distance estimate). We adopt the distance uncertainty of 10%. $^{(i)}$ Jones & Prosser (1996) estimated the age to be within the interval of 200–250 Myr, which we take as (0.23 ± 0.3) Gyr. $^{(j)}$ No uncertainty of age is given in the source paper of González & Lapasset (2001, and to our knowledge, none of the more recent studies of the cluster gives the age uncertainty estimate); we take the uncertainty of 10%.

References. (1) Twarog et al. (2003); (2) Anthony-Twarog et al. (2010); (3) Basu et al. (2011); (4) Hole et al. (2009); (5) Bragaglia et al. (2006); (6) Sestito et al. (2006); (7) Kassis et al. (1997); (8) Mermilliod et al. (2008a); (9) Jacobson et al. (2011a); (10) Salaris et al. (2004); (11) Twarog et al. (1997); (12) Gim et al. (1998); (13) Jacobson et al. (2011b); (14) Hartman et al. (2008); (15) Sestito et al. (2008); (16) Balaguer-Núñez et al. (2004a); (17) Daniel et al. (1994); (18) Sarajedini et al. (1999); (19) Geller et al. (2008); (20) Yadav et al. (2008); (21) Meibom et al. (2002); (22) Pietrukowicz et al. (2006); (23) Sandrelli et al. (1999); (24) Mermilliod et al. (2009); (25) Rasmussen et al. (2002); (26) Loktin et al. (2001); (27) Santos et al. (2005); (28) van Leeuwen (2009); (29) Dobbie et al. (2010); (30) Bruntt et al. (1999); (31) Anthony-Twarog et al. (2009); (32) Kharchenko et al. (2005a); (33) Twarog et al. (2006); (34) Sarajedini et al. (2004); (35) Jones & Prosser (1996); (36) Kharchenko et al. (2007); (37) Villanova et al. (2009); (38) Cargile et al. (2010); (39) Začs et al. (2011); (40) Bica & Bonatto (2005); (41) Choo et al. (2003); (42) Carraro & Patat (2001); (43) González & Lapasset (2001); (44) Carraro et al. (2011); (45) Jeffries et al. (2002); (45) Williams & Bolte (2007).

Clusters are listed in Table 6.1, together with their characteristics – solar distance $d_\odot$, radial velocity v_r (necessary for the initial conditions calculation), and their age. Values of these quantities and their uncertainties were collected from the literature (the references are also given in Table 6.1). Clusters in the sample have solar distances within the range of 0.1–4.4 kpc. No study providing the distances, radial velocities, or age estimates in a consistent way for all these clusters is available. Therefore, we collected the information from various sources, which generally used different methods to obtain these characteristics. For each cluster, we searched for the most up-to-date information available and when more than one source was available, we checked through the various studies and aimed to use the most reliable estimate.[3]

Figure 6.1 shows the spatial distribution of OCs in our sample. Comparing the left plot of Fig. 6.1, showing the distribution in the Galactic plane, to Fig. 2.1, panel (d), we can see similarity with the distribution of a much bigger sample of 654 OCs in the Galactic plane (from Bonatto et al., 2006).

6.2 Metallicity of sample clusters

For all clusters in our sample, at least one study of metallicity using a high-resolution spectroscopy is available, however, some clusters were analyzed more than once. In these multiple cases, we decided to use the result with the smaller uncertainty. In the cases when more studies give the same uncertainty, we chose the result using a higher number

[3] Characteristics of OCs are also collected in various catalogs, such as the catalog of Dias et al. (2002a) or the WEBDA database (Sect. 2.2). However, the uncertainties of some characteristics (e.g., the solar distance, necessary to estimate uncertainties in orbital parameters, Sect. 5.1.1) are not listed in these compilations and therefore we preferred to collect the information directly from the original studies.

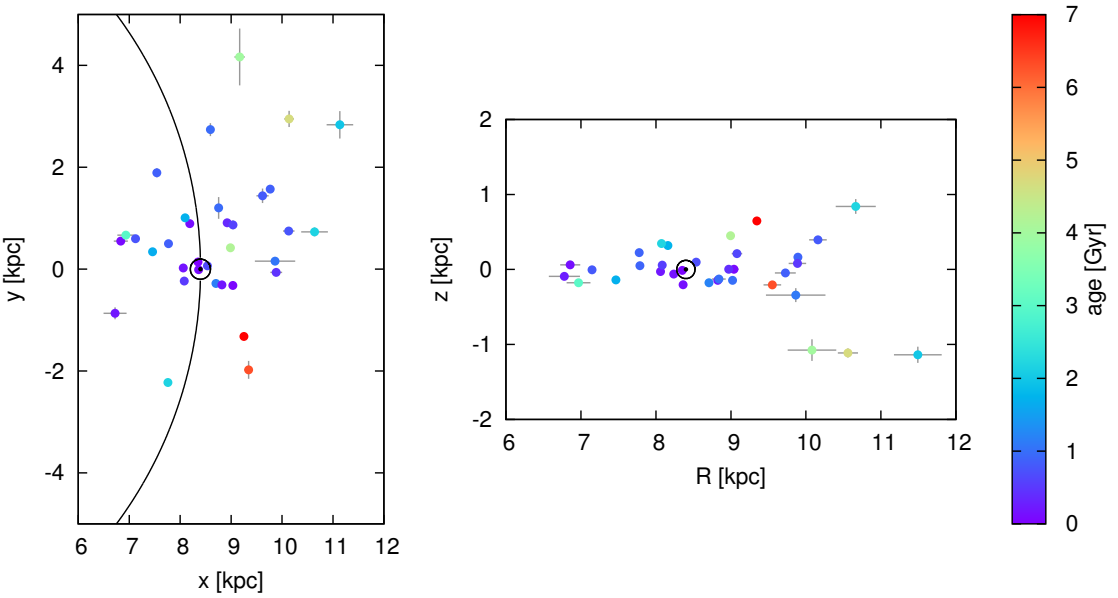

Figure 6.1: Spatial distribution of OCs in our sample color-coded by their age. The coordinate system is the one defined in Sect. 5.1.1 (Cartesian Galactocentric right-handed coordinates, where the x axis points from the Galactic center outward, in the direction of the Sun; the y axis points in anti-direction of the LSR motion; and the z axis toward the North Galactic Pole). Symbol $\odot$ marks the position of the Sun. *Left:* Distribution in the Galactic plane. The black curve shows the solar circle with the radius of 8.4 kpc. *Right:* Distribution in the meridional plane.

of cluster member stars to derive the mean cluster metallicity. Generally, the results of different studies are consistent within their errors.

The literature data on [Fe/H] for clusters in the sample are given in Table 6.2. We note that our literature search was not exhaustive and a different criterion could be used for the metallicity selection in the multiple cases. These could also be treated as independent measurements (e.g., Pancino et al., 2010 or Yong et al., 2012), averaged with equal weights (Carrera & Pancino, 2011), or averaged with some kind of weighting system (based, for example, on the number of stars used in the different studies, the uncertainty of metallicity, or the spectral resolution).

6.3 Clusters mean PM vectors

Mean PM vector for each cluster in the sample was obtained using data of individual stars from the UCAC4 astrometric catalog. The description of UCAC4 was given by Zacharias et al. (2012a). It is the final release in the UCAC series, covering all-sky by over 110 million of objects with PMs supplemented by the photometry from The Two Micron All Sky Survey (2MASS, Skrutskie et al., 2006). It is complete to about 16 mag

Table 6.2: Clusters Galactocentric radii and metallicity.

Cluster	R [kpc]	σ_R	[Fe/H]	$\sigma_{[Fe/H]}$	#	Ref.
Blanco 1	8.36	0.00	+0.04	0.04	8	Ford et al. (2005)
IC 2602	8.35	0.00	−0.05	0.05	9	Randich et al. (2001)
IC 4651	7.47	0.04	+0.11	0.01	4	Carretta et al. (2004)
Melotte 66	10.08	0.32	−0.33	0.03	5	Sestito et al. (2008)
Melotte 71	9.89	0.02	−0.32	0.16	2	Brown et al. (1996)
NGC 188	9.35	0.05	+0.12	0.02	4	Friel et al. (2010)
NGC 752	8.71	0.01	+0.01	0.04	18	Sestito et al. (2004)
NGC 1039	8.82	0.03	+0.07	0.04	5	Schuler et al. (2003)
NGC 1545	9.04	0.06	−0.13	0.08	3	Začs et al. (2011)
NGC 1817	9.86	0.40	−0.16	0.03	28	Jacobson et al. (2011b)
NGC 2099	9.89	0.12	+0.01	0.05	3	Pancino et al. (2010)
NGC 2204	11.49	0.32	−0.23	0.04	13	Jacobson et al. (2011a)
NGC 2243	10.56	0.14	−0.42	0.05	10	Jacobson et al. (2011a)
NGC 2355	10.16	0.12	−0.08	0.08	5	Jacobson et al. (2011b)
NGC 2360	9.73	0.14	−0.07	0.06	4	Reddy et al. (2012)
NGC 2420	10.66	0.27	−0.20	0.06	9	Jacobson et al. (2011b)
NGC 2447	8.97	0.02	−0.10	0.03	3	Santos et al. (2009)[a]
NGC 2477	8.84	0.09	+0.07	0.03	6	Bragaglia et al. (2008)
NGC 2539	9.08	0.07	+0.13	0.03	3	Santos et al. (2009)[a]
NGC 2632	8.54	0.01	+0.16	0.05	3	Carrera & Pancino (2011)
NGC 2660	9.02	0.05	+0.04	0.04	5	Bragaglia et al. (2008)
NGC 2682	9.00	0.03	+0.03	0.01	10	Randich et al. (2006)
NGC 3114	8.24	0.01	+0.02	0.05	3	Santos et al. (2009)[a]
NGC 3680	8.16	0.01	−0.08	0.02	21	Anthony-Twarog et al. (2009)
NGC 3960	7.78	0.02	+0.02	0.04	6	Bragaglia et al. (2008)
NGC 5822	7.79	0.04	+0.05	0.04	3	Santos et al. (2009)[a]
NGC 6134	7.15	0.05	+0.15	0.07	3	Carretta et al. (2004)
NGC 6192	6.86	0.13	+0.12	0.04	4	Magrini et al. (2010)
NGC 6253	6.97	0.16	+0.36	0.07	5	Sestito et al. (2007)
NGC 6475	8.06	0.02	+0.14	0.06	13	Sestito et al. (2003)
NGC 6633	8.08	0.02	+0.06	0.01	3	Santos et al. (2009)[a]
NGC 6705	6.78	0.21	+0.23	0.01	3	Santos et al. (2012)[a]
NGC 6819	8.07	0.00	+0.09	0.03	3	Bragaglia et al. (2001)
NGC 7789	9.55	0.12	+0.02	0.04	28	Jacobson et al. (2011b)

Notes. Cluster Galactocentric radius, R, is calculated using the solar distance $d_\odot$ (Table 6.1), the solar Galactocentric radius of $R_\odot = 8.4\,\mathrm{kpc}$ (Sect. 4.1.1), and cluster coordinates taken from the catalog of Dias et al. (2002a, V3.2). The error of cluster Galactocentric radius, σ_R, is the standard deviation of a set of 1000 realizations of R derived from randomly generated values of $d_\odot$ having a normal distribution with its standard deviation equal the $\sigma_{d_\odot}$ (Table 6.1). Metallicity, [Fe/H], and its error, $\sigma_{[Fe/H]}$, are given in the 3rd and the 4th column, respectively. Number of stars used to obtain clusters metallicity is given in the 5th column. An finally, the 6th column lists the reference for metallicity. [(a)] Santos et al. (2009, 2012) give clusters metallicity values derived using different line-lists. We adopt the [Fe/H] values derived using the line-list of Sousa et al. (2008) with a corrected scale (see Santos et al., 2009, Sect. 4.2 for details about the correction).

in its instrumental system (close to the R band) and the distribution of PM errors (per coordinate) peaks around $4\,\mathrm{mas\,yr^{-1}}$.

For most of the sample clusters, a membership study based on the RV measurements is available in the literature. In these cases, we carried out a cross-identification of member stars with the UCAC4 catalog. The cross-identification was made through the equatorial coordinates using the software TOPCAT.[4] Further, to avoid stars with non-standard PM errors, only these that have the PM error smaller than $5\,\mathrm{mas\,yr^{-1}}$ were used (PM error is calculated as $\sigma_\mu = \sqrt{\sigma_{\mu_\alpha}{}^2 + \sigma_{\mu_\delta}{}^2}$, where σ_{μ_α} and σ_{μ_δ} are errors of the μ_α and μ_δ PM vector components, respectively). If there were at least 10 such member stars identified, we calculated the mean value of each PM component. To avoid using possible outliers, we applied the 3σ cut-off and excluded stars with either of their PM component outside the 3σ intervals. An updated mean PM vector was calculated for the new sample and the 3σ cut-off was applied again. This procedure was applied until no outlier was identified in the sample. The final mean values of each PM component were used as the components of the mean cluster PM vector. Detailed description of the process for individual clusters including references to the original RV-membership studies and the number of used stars is given in Sect. 6.4.

For some clusters in our sample there is not a sufficient number of RV-member stars or the sample of cross-identified stars is too small (less then 10 members with their PM error smaller than $5\,\mathrm{mas\,yr^{-1}}$). In these cases, to obtain the mean cluster PM vector, we applied a cluster–field separation method that is discussed in the following section and in Appendix B. The cluster–field separation method was tested for all clusters in the sample and comments about these results are given in Sect. 6.4. Generally, the results are consistent with values obtained using the cross-identification.

6.3.1 Cluster–field separation based on PMs

The PM data of individual stars are very often used to separate the cluster members from the field stars, i.e., to determine stars cluster membership probability. The membership determination problem, or in other words the cluster–field separation, can be in general solved in various observational data planes and their combination. Because of their common origin and characteristics, the cluster member stars form over-densities in the PM space, in the spatial distribution (coordinates, radii), in the radial velocity dimension, and they also have a specific distribution in the photometric plane (CMDs of clusters). In the ideal case, all the available observational information is combined to estimate the cluster membership probability of individual stars. On the other hand, the data from different observational planes are often not available for the same sample of stars or they have different accuracies. The topic of cluster–field separation using the PM data is widely discussed in the literature (see for example, the references given later in this section and in Appendix B). Basically, two main methods have been used and in the paragraphs below we give their brief summary. A detailed description of the method implemented here is given in Appendix B.

[4] `http://www.star.bristol.ac.uk/~mbt/topcat/`

Parametric method

The *classical* method, originally described by Vasilevskis et al. (1958), is based on the assumption of parametric models for the cluster and the field stars distributions in the 2-dimensional PM space. It assumes that the two groups can be described by normal bivariate functions. The cluster stars distribution function is circular (supposing that the intrinsic velocity dispersion is not resolved and there is no systematic difference in observational errors, which are assumed to be independent on direction), and the field stars distribution is elliptical. The maximum likelihood method is usually used for the determination of distributions parameters (Sanders, 1971). Later, the classical method was improved to weight the stellar PMs with different observational uncertainties by Stetson (1980) and Zhao & He (1990). Various modifications of the parametric method were used for the analysis of mean PM of OCs (e.g., Dias et al., 2002a, 2006; Krone-Martins et al., 2010).

The parametric method generally works well provided the assumption of the bivariate cluster and field stars distributions is fulfilled, the ratio of numbers of cluster/field stars is high, and the statistical distance between the cluster and the field distribution is large enough (see, e.g., a discussion in Galadí-Enríquez et al., 1998). However, there are various reasons why it can fail in other cases – the distributions can be far away from the assumed model functions (especially for the field distribution, the model can be quite unrealistic, since asymmetries or tails can be present), both distributions can be very close to each other, there are overlapping distributions of two clusters present in the data, or a large number of field stars is present in the sample. The method is also very sensitive to data pruning and the rejection of sample outliers (Cabrera-Cano & Alfaro, 1990).

Non-parametric method

Basic idea of the non-parametric method for the cluster–field separation in the 2-dimensional PM space, is the empirical determination of the cluster and field stars distributions without any assumption about their shape. Cabrera-Cano & Alfaro (1990) used the kernel estimation technique (with a circular Gaussian kernel function) to derive the data distributions. Different implementations of this approach were further described by Chen et al. (1998) or Galadí-Enríquez et al. (1998). In the data sample, the total distribution is given as sum of the cluster and the field stars distributions. To obtain the frequency function for the cluster stars (and so the cluster membership probabilities), it is necessary to decompose the total combined cluster+field distribution into the cluster and the field parts by subtracting the field contribution. The field frequency function can be estimated, e.g., using a model of the Galaxy stellar population in the direction of the studied cluster (Chen et al., 1998); by a geometrical division of the sample – stars from a circle within the cluster radius and from a corona limited by some higher radii centered on the cluster are taken to estimate the cluster+field sample and the field distribution, respectively (Galadí-Enríquez et al., 1998); or using a membership classification based on some other independent observational information, e.g., Frinchaboy & Majewski (2008) used the RV-membership to identified the field stars. Non-parametric approach was used by several authors, for example, by Frinchaboy & Majewski (2008) or Balaguer-Núñez

Table 6.3: Parameters of OCs for the cluster-field separation.

Cluster	α (J2000) [h m s]	δ (J2000) [° ′ ″]	r_c [′]	Notes
Melotte 66	7 26 23	−47 40 0	10.0	
NGC 1545	4 20 57	50 15 12	10.0	
NGC 2660	8 42 38	−47 12 0	10.0	
NGC 3680	11 25 38	−43 14 36	10.0	$J < 14$ mag
NGC 6192	16 40 23	−43 22 0	10.2	
NGC 6705	18 51 5	−6 16 12	21.0	

et al. (2004b, 2005), who also give a comparison between classical parametric and non-parametric methods.

Our implementation

In cases of clusters with less than 10 RV-based member stars cross-identified with the UCAC4 catalog that have the PM error smaller than 5 mas yr^{-1}, we applied the non-parametric cluster–field separation method using the kernel estimation of the cluster and field frequency functions adopted from Galadí-Enríquez et al. (1998). There were six such clusters and they are listed in Table 6.3 together with their central coordinates, cluster radii, and additionally notes relevant to the cluster–field separation process (see respective paragraphs in Sect. 6.4).

A detailed description of the procedure and an example of its usage (cluster NGC 2660) are given in Appendix B. Briefly, we applied the kernel estimation of the empirical frequency functions of the mixed cluster+field populations within the cluster geometrical radius and of the field stars in a corona surrounding the cluster field (with the inner radius equal the cluster radius, and the outer equal twice its value). To consider the observational errors of PM components, we applied the procedure on 10 random realizations of the data and derived corresponding uncertainties of the final mean cluster PM vector.

6.4 Notes on PMs of individual OCs

In this section, various notes on obtaining the mean cluster PM vectors are given for each cluster in the sample. The final values of the mean PM vectors together with the results collected from the literature are given in Table C.1.

Blanco 1

The cross-identification of 79 RV-member stars from Mermilliod et al. (2009) with the UCAC4 catalog gives 78 stars with their PM error smaller than 5 mas yr^{-1}; their mean PM vector is $(-18.9, 3.2) \pm (0.2, 0.2)$ mas yr^{-1}, which we take as the cluster mean PM. This result roughly agrees with the values published in literature, see Table C.1.

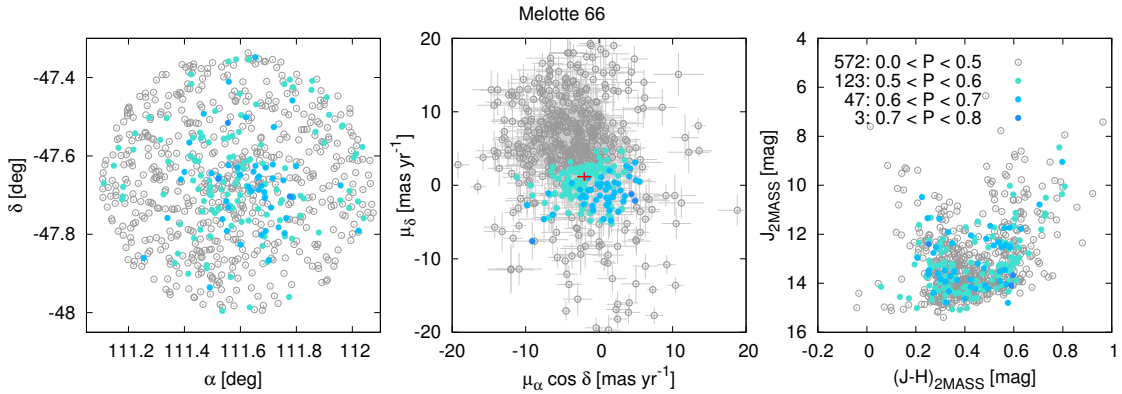

Figure 6.2: Cluster–field membership analysis for Melotte 66. *Left:* α and δ J2000 equatorial coordinates of the cluster field; *Middle:* VPD of the cluster field; *Right:* 2MASS CMD of the cluster field. Coordinates and PMs are taken from the UCAC4 catalog. Cluster field is defined by the parameters listed in Table 6.3. The cluster–field separation method is described in Appendix B. Different colors of the individual stars correspond to different cluster membership probability bins: gray circles represent stars with the membership probability less than 50%; light to dark blue circles represent probability of 50%–100%, with an increment of 10%. Colors and corresponding probabilities are indicated in the left plot (with the CMD), where the number of stars in each bin is also given. The red cross in the middle plot (with the VPD) indicates the final mean PM of the cluster (see Appendix B for more detailed discussion).

IC 2602

Based on RVs, Mermilliod et al. (2009) found 26 member dwarf stars in the cluster; from these, 25 stars were cross-identified with the UCAC4 catalog, 22 having their PM error smaller than $5\,\mathrm{mas\,yr^{-1}}$. Additionally, 2 of these stars were excluded from the sample – though they are just within the 3σ mean PM intervals, the amplitude of their PM is higher then $64\,\mathrm{mas\,yr^{-1}}$ and they clearly lie outside the distribution of the rest of the cluster members sample. The final sample of 20 stars has the mean PM vector of $(-14.9, 7.9) \pm (1.6, 1.3)\,\mathrm{mas\,yr^{-1}}$. We note that both components of the result have somehow smaller absolute values than values presented in the literature (Table C.1).

IC 4651

The cross-identification of 19 RV-member stars from Mermilliod et al. (2008a) and the UCAC4 catalog gives 16 stars with their PM error smaller than $5\,\mathrm{mas\,yr^{-1}}$. The mean PM vector of these stars is $(-1.2, -2.5) \pm (0.6, 1.0)\,\mathrm{mas\,yr^{-1}}$, which within the errors compares well with the results of Dias et al. (2006), Kharchenko et al. (2005a), or Frinchaboy & Majewski (2008), see Table C.1.

Melotte 66

The cross-identification of 5 RV-member stars from Sestito et al. (2008, based on RVs derived from a high-resolution spectroscopy) with the UCAC4 catalog gives mean cluster PM of $(-2.8, 2.8) \pm (0.6, 1.0)\,\mathrm{mas\,yr^{-1}}$. Although this result is based on PMs of only 5 stars, it agrees (within the errors) with the result of the cluster–field separation routine that gives $(-2.0, 1.2) \pm (1.0, 0.6)\,\mathrm{mas\,yr^{-1}}$, which we further consider as the cluster mean PM vector. See Table 6.3 for parameters of the cluster–field separation method and Fig. 6.2 for the resulting plots of the stars equatorial coordinates (distribution in the 2-dimensional sky plane), their vector point diagram (VPD, distribution in the 2-dimensional PM plane), and their CMD.

Melotte 71

The cross-identification of 17 RV-member stars from Mermilliod et al. (2008a) with the UCAC4 catalog gives 10 stars with the PM error smaller than $5\,\mathrm{mas\,yr^{-1}}$. Their mean PM value, $(-4.7, 7.5) \pm (0.6, 0.6)\,\mathrm{mas\,yr^{-1}}$, is taken as the mean cluster PM (we obtained a similar result using the cluster–field separation analysis), a result with absolute values of both components slightly higher then found by other authors (Table C.1), whose results, however, are not consistent with each other either.

NGC 188

The cross-identification of 47 RV-member stars from Jacobson et al. (2011a, based on RVs derived from a high-resolution spectroscopy) with the UCAC4 catalog leads to 36 stars with PM error smaller than $5\,\mathrm{mas\,yr^{-1}}$. The mean PM vector of these stars is taken as the mean cluster PM: $(-2.9, -1.4) \pm (0.6, 0.5)\,\mathrm{mas\,yr^{-1}}$.

NGC 752

The cross-identification of 76 RV-member stars from Mermilliod et al. (2009) and the UCAC4 catalog leads to 75 stars with their PM error smaller than $5\,\mathrm{mas\,yr^{-1}}$. The mean PM vector of these stars is $(7.7, -11.9) \pm (0.1, 0.1)\,\mathrm{mas\,yr^{-1}}$ (we tested the cluster–field separation method and using the cluster radius of $87'$ from Kharchenko et al., 2005a, we obtained a consistent result). This result is consistent with values published in other studies (Table C.1).

NGC 1039 (M 34)

Meibom et al. (2011) combined photometry and RV measurements to obtain the cluster membership probability for 120 stars in the cluster field; they found 83 of these stars to br kinematic and photometric members. The cross-identification of this sample with the UCAC4 catalog gives 37 stars with their PM error smaller than $5\,\mathrm{mas\,yr^{-1}}$. Their mean PM vector is $(0.2, -6.3) \pm (0.4, 0.3)\,\mathrm{mas\,yr^{-1}}$ (we tested also the cluster–field separation method with the cluster radius of $22.2'$ from Kharchenko et al., 2005a, which leads to consistent result). This result is roughly consistent with the PM vectors published in the

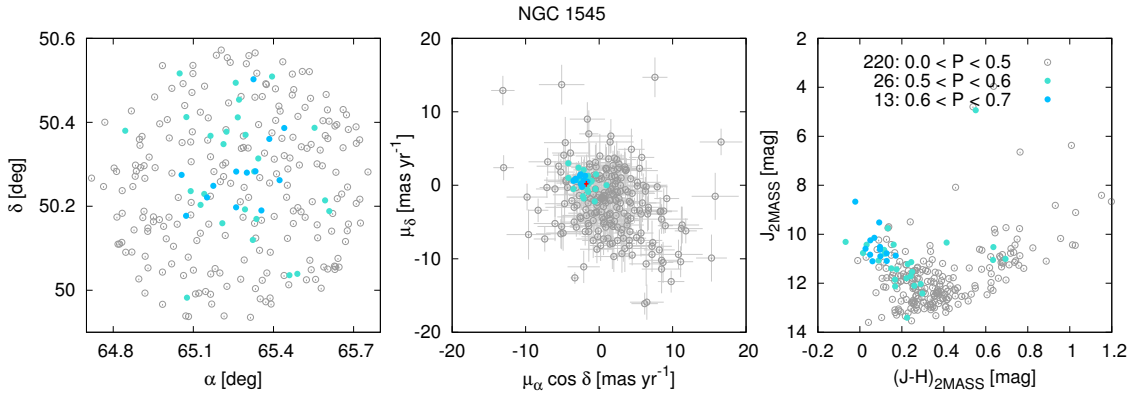

Figure 6.3: Cluster–field membership analysis for NGC 1545. See Fig. 6.2 for the description.

literature (Table C.1, note that these do not agree with each other, within their errors, which are quite small, about 0.2 mas yr^{-1}, in most of the published cases).

NGC 1545

There are only few (up to 3) RV-member stars determined in the literature (Mermilliod et al., 2008a; Začs et al., 2011). The cluster–field separation method gives stable results for the cluster radii within an interval of published values, from 9.0′ (Dias et al., 2002a, V3.2) to 12.6′ (Kharchenko et al., 2005a). We chose the radius of 10.0′. The mean PM vector is $(-1.7, 0.2) \pm (0.3, 0.4)$ mas yr^{-1} (Fig 6.3), which falls within the range of estimates presented in the literature (see Table C.1).

NGC 1817

The cross-identification of 38 RV-member stars from Mermilliod et al. (2008a) and the UCAC4 cataloque gives 31 stars with their PM error smaller than 5 mas yr^{-1} (RV membership analysis by Jacobson et al., 2011a would give only one extra star within this constrain). The mean PM vector of these stars is $(-2.2, -0.7) \pm (0.5, 0.4)$ mas yr^{-1}.

NGC 2099 (M 37)

The cross-identification of 35 RV-member stars from Mermilliod et al. (2008a) with the UCAC4 catalog gives 28 stars with their PM error smaller than 5 mas yr^{-1}. Their mean PM vector is $(2.5, -7.0) \pm (0.3, 0.3)$ mas yr^{-1} (the cluster–field separation method was tested and gives a consistent result), in a good agreement with Dias et al. (2006, see Table C.1), who used the UCAC2 catalog. Studies using the Tycho-2 catalog (e.g., Loktin & Beshenov, 2003; Kharchenko et al., 2005a; Frinchaboy & Majewski, 2008) found slightly higher value of the $\mu_\alpha \cos\delta$ component; however, the difference is small (less than

$1\,\mathrm{mas\,yr^{-1}}$, when considering the errors). The μ_δ component agrees across the results from different PM catalogs.

NGC 2204

The cross-identification of RV-member stars from Jacobson et al. (2011a) and Mermilliod et al. (2008a) with the UCAC4 (18 stars with their PM error smaller than $5\,\mathrm{mas\,yr^{-1}}$) gives the mean PM vector of $(1.0, 1.5) \pm (0.7, 0.6)\,\mathrm{mas\,yr^{-1}}$, which within the errors fairly compares with $(-0.22, 1.78) \pm (0.48, 0.44)\,\mathrm{mas\,yr^{-1}}$ found by Loktin & Beshenov (2003).

NGC 2243

The cross-identification of RV-member stars from Jacobson et al. (2011a) with the UCAC4 catalog gives 14 stars with their PM error smaller than $5\,\mathrm{mas\,yr^{-1}}$; their mean PM vector is $(1.0, 5.3) \pm (1.1, 1.3)\,\mathrm{mas\,yr^{-1}}$. This result does not agree well with that of $(2.53, 2.9) \pm (0.54, 1.30)\,\mathrm{mas\,yr^{-1}}$ found by Loktin & Beshenov (2003, who, however, classified this mean PM as a *very unreliable data*), either with that of $(-3.66, 3.32) \pm (0.61, 0.61)\,\mathrm{mas\,yr^{-1}}$ found by Dias et al. (2006). Note, however, that these two results do not agree well with each other.

NGC 2355

Soubiran et al. (2000) combined spectroscopic and astrometric data of stars in the field of NGC 2355 and based on their RVs and PMs they classified 17 stars as cluster members. We compared their sample with the RV-members of Mermilliod et al. (2008a) and rejected membership of one star, so all the members found by Soubiran et al. (2000) are also members by Mermilliod et al. (2008a). We cross-identified this sample with the UCAC4 catalog and identified 12 stars with their PM error smaller than $5\,\mathrm{mas\,yr^{-1}}$. Their mean PM vector is $(-2.5, -3.2) \pm (0.5, 0.8)\,\mathrm{mas\,yr^{-1}}$, which is in a good agreement with Soubiran et al. (2000), see Table C.1. To check the PM obtained by the cross-identification we carried out our cluster–field separation analysis. Soubiran et al. (2000) estimated the radii of the cluster *central body* and *halo* to be $7'$ and $15'$, respectively (much larger than $3.5'$, the radius given in the catalog of Dias et al., 2002a, V3.2). Our cluster–field separation method gives stable results for the cluster radii of 10–$15'$ (radius of $12'$ was used) and the resulting mean cluster PM of $(-2.9, -3.3) \pm (0.7, 1.1)\,\mathrm{mas\,yr^{-1}}$ agrees well with that obtained by the cross-identification.

NGC 2360

The cross-identification of 20 RV-member stars from Mermilliod et al. (2008a) with the UCAC4 catalog gives 16 stars with their PM error smaller than $5\,\mathrm{mas\,yr^{-1}}$. The mean PM vector of these stars is $(-2.7, 6.0) \pm (0.5, 0.4)\,\mathrm{mas\,yr^{-1}}$. The cluster–field separation method gives stable results, which are consistent with this value, for a wide range of radii of about 6–$30'$. The cluster radius estimates published in the literature fall within a similar interval: $6.5'$ by Lyngå (1987); $15.3'$ by Nilakshi et al. (2002); $15.0'$ by Kharchenko et al.

(2005a, 2009); 22.63′ by Güneş et al. (2012). The level and distribution of the membership probability from our cluster–field separation favors somehow higher values of the cluster radius, around 20′ (for smaller radii, almost all stars within the field have membership probability higher than 50%; for bigger radii, the number of stars with membership probability higher than 50% decreases).

NGC 2420

The cross-identification of 22 RV-member stars from Mermilliod et al. (2008a) with the UCAC4 catalog gives 11 stars with PM error less than $5\,\mathrm{mas\,yr^{-1}}$; their mean PM vector is $(-0.7, -2.8) \pm (0.9, 0.5)\,\mathrm{mas\,yr^{-1}}$ (additionally, Jacobson et al., 2011b determined membership for 22 stars, 12 of them being classified as members, of which 2 were not studied by Mermilliod et al. (2008a); both of these stars, however, were not cross-identified with the UCAC4 catalog). We tested the cluster–field separation method for various cluster radii. The catalog of Dias et al. (2002a, version 3.2) gives the cluster radius of 2.5′; however, few recent studies of the cluster, Nilakshi et al. (2002, using the photometric data of the SDSS), Chen et al. (2004, using the 2MASS star catalog), Sharma et al. (2006, using CCD observations), estimated that cluster radius is about 10–13′. The cluster–field separation method gives stable results for radii within the range of 8–15′. Using the cluster radius of 11.6′ (Chen et al., 2004), which gives the mean cluster PM vector of $(-1.4, -1.8) \pm (0.8, 0.7)\,\mathrm{mas\,yr^{-1}}$, within the errors in agreement with the cross-identification. We use the the cross-identification result as the final mean cluster PM vector; this result is consistent with values found by Loktin & Beshenov (2003), which is, to our knowledge, the only mean PM estimate mentioned in the literature.

NGC 2447 (M 93)

All 13 RV-member stars from Mermilliod et al. (2008a) that were cross-identified with the UCAC4 catalog have their PM error smaller than $5\,\mathrm{mas\,yr^{-1}}$. The mean PM vector of these stars is $(-4.9, 4.0) \pm (0.6, 0.3)\,\mathrm{mas\,yr^{-1}}$; a result consistent with most of other estimates published in the literature (see Table C.1).

NGC 2477

The cross-identification of 76 RV-member stars from Mermilliod et al. (2008a) with the UCAC4 catalog gives 75 stars with their PM error smaller than $5\,\mathrm{mas\,yr^{-1}}$. The mean PM vector of these stars is $(-0.65, 1.13) \pm (0.60, 0.59)\,\mathrm{mas\,yr^{-1}}$. This result falls within the intervals defined by values found by other authors (Table C.1).

NGC 2539

The cross-identification of 11 RV-member stars of Mermilliod et al. (2008a) with the UCAC4 catalog gives 10 stars with their PM error less than $5\,\mathrm{mas\,yr^{-1}}$. The mean PM vector of these stars is $(-4.13, -1.7) \pm (1.4, 0.6)\,\mathrm{mas\,yr^{-1}}$, which is in a good agreement with the majority of results published in other studies (see Table C.1). Various authors

give different values of cluster radius, from 4.5′ (Dias et al., 2002a, V3.2) to 30′ Kharchenko et al. (2005b). The cluster–field separation method was tested for this range of cluster radii and gives results consistent with the cross-identification.

NGC 2632 (Praesepe)

NGC 2632 (Praesepe) is close ($d_\odot = 180 \pm 10$ kpc, Table 6.1), well studied OC. Various studies of its mean PM vector are generally consistent (Table C.1) and, not surprisingly, our results based on the UCAC4 catalog agree well with these numbers published in the literature. The cross-identification of 150 RV-members from Mermilliod et al. (2009) with the UCAC4 catalog gives 141 stars with their PM error less than 5 mas yr^{-1}. Their mean PM vector is $(-35.3, -12.4) \pm (0.3, 0.2)$ mas yr^{-1}, comparing fairly well with the results found in other studies (Table C.1). Cluster–field separation analysis (using cluster radius of 3° from Kharchenko et al., 2005a) gives a similar mean PM vector.

NGC 2660

Sestito et al. (2006) used a high-resolution spectroscopic RV measurements of 6 members of NGC 2660; additionally to these stars, Mermilliod et al. (2008a) presented spectroscopy measurements of 9 different stars in the field of NGC 2660 and based on their RVs, they classified 6 of them as cluster members. 11 of the Sestito et al. (2006) and Mermilliod et al. (2008a) member stars have their PMs in the UCAC4 catalog with error smaller than 5 mas yr^{-1}. However, the PM of individual stars are quite dispersed (having the standard deviations of 21 and 37 mas yr^{-1} for the $\mu_\alpha \cos\delta$ and μ_δ components, respectively). Cluster radius given in the catalog of Dias et al. (2002a, V3.2) is 1.5′, compared with the half-radius of 4.8′ given by Portegies Zwart et al. (2001, see also references therein), who also estimated the tidal radius of the cluster to be 11.4′. We tested the cluster–field separation method with various cluster radii in the range of 2–15′. We chose the radius of 10′ giving the mean PM of $(-3.3, 6.9) \pm (1.4, 1.4)$ mas yr^{-1} (Fig. 6.4). The μ_δ component agrees well with the result by Loktin & Beshenov (2003), who obtained the mean cluster PM vector of $(-5.82, 7.4) \pm (0.81, 0.83)$ mas yr^{-1}; however, our value of the $\mu_\alpha \cos\delta$ component is somewhat higher.

NGC 2682 (M 67)

NGC 2682 (M 67) belongs to the one of the most studied Galactic OCs. The mean PM of the cluster has been calculated several times; using the HIPPARCOS catalog (Baumgardt et al., 2000), or the Tycho-2 catalog (Dias et al., 2001; Loktin & Beshenov, 2003; Kharchenko et al., 2005a; Frinchaboy & Majewski, 2008, see Table C.1 for comparison of their results). More recently, Bellini et al. (2010a) obtained an absolute PM using a ground-based multi-epoch CCD wide-field images observed with a 10 years epoch difference. The components of the cluster PM vector from various studies have values within intervals from -9.6 to -6.5 mas yr^{-1} and from -7.7 to -3.7 mas yr^{-1} for the $\mu_\alpha \cos\delta$ and μ_δ component, respectively (Table C.1). The cross-identification of 23 RV-members from Mermilliod et al. (2008a) and 40 additional RV-members from Mermilliod et al.

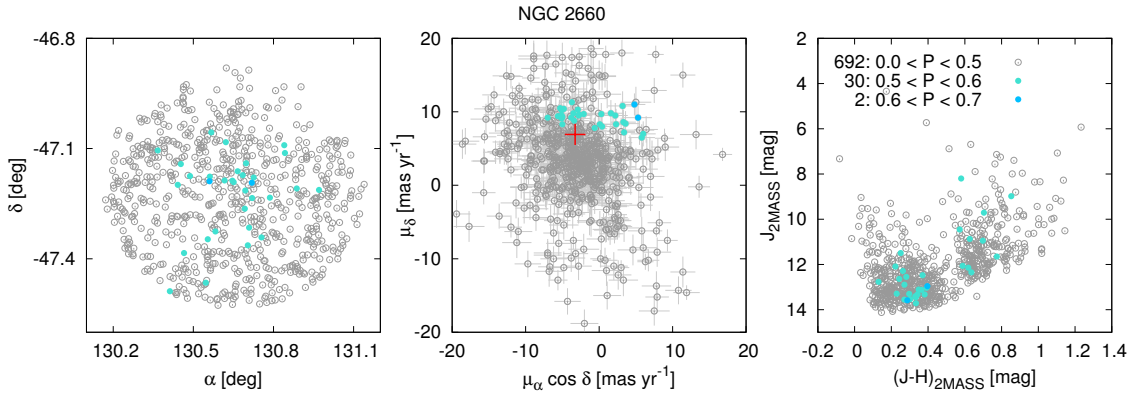

Figure 6.4: Cluster–field membership analysis for NGC 2660. See Fig. 6.2 for the description.

(2009) with the UCAC4 catalog gives 54 stars with their PM error less than 5 mas yr^{-1}. The mean PM vector of these stars is $(-9.1, -4.3) \pm (0.3, 0.2)$ mas yr^{-1} (consistent result was obtained using the cluster–field separation method), which falls within the intervals of previously measured values. This result is also consistent with the values of Bellini et al. (2010a), which we consider the most reliable from the available cluster mean PM estimates.

NGC 3114

RV membership studies of the cluster were done by González & Lapasset (2001) and Mermilliod et al. (2008a). González & Lapasset (2001) identified 19 cluster members; Mermilliod et al. (2008a) studied a sample of 11 stars and confirmed the results of González & Lapasset (2001) for all of them. We cross-identified the 19 member stars with the UCAC4 catalog and found 18 stars with PM error less than 5 mas yr^{-1}. Mean PM vector of this sample is $(-5.9, -4.2) \pm (0.4, 0.3)$ mas yr^{-1} (consistent result was obtained using the cluster–field separation method). When comparing this result with these published in the literature (Table C.1), we see that the $\mu_\alpha \cos\delta$ component has systematically of about 1.5 mas yr^{-1} lower value than the one found by Baumgardt et al. (2000), Dias et al. (2001), Loktin & Beshenov (2003), and Kharchenko et al. (2005a), who obtained the clusters mean PM vector using the HIPPARCOS or Tycho-2 catalog; on the other hand, our result agrees well with the value found by Dias et al. (2006), who used the UCAC2 catalog. Therefore, we account the discrepancy in the $\mu_\alpha \cos\delta$ component for the differences in the individual PMs presented in different catalogs. The μ_δ component estimates have consistent values across different catalogs and studies.

NGC 3680

Published estimates of the cluster mean PM agrees well (with a single exception of the result found by Baumgardt et al., 2000), finding the $\mu_\alpha \cos\delta$ and μ_δ components in the

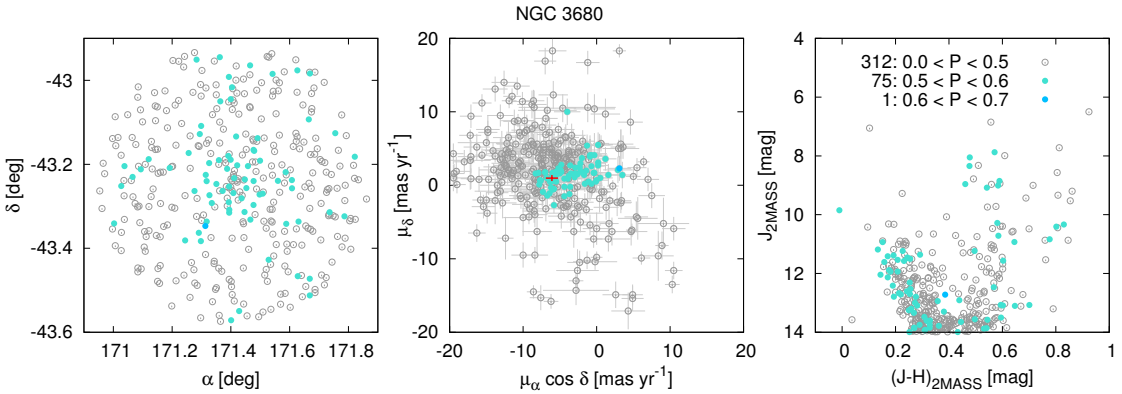

Figure 6.5: Cluster–field membership analysis for NGC 3680. See Fig. 6.2 for the description.

ranges from −6.4 to −5.4 and from 0.9 to 2.0, respectively (Table C.1). Our cluster–field separation method is not giving a stable results, even if a range of cluster radii was tested. This might be caused by a high ratio of the field stars to the cluster stars. Therefore, we applied a brightness cut-off and used only stars brighter than 14 mag in the 2MASS J band. With this constrain, our cluster–field separation method gives stable results, for different values of the cluster radius (range of 4–15′). We decided to use the cluster radius of 10′, a value which is between the cluster radius estimates of 2.5′ by Dias et al. (2002a, V3.2) and of 12.6′ by Kharchenko et al. (2005a). The final mean PM vector is $(-6.1, 1.0) \pm (0.8, 0.4)\,\mathrm{mas\,yr^{-1}}$ (Fig. 6.5), which falls within the intervals of the values presented in the literature.

NGC 3960

Mermilliod et al. (2008a) presented spectroscopy measurements for 14 stars in the field of NGC 3960; based on their RVs, they classified 12 stars as cluster members. 6 of these stars were already classified as members by Sestito et al. (2006) through a high-resolution spectroscopic RV measurements (they observed one additional star, which was classified as a non-member). We cross-identified 11 member stars with the UCAC4 catalog and obtain the mean PM of $(-8.9, 5.2) \pm (1.4, 1.3)\,\mathrm{mas\,yr^{-1}}$; this result is consistent with the one found by (Dias et al., 2006), however, the μ_δ component has a higher value than found by Loktin & Beshenov (2003) (Table C.1).

NGC 5822

The cross-identification of 21 RV-member stars of Mermilliod et al. (2008a) with the UCAC4 catalog give 20 stars with their PM error less than $5\,\mathrm{mas\,yr^{-1}}$. Their mean PM vector is $(-8.2, -6.1) \pm (0.7, 0.5)\,\mathrm{mas\,yr^{-1}}$ (confirmed by the cluster–field separation method). Different studies found slightly different mean PM vectors (Table C.1), however, almost all within the intervals from −8.6 to −6.2 and from −8.8 to $-5.7\,\mathrm{mas\,yr^{-1}}$ for the

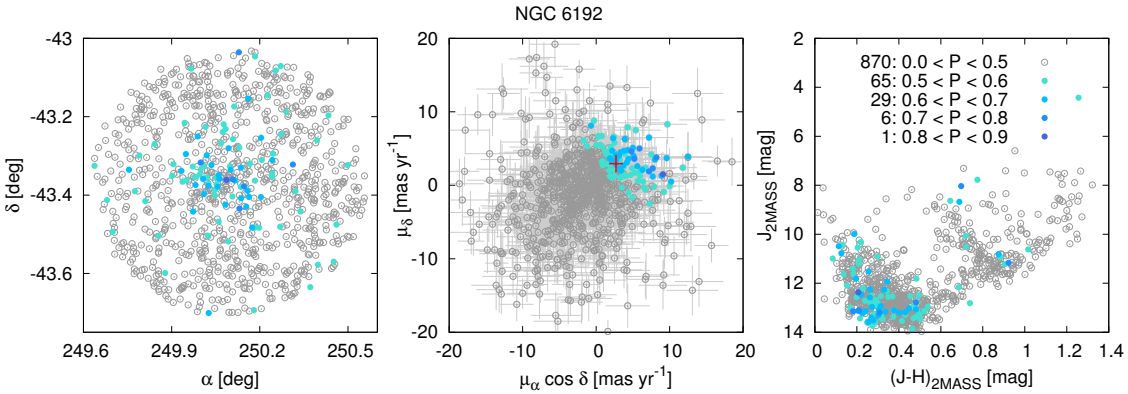

Figure 6.6: Cluster–field membership analysis for NGC 6192. See Fig. 6.2 for the description.

μ_δ and $\mu_\alpha \cos\delta$ components, respectively (excluding the result of Baumgardt et al., 2000, which is based on only 2 stars and is an outlier with respect to the results of other authors). The above mentioned PM vector resulting from the cross-identification falls within these intervals.

NGC 6134

The cross-identification of 19 RV-member stars determined by Mermilliod et al. (2008a) and the UCAC4 catalog gives 17 stars with their PM error less than $5\,\mathrm{mas\,yr^{-1}}$. Their mean PM vector is $(-0.7, -5.9) \pm (0.6, 0.5)\,\mathrm{mas\,yr^{-1}}$, which, within the errors, agrees well with previously published numbers (Table C.1). Using the cluster radius of $7.8'$ from Kharchenko et al., 2005a, our cluster–field separation method gives similar result.

NGC 6192

Cluster membership based on RVs was published only for 11 stars, with 5 of those were classified as cluster members (Mermilliod et al., 2008a; Magrini et al., 2010). The cross-identification with the UCAC4 catalog gives only 2 stars with their PM error less than $5\,\mathrm{mas\,yr^{-1}}$. Using the cluster radius of $10.2'$ from Kharchenko et al., 2005a, our cluster–field separation method gives a stable result and we found the mean cluster PM vector of $(2.7, 2.9) \pm (0.9, 1.2)\,\mathrm{mas\,yr^{-1}}$ (Fig. 6.6), which, within the errors, agrees well with some of the PM estimates published in the literature (Dias et al., 2002a, V3.2; Magrini et al., 2010) but disagrees with some others (Loktin & Beshenov, 2003; Kharchenko et al., 2005a; Dias et al., 2006), see Table C.1.

NGC 6253

Montalto et al. (2009) derived relative PMs of about 3000 stars in the field of NGC 6253. Based on this data they obtained stars membership probabilities. Anthony-Twarog

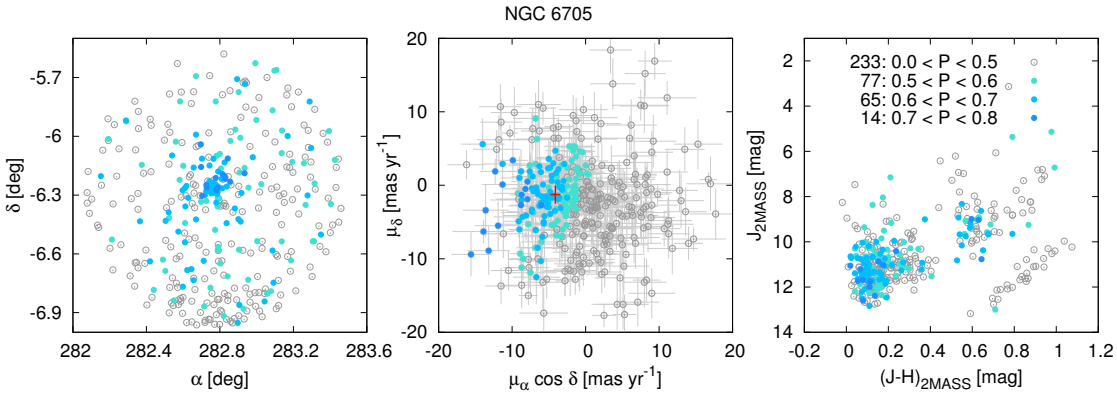

Figure 6.7: Cluster–field membership analysis for NGC 6705. See Fig. 6.2 for the description.

et al. (2010) presented RV-membership analysis based on a high-dispersion spectral data (using HYDRA multi-object spectrograph). They used their RV-membership probabilities and the PMs based on Montalto et al. (2009) to obtain a combined membership classification for 89 stars. We used this membership classification of individual stars in combination with the PM data from the UCAC4 catalog – 39 stars with their PM error smaller than 5 mas yr^{-1} were cross-identified. Their mean PM vector is $(-1.7, -3.5) \pm (1.2, 1.9)$ mas yr^{-1}.

NGC 6475

The cross-identification of 67 RV-member stars from the study of Jacobson et al. (2011b) with the UCAC4 catalog gives 46 stars with their PM error less than 5 mas yr^{-1}; their mean PM vector is $(1.1, -3.7) \pm (0.4, 0.4)$ mas yr^{-1}. This result agrees well with the one found by Dias et al. (2001); on the other hand, it is slightly different than the one found in other studies (Baumgardt et al., 2000; Loktin & Beshenov, 2003; Kharchenko et al., 2005a, see Table C.1).

NGC 6633

The cross-identification of 30 RV-member stars from Jeffries et al. (2002) with the UCAC4 catalog gives 20 stars with their PM error less than 5 mas yr^{-1}; their mean PM vector is $(0.2, -1.0) \pm (0.4, 0.4)$ mas yr^{-1}, consistent with most of the results published in other studies (Table C.1).

NGC 6705 (M 11)

Membership estimates based on RVs were presented by Gonzalez & Wallerstein (2000) and Mermilliod et al. (2008a), together classifying 18 stars as cluster members; however, the cross-identification of these stars with the UCAC4 catalog gives only 6 stars with their

PM error smaller than 5 mas yr^{-1}. Various studies found different values for the cluster radius – 7.5′ by Lyngå (1987, also adopted in WEBDA); 11.4′ by Kharchenko et al. (2005a); 16′ listed in the catalog of Dias et al. (2002a, V3.2); $(21 \pm 1)'$ by Santos et al. (2005), based on an overall analysis of 2MASS data. We tested the cluster–field separation method for all mentioned values and decided to use the most up-to-date value of Santos et al. (2005), which gives the mean PM vector of $(-4.12, -1.26) \pm (0.7, 1.2)$ mas yr^{-1} (Fig. 6.7), within the errors in agreement with the results of Dias et al. (2002a) and Frinchaboy & Majewski (2008), but in disagreement with some other studies (see Table C.1).

NGC 6819

Hole et al. (2009) presented a RV survey of the cluster including 1207 stars with photometry collected from the literature (the V band magnitude in the range of 11–16.5 mag) and presented membership probabilities for the upper MS stars. We used these membership probabilities of individual stars (56 stars with the cluster membership probability higher than 80%) in combination with the PM data from the UCAC4 catalog to obtain the mean PM of the cluster. We considered only stars with their PM error smaller than 5 mas yr^{-1}. The mean PM vector is $(-5.8, -2.8) \pm (1.0, 1.1)$ mas yr^{-1} and agrees with Dias et al. (2006), who obtained $(-5.33, -2.76) \pm (0.5, 0.5)$ mas yr^{-1}.

NGC 7789

The cross-identification of 37 RV-member stars of Jacobson et al. (2011b) with the UCAC4 catalog gives 17 stars with their PM error less than 5 mas yr^{-1}; their mean PM vector is $(2.0, -2.7) \pm (0.6, 0.6)$ mas yr^{-1}. Our cluster–field separation method gives similar result (using the cluster radius of 16.2′ from Kharchenko et al., 2005a) of $(1.7, -2.4) \pm (0.3, 0.6)$ mas yr^{-1}. These results, however, do not agree well with the values given either by Loktin & Beshenov (2003) or Kharchenko et al. (2005a). On the other hand, these do not agree in the $\mu_\alpha \cos\delta$ component between each other either (Table C.1).

6.4.1 Comparison with previous studies of clusters mean PM vectors

As mentioned in Sect. 2.3, there are several studies using different all-sky astrometric surveys and different cluster–field separation methods to obtain the mean PMs of OCs. PM vectors presented in these studies for individual clusters in our sample are listed in Table C.1 and, for some clusters, the differences are discussed in Sect. 6.4. Figure 6.8 shows a comparison of the mean PM vector components derived in this work and in four different studies that have, to our knowledge, the highest number of the common clusters with our sample: Dias et al. (2001, 2002a), Loktin & Beshenov (2003), Kharchenko et al. (2005a), and Dias et al. (2006). More quantitative comparison is given in Table 6.4. In general, the mean differences have values from 0.8 to 1.9 mas yr^{-1}, which is a fairly good agreement, as can been seen also in Fig. 6.8. Our PMs generally have higher errors with the mean value of 0.7 mas yr^{-1} (Table 6.4).

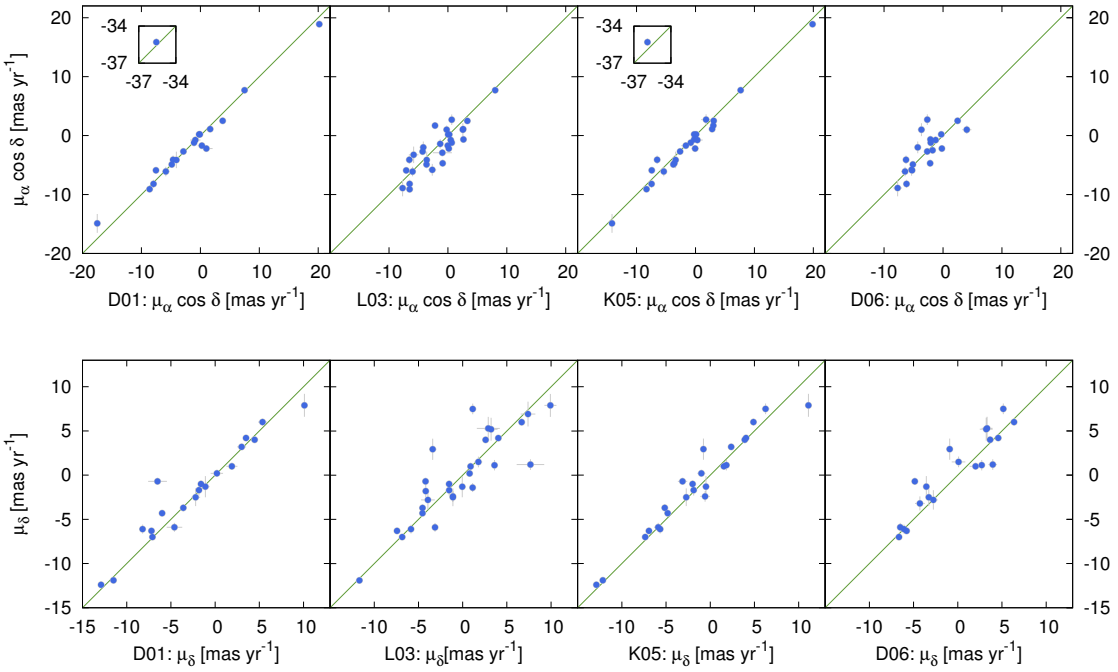

Figure 6.8: Comparison of the clusters PM components derived in this work and in several different studies. The results derived here are given on the vertical axis. The horizontal axis show results of: Dias et al. (2001, 2002a) – D01, Loktin & Beshenov (2003) – L03, Kharchenko et al. (2005a) – K05, and Dias et al. (2006) – D06. The upper panel compares the $\mu_\alpha \cos\delta$ component; the lower panel compares the μ_δ component. The green lines indicate the loci of equal PM components.

Table 6.4: Comparison of the PMs derived here and in previous studies.

Ref.	OCs	$\langle\sigma_{\mu_\alpha}\rangle$	$\langle\sigma_{\mu_\delta}\rangle$	$\langle\lvert\Delta\mu_\alpha \cos\delta\rvert\rangle$	$\langle\lvert\Delta\mu_\delta\rvert\rangle$
		[mas yr^{-1}]		[mas yr^{-1}]	
this study	34	0.7	0.7	–	–
D01	20	0.4	0.4	0.8	1.0
L03	30	0.4	0.4	1.9	1.7
K05	24	0.4	0.3	0.9	1.0
D06	20	0.4	0.4	1.6	1.4

Notes. The 2nd column indicates the number of common OCs in this and the referenced study; $\langle\sigma_{\mu_\alpha}\rangle$ and $\langle\sigma_{\mu_\delta}\rangle$ are the mean values of PM errors for the common clusters sample; $\langle\lvert\Delta\mu_\alpha \cos\delta\rvert\rangle$ and $\langle\lvert\Delta\mu_\delta\rvert\rangle$ are the mean absolute values of differences between PM components given here and in the referenced stufy for common clusters.

References. D01 – Dias et al. (2001, 2002a); L03 – Loktin & Beshenov (2003); K05 – Kharchenko et al. (2005a); D06 – Dias et al. (2006)

6.5 Current orbits

6.5.1 Orbital parameters

To characterize the current kinematics of our OCs sample, we investigate orbital parameters of clusters current orbits. Uncertainties of the input observational data, which were used to calculate the initial conditions, were taken into account in a Monte Carlo fashion, similarly as for NGC 6791 (Sect. 5.1.1). We randomly generated a set of 1000 values for cluster distance to the Sun $d_\odot$, radial velocity v_r, and components of the PM vector. For each of these quantities, the values have Gaussian distribution with the mean and the standard deviation equal the observed value and its uncertainty, respectively. For $d_\odot$ and v_r these are given in Table 6.1; components of the PM vector are given in Table C.1. For each this set of values of $d_\odot$, v_r, and PM components, the initial conditions were derived following the procedure of Johnson & Soderblom (1987, see also Sect. 5.1.1). A set of 1000 orbits was integrated forward for 2 Gyr using all four flavors of the present-day MW model (Sect. 4, the model MW1). Finally, orbits are characterized by orbital parameters of the first completed orbital cycle (defined by azimuthal change of 2π). Mean values and standard deviations of the orbital parameters are calculated for each set of orbits and each flavor of the MW model. Values for the axisymmetric and the combined bar and spiral arms model are listed in Table 6.5. Figure D.1 (Appendix D) shows orbits projections into the Galactic and meridional plane for the axisymmetric and the combined model for each cluster (orbits with initial conditions given by the mean values of input observational data are plotted).

All clusters in our sample are located at the Galactocentric radii within the interval of 6.5–12 kpc (Table 6.2). Therefore, the influence of the Galactic bar and the spiral arms is not expected to be prominent. Indeed, there is no significant difference in the shape of current orbits among various model flavors. The differences between values of orbital parameters derived using different flavors of the MW model are generally smaller or of the same order as their standard deviations given by the uncertainties of the input data. Figure 6.9 shows the comparison of parameters derived using the axisymmetric and the combined bar and spiral arms MW model. It can be seen that the model including the bar and spiral arms generally produces orbits with slightly higher eccentricities and vertical amplitudes (similarly as in the case of NGC 6791, Sect. 5.1.2). These trends can also be seen in Fig. D.1. All clusters have close-to-circular orbits, with eccentricity below 0.25.

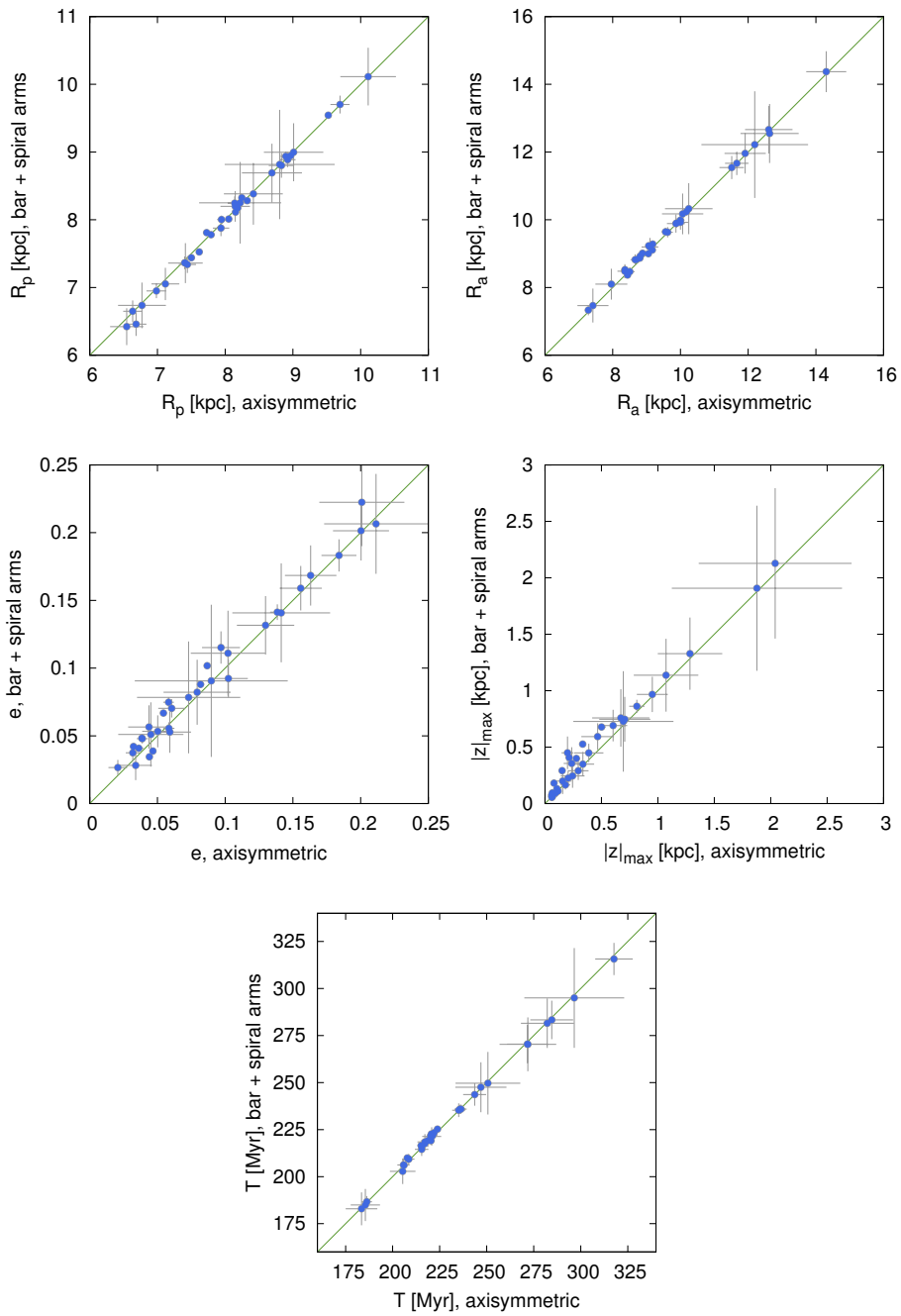

Figure 6.9: Comparison of the current orbital parameters derived using the axisymmetric and the bar and spiral arms combined MW model. Perigalacticon distance $R_{\rm p}$, apogalacticon distance $R_{\rm a}$, eccentricity e, vertical amplitude $|z|_{\rm max}$, and azimuthal period T are shown. Green lines indicate the loci of equal values.

Table 6.5: Orbital parameters for the axisymmetric and and combined MW model (including the bar and spiral arms).

Cluster		R_a [kpc]	σ_{R_a}	R_p [kpc]	σ_{R_p}	e	σ_e	$\lvert z\rvert_{max}$ [kpc]	$\sigma_{\lvert z\rvert_{max}}$	T [Myr]	σ_T
Blanco 1	a	8.33	0.02	8.88	0.01	0.032	0.001	0.21	0.01	221	1
	b	8.28	0.01	9.01	0.01	0.042	0.001	0.41	0.01	223	1
IC 2602	a	7.73	0.02	8.44	0.02	0.044	0.001	0.08	0.01	206	1
	b	7.81	0.02	8.37	0.02	0.035	0.001	0.18	0.03	206	1
IC 4651	a	7.40	0.06	8.36	0.22	0.061	0.010	0.20	0.03	206	3
	b	7.36	0.09	8.48	0.21	0.070	0.007	0.23	0.06	206	3
Melotte 66	a	8.22	0.61	12.63	0.86	0.211	0.038	1.88	0.75	251	17
	b	8.25	0.60	12.55	0.87	0.207	0.037	1.91	0.73	250	17
Melotte 71	a	9.52	0.03	14.31	0.59	0.200	0.021	0.34	0.10	318	10
	b	9.54	0.04	14.37	0.60	0.201	0.022	0.35	0.11	316	9
NGC 188	a	8.92	0.12	9.87	0.27	0.050	0.012	0.81	0.07	235	3
	b	8.89	0.11	9.89	0.27	0.053	0.012	0.86	0.06	235	4
NGC 752	a	8.15	0.05	8.81	0.02	0.039	0.004	0.28	0.02	220	2
	b	8.11	0.05	8.93	0.01	0.048	0.004	0.40	0.01	222	2
NGC 1039	a	8.25	0.03	9.05	0.03	0.047	0.001	0.15	0.01	217	1
	b	8.33	0.03	9.00	0.03	0.039	0.001	0.29	0.03	218	1
NGC 1545	a	8.90	0.08	10.00	0.12	0.058	0.004	0.06	0.02	236	3
	b	8.94	0.07	9.99	0.12	0.056	0.005	0.06	0.02	236	2
NGC 1817	a	9.01	0.44	11.91	0.61	0.139	0.005	0.71	0.23	282	14
	b	9.00	0.43	11.96	0.59	0.141	0.006	0.75	0.20	282	13
NGC 2099	a	7.12	0.21	9.89	0.12	0.163	0.019	0.09	0.02	220	2
	b	7.05	0.24	9.90	0.13	0.168	0.022	0.09	0.02	219	2
NGC 2204	a	8.80	0.81	11.66	0.35	0.141	0.036	1.28	0.29	272	15
	b	8.82	0.81	11.67	0.35	0.141	0.037	1.33	0.32	270	14
NGC 2243	a	10.11	0.41	12.19	1.58	0.090	0.057	2.04	0.68	297	27
	b	10.11	0.43	12.22	1.58	0.091	0.056	2.13	0.67	295	27
NGC 2355	a	8.69	0.44	10.18	0.12	0.079	0.025	0.60	0.13	244	6
	b	8.69	0.43	10.24	0.12	0.082	0.024	0.69	0.14	244	6
NGC 2360	a	9.70	0.14	12.61	0.70	0.130	0.021	0.24	0.11	285	11
	b	9.70	0.13	12.66	0.70	0.132	0.022	0.24	0.10	283	10
NGC 2420	a	8.42	0.44	11.51	0.36	0.156	0.016	0.95	0.14	272	11
	b	8.38	0.46	11.54	0.34	0.159	0.016	0.97	0.16	270	10
NGC 2447	a	8.97	0.02	9.56	0.11	0.032	0.005	0.07	0.04	236	3
	b	8.95	0.03	9.64	0.12	0.038	0.006	0.06	0.04	236	2
NGC 2477	a	8.14	0.10	10.00	0.23	0.102	0.014	0.18	0.04	221	2
	b	8.25	0.10	9.92	0.22	0.092	0.014	0.17	0.04	222	2
NGC 2539	a	8.15	0.22	9.17	0.10	0.059	0.016	0.29	0.09	219	4
	b	8.20	0.23	9.11	0.09	0.053	0.015	0.29	0.08	219	3
NGC 2632	a	7.62	0.02	9.06	0.02	0.087	0.003	0.10	0.01	222	2
	b	7.53	0.02	9.23	0.02	0.102	0.003	0.13	0.02	223	1
NGC 2660	a	8.83	0.19	10.25	0.70	0.073	0.038	0.69	0.44	247	14
	b	8.80	0.18	10.33	0.75	0.078	0.041	0.73	0.44	248	13
NGC 2682	a	7.79	0.03	9.18	0.04	0.082	0.003	0.50	0.04	224	2
	b	7.78	0.03	9.28	0.04	0.088	0.003	0.68	0.02	225	2

Continued on next page.

Table 6.5: Orbital parameters – continued from previous page.

Cluster		R_a [kpc]	σ_{R_a}	R_p [kpc]	σ_{R_p}	e	σ_e	$\lvert z\rvert_{max}$ [kpc]	$\sigma_{\lvert z\rvert_{max}}$	T [Myr]	σ_T
NGC 3114	[a]	8.19	0.02	8.80	0.04	0.036	0.004	0.12	0.02	215	2
	[b]	8.17	0.01	8.87	0.03	0.041	0.002	0.11	0.03	216	1
NGC 3680	[a]	7.95	0.07	8.50	0.14	0.034	0.012	0.33	0.02	208	1
	[b]	8.00	0.06	8.47	0.13	0.028	0.011	0.53	0.02	210	2
NGC 3960	[a]	7.41	0.26	9.10	0.25	0.102	0.028	0.67	0.25	221	5
	[b]	7.36	0.29	9.20	0.27	0.111	0.031	0.76	0.25	221	5
NGC 5822	[a]	7.44	0.13	8.36	0.11	0.058	0.004	0.06	0.01	209	3
	[b]	7.34	0.12	8.53	0.11	0.075	0.004	0.08	0.03	209	3
NGC 6134	[a]	6.98	0.15	7.28	0.10	0.021	0.007	0.20	0.05	186	3
	[b]	6.95	0.11	7.33	0.15	0.027	0.006	0.45	0.14	187	3
NGC 6192	[a]	6.68	0.15	10.07	0.61	0.201	0.031	0.16	0.08	205	7
	[b]	6.46	0.17	10.17	0.60	0.222	0.032	0.20	0.11	203	7
NGC 6253	[a]	6.77	0.35	7.41	0.46	0.045	0.024	0.24	0.07	186	8
	[b]	6.74	0.34	7.47	0.50	0.051	0.024	0.36	0.14	185	9
NGC 6475	[a]	8.05	0.02	8.70	0.05	0.039	0.003	0.06	0.01	215	2
	[b]	8.01	0.02	8.82	0.05	0.048	0.002	0.08	0.02	217	1
NGC 6633	[a]	7.50	0.03	8.36	0.02	0.054	0.001	0.065	0.005	209	2
	[b]	7.44	0.02	8.50	0.03	0.067	0.002	0.09	0.02	209	1
NGC 6705	[a]	6.55	0.25	7.96	0.47	0.097	0.014	0.47	0.15	183	8
	[b]	6.42	0.27	8.10	0.46	0.115	0.012	0.59	0.12	183	9
NGC 6819	[a]	7.94	0.12	8.66	0.14	0.044	0.015	1.07	0.29	217	4
	[b]	7.88	0.12	8.82	0.16	0.057	0.016	1.14	0.32	218	4
NGC 7789	[a]	6.63	0.14	9.62	0.15	0.184	0.013	0.39	0.13	215	4
	[b]	6.65	0.16	9.63	0.15	0.183	0.012	0.45	0.08	215	3

Notes. Two lines are given for each cluster: the first line, labeled [(a)] in the 2nd column, lists the orbital parameters and their standard deviations in the axisymmetric model; the second line, [(b)] in the 2nd column, lists values for the bar and spiral arms combined model.

6.5.2 Current radial metallicity gradient

In Fig. 6.10 we show the radial distribution of metallicity for clusters in our sample. Metallicities and their uncertainties are collected from the literature (Table 6.2). The radial range of our sample is 6.5–12 kpc, spanning over the *inner* disk, when compared to the radial location of the discontinuity observed in the radial metallicity distribution of OCs at 12–13 kpc (Sect. 2.5.1). The radial distribution of our clusters metallicities can be well described by a single linear function. Weighted linear fit (where uncertainties of metallicity were used to calculate the weights as $1/\sigma^2_{[Fe/H]}$) gives the slope of $(-0.09 \pm 0.01)\,\mathrm{dex\,kpc^{-1}}$, in perfect agreement with Yong et al. (2012, see Fig 2.3) and other recent investigations of the radial metallicity gradient of the inner disk (see Sect. 2.5.1 for more references). This is not unexpected, since we use similar data (metallicities and solar distances) as other authors, however, our sample is smaller than these used in the most of the recent studies (e.g., Magrini et al., 2009; Pancino et al., 2010; Carrera & Pancino, 2011; Yong et al., 2012). In Fig. 6.10, the radial span from perigalacticon to apogalacticon

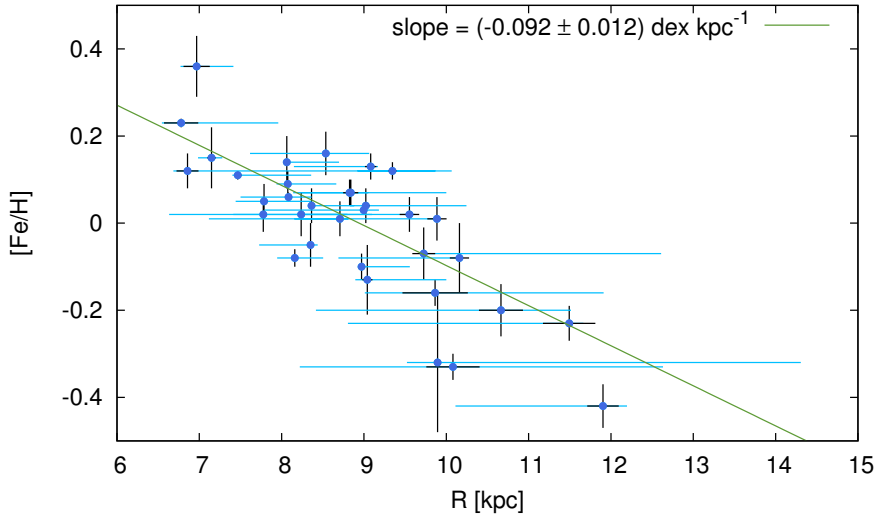

Figure 6.10: Radial distribution of metallicity for clusters in our sample. Uncertainties of [Fe/H] are shown by vertical black error-bars (Table 6.2); horizontal black error-bars show the uncertainties of the current clusters Galactocentric radius (σ_R in Table 6.2); horizontal blue lines span from the actual perigalacticon to apogalacticon for each cluster (calculated using the axisymmetric model, see Table 6.5). Green line shows weighted linear fit of the data (inverse squared errors of metallicity were used for the weighting).

of current orbits in the axisymmetric model is shown by blue horizontal lines for each cluster. For all clusters, these intervals are about order of magnitude larger than the uncertainty in the Galactocentric radius, σ_R, shown by the black error-bars.

Unfortunately, the radial range occupied by clusters in our sample (6.5–12 kpc) does not sufficiently cover the radii beyond the transition zone of the radial metallicity gradient located around 12–13 kpc (Sect. 2.5.1). Clearly, a larger sample, widely radially distributed, is necessary to study the clusters kinematics in the transition zone and in the outer disk.

6.5.3 Time evolution of the gradient

Figure 6.11 shows radial metallicity gradients for three age bins of 0–0.6 Gyr, 0.6–1.15 Gyr, and for clusters older than 1.15 Gyr. The age bins were chosen so that each bin contains similar number of clusters (11, 11, and 12 OCs, respectively). Similarly as in the case of the whole cluster sample (Fig. 6.10), a single weighted linear fit is applied on the data in each bin. Within their errors, the slopes are consistent with each other and hence we find an absence of any significant dependence of the radial metallicity gradient on age of clusters in our sample (see Sect. 2.5.1 for a brief summary of literature on this topic). We

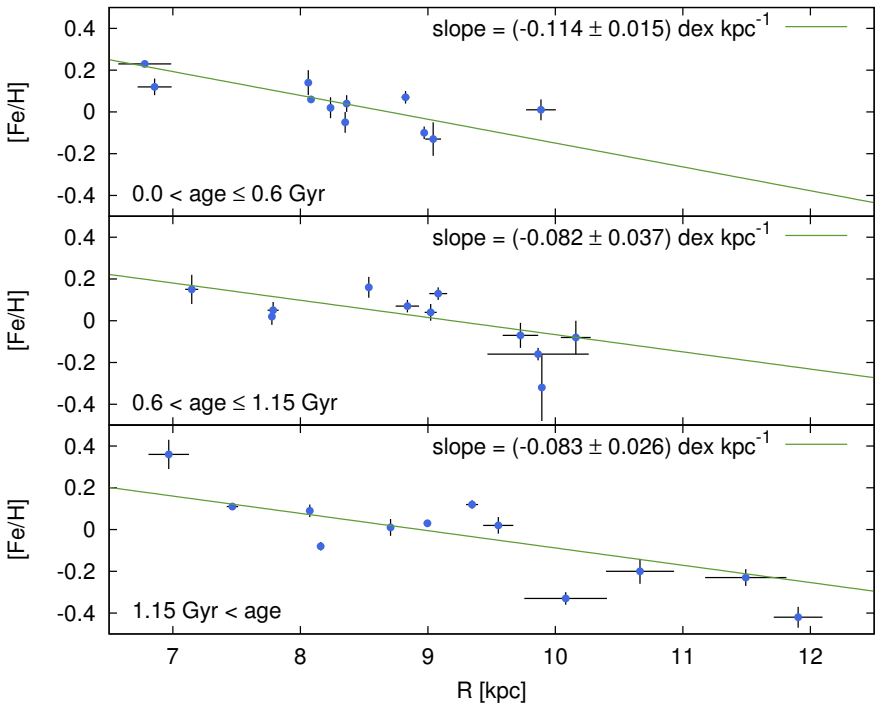

Figure 6.11: Radial distribution of metallicity for clusters in our sample (similar to Fig. 6.10) for different age bins. Age bins are indicated in the lower left corner of each plot. Values for the radial metallicity gradient are indicated in the upper right corners.

tested that this result does not change when the limiting ages for the individual bins are changed within reasonable limits.[5]

Assuming that the calculated orbits describe the past movement of clusters and that the clusters metallicity does not change in time, the metallicity gradient can be followed backward in time. Figure 6.12 shows such a time evolution of the radial metallicity gradient in the axisymmetric and the combined models, backward for time of 1 Gyr. We integrated orbits for all clusters in our sample backward and calculated the value of the radial metallicity gradient each 50 Myr. Similarly as above, sets of 1000 orbits were followed and the Galactocentric radius of each cluster was calculated as the mean value at given time. The resulting radial metallicity distribution was fitted with a weighted linear function where the inverse squared errors of metallicity were used as the weights. Figure 6.10 shows that the radial span perigalacticon–apogalacticon occupied by individual clusters during their current orbital cycle is large (generally $\sim$2 kpc, even thought it reaches up to 4 kpc for two clusters in the sample) compared to the uncertainty of their actual Galactocentric radii (maximal value of σ_R is 0.4 kpc, Table 6.2). The perigalacticon–

[5] Due to the relatively low numbers of OCs in the individual age bins, the gradient can sometimes be significantly influenced by presence or absence of a single cluster with small metallicity error (and therefore with a high weight). However, even in these cases, the gradients in different bins have mutually consistent values within their 2σ intervals.

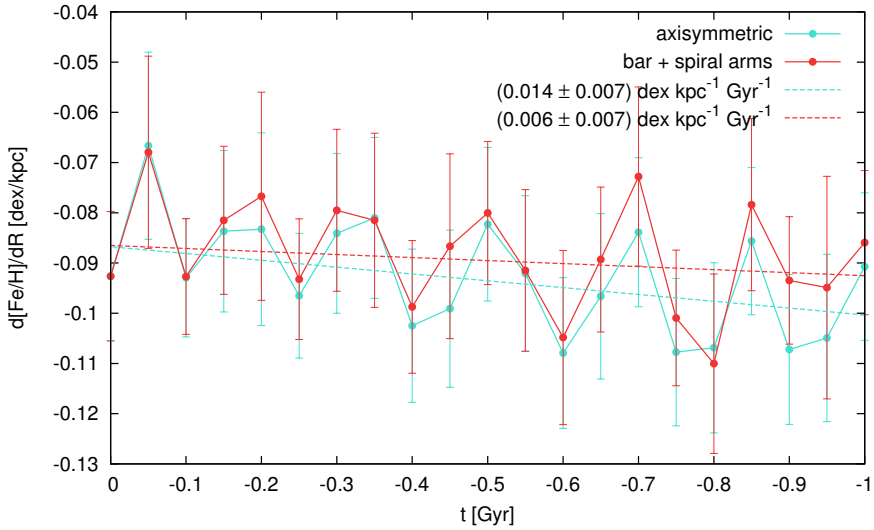

Figure 6.12: Time evolution of the radial metallicity gradient for the axisymmetric and the combined models. The blue point-line shows values of the radial metallicity gradient at different times calculated using the axisymmetric model. The red point-line shows the combined model. The time step for the radial metallicity gradient calculations is 50 Myr. The blue and red dashed lines are weighted linear fits of the time evolution for the axisymmetric and the combined model, respectively. Inverse squared uncertainties of the radial metallicity gradients at individual times were used as weights for these fits.

apogalacticon radial movement of clusters does not significantly differ in various Galactic models. Following the radial metallicity gradient at different orbital times with a time step of 50 Myr, fairly smaller than a typical azimuthal period of about 250 Myr (Fig. 6.9, Table 6.5), we can see if this nature of the Galactic orbits causes a time evolution of the radial metallicity gradient.

To estimate this, all OCs from the sample are used for the calculation of metallicity gradients in Fig. 6.12, even thought only 13 clusters from our sample are older than 1 Gyr. Dashed lines in Fig. 6.12 show weighted linear fits of the radial metallicity gradient time evolution. The inverse squared values of the errors of the radial metallicity gradient at individual times are used as the weights. The linear fits have values of $(0.014 \pm 0.007)\,\mathrm{dex\,kpc^{-1}\,Gyr^{-1}}$ and $(0.006 \pm 0.007)\,\mathrm{dex\,kpc^{-1}\,Gyr^{-1}}$ for the axisymmetric and the combined model, respectively. Hence, they are similar within their errors. Considering the typical error of the radial metallicity gradient at individual times of about $0.015\,\mathrm{dex\,kpc^{-1}}$ (see the error-bars in Fig. 6.12), the gradients are consistent with no significant evolution in time. We have investigated the orbits backward for longer integration time (5 Gyr back in time for all clusters in the sample) and there is no significant change in the behavior of the gradient. We have also followed the orbits in the other two model favors with a single non-axisymmetric component, bar or spiral arms, and the result do not differ significantly.

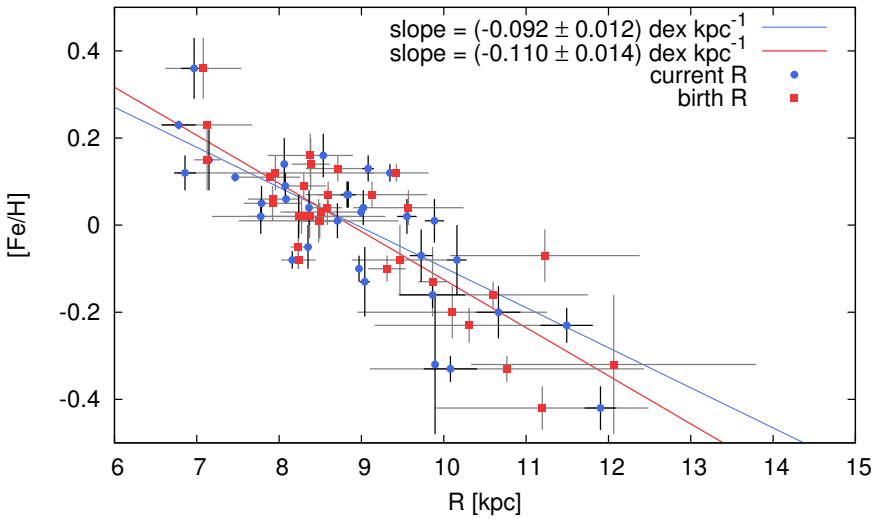

Figure 6.13: Clusters metallicity gradient based on the birth radii compared to their current radial metallicity distribution. Uncertainties of [Fe/H] are shown by vertical error-bars. Red squares with gray error-bars show the clusters birth radii and their uncertainties. Orbits were integrated in the axisymmetric model. Blue circles with black error-bars show the clusters current Galactocentric radii and their uncertainties, and are the same as in Fig. 6.10. Red and blue lines show the weighted linear fit to the birth radii and current radii dependencies, respectively. Inverse squared errors of metallicity were used for the weighting. Note that the metallicity is assumed to stay constant during cluster life and only the radius changes, hence the point representing given cluster moves only in the horizontal direction of the plot.

Since we know the age of OCs, it is possible to estimate clusters birth radii. Provided there was no time evolution of the gradient during the time since the oldest cluster in the sample was formed (about 7 Gyr for NGC 188), the birth radii, originating in different times, should correspond to the same metallicity gradient. To investigate this idea, we integrated clusters orbits backward for the integration time equal the age of each cluster. The observational uncertainties of the input data were taken into account in the same way as when calculating clusters current orbits, i.e., by drawing 1000 realization for the $d_\odot$, v_r, and PM components. Further, to consider the uncertainty in the age, the integration time of the individual integration was taken from a normal distribution with its mean equal the cluster age and the standard deviation equal the error (given in Table 6.1). The birth radius of each cluster was then calculated as the mean value of the 1000 realizations. From Figs. 6.11 and 6.12 we do not expect any significant time evolution of the gradient. This is confirmed in Fig. 6.13, where the metallicity gradient based on clusters birth radii is shown (the axisymmetric model was used for the integrations) and compared with the gradient based on current clusters Galactocentric radii. The value of the birth radii metallicity gradient is $(-0.11 \pm 0.01)\,\mathrm{dex\,kpc^{-1}}$ and it is, within the errors, consistent

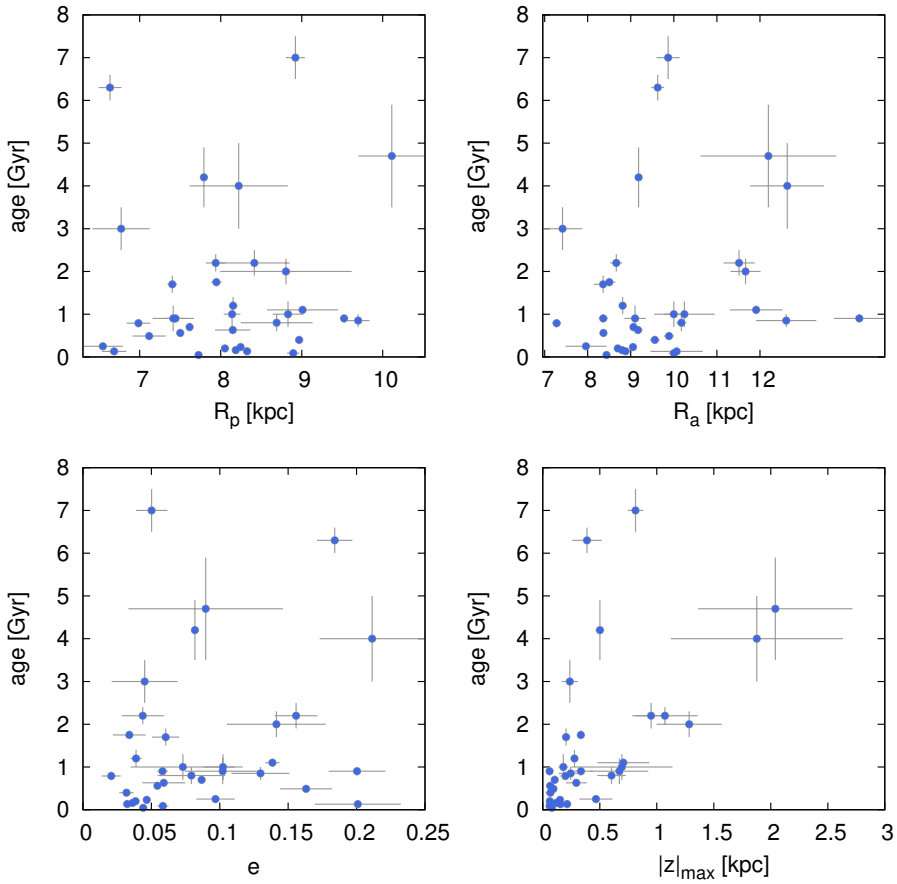

Figure 6.14: Perigalacticon distance, apogalacticon distance, eccentricity, and vertical amplitude of the recent orbits in the axisymmetric potential (Table 6.5) versus age (Table 6.1) for clusters in our sample.

with the gradient measured using the current radii of $(-0.09 \pm 0.01)\,\mathrm{dex\,kpc^{-1}}$. The birth radii calculated in the Galactic model including the non-axisymmetric components result in similar values of the gradient: $(-0.11 \pm 0.01)\,\mathrm{dex\,kpc^{-1}}$ for the barred and also the bar and spiral arms combined case, and $(-0.10 \pm 0.01)\,\mathrm{dex\,kpc^{-1}}$ for the model with the spiral arms.

6.5.4 Current orbital parameters versus age and metallicity

Figure 6.14 shows the perigalacticon distance (upper left plot), the apogalacticon distance (upper right plot), the eccentricity (bottom left plot) and vertical amplitude (bottom right plot) of clusters current orbits in the axisymmetric model versus their age. The plots look very similar for the combined bar and spiral arms model, since the orbital parameters themselves do not differ significantly for different model favors (Fig. 6.9). All orbits are close-to-circular ($e \lesssim 0.2$) and there is no strong trend between the clusters age and the perigalacticon distance, the apogalacticon distance, or the orbital eccentricity. The plot of the age versus vertical amplitude shows that the clusters with higher vertical amplitude

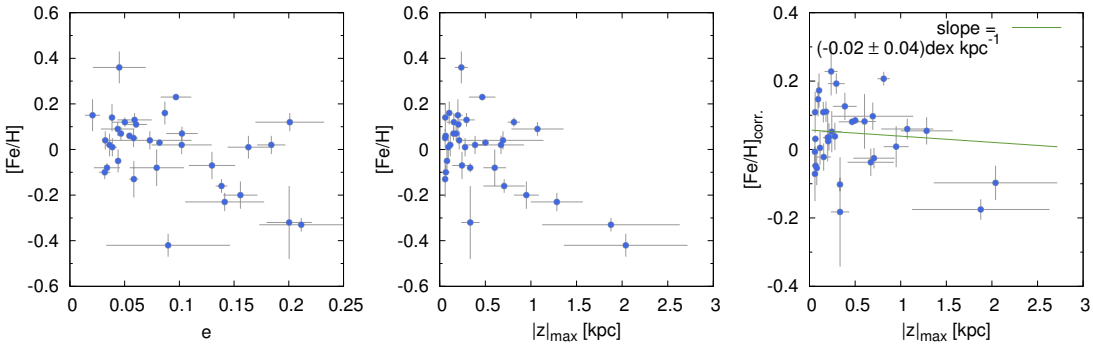

Figure 6.15: Vertical amplitude and eccentricity of the recent orbits in the axisymmetric potential (Table 6.5) versus metallicity (Table 6.2) for clusters in our sample. *Up:* eccentricity; *Bottom left:* vertical amplitude versus actual metallicity (Table 6.2); *Bottom right:* vertical amplitude versus metallicity corrected for the radial metallicity gradient of $-0.092\,\mathrm{dex\,kpc^{-1}}$ (Fig. 6.10) to the solar Galactocentric radius of 8.4 kpc. Green line shows weighted linear fit to the data (inverse squared errors of metallicity were used for the weighting).

($|z|_{\max} \gtrsim 1\,\mathrm{kpc}$) are generally older (age $\gtrsim 0.5\,\mathrm{Gyr}$, even thought several old clusters have vertical amplitude below 1 kpc), which confirms what have been already noticed in the previous investigations of OCs spatial distribution (Sect. 2.2).

Figure 6.15 shows orbital parameters (eccentricity and vertical amplitude) versus clusters metallicity. Similarly as in the case of clusters eccentricity and age, there seems to be no strong correlation between the eccentricity and metallicity. The plot of metallicity versus the vertical amplitude is in a way a *limiting* version of the vertical metallicity gradient which is not corrected for the radial metallicity gradient ($|z|_{\max}$ is the maximal vertical distance from the Galactic plane each cluster reaches during its current orbital period) and a trend of decreasing metallicity with increasing vertical amplitude can be seen. However, as described in Sect. 2.5.2, when estimating the vertical metallicity gradient, the clusters metallicity should be corrected for the radial gradient. The last plot of Fig. 6.15 shows this corrected vertical metallicity distribution. Metallicity was scaled by the radial gradient of $-0.092\,\mathrm{dex\,kpc^{-1}}$ (see Sect. 2.5.1 and Fig. 6.10) to the solar Galactocentric radius of 8.4 kpc. A weighted linear fit of this corrected vertical metallicity distribution (uncertainties of metallicity were used to calculate the weights as $1/\sigma^2_{\mathrm{[Fe/H]}}$) gives a very shallow slope, within its error clearly consistent with a flat distribution. Therefore we conclude that for the clusters in our sample, there is no significant evidence for a trend between clusters metallicity and vertical amplitudes of their current orbits.

Chapter 7

Summary and conclusions

The Galactic open clusters (OCs) provide a unique insight into various astrophysical processes. Due to the common evolution and properties of stars in clusters, it is generally possible to obtain their characteristics (e.g., clusters age, chemical composition, distance modulus, or kinematics) more easily and with better precision than for the field stars. These well known observational advantages of star clusters and the presence of a whole Galactic system of OCs have yielded many important and exciting results helping us to understand physical processes on different scales, from the stellar evolution, up to constraints on the chemodynamical evolution of the Milky Way (MW) thin disk and galactic disks in general. Kinematics is an important part of the information held by OCs and understanding the orbital history of OCs is crucial in the context of the bigger picture of the Galactic thin disk evolution.

This work focuses on the investigation of OCs orbits and we study two separate problems. In the first part of this thesis, we concentrate on a single object of the cluster NGC 6791. In the second part, we analyze the orbits of a sample of 34 OCs.

It is well known, from the observations as well as from the theoretical studies, that non-axisymmetric perturbations are essential for the chemodynamical evolution of the galactic disks. The presence of a bar or spiral arms can, among other important processes, induce radial migration of orbits in the disk. Radial migration happens whenever the mean Galactocentric radius of an orbit is changed without a significant dynamical heating (i.e., without dramatic increase in eccentricity or inclination). Several independent mechanisms inducing the radial migration have been described. One of them is the radial migration due to resonance overlap of multiple rotating patterns, which was recently revealed by Minchev & Famaey (2010, see Sect. 3.2.2). It is well known that the MW posses both, bar and spiral structure, and by taking these components simultaneously into account we aim to estimate the influence of the radial migration due to resonance overlap on orbits of OCs. We integrate the orbits in an analytical model consistent with an up-to-date picture of the MW (model description is given in Sect. 4). The model includes non-axisymmetric components, the Galactic bar and spiral arms, and we investigated the role

of the resonance overlap radial migration in the kinematic history of NGC 6791 and the sample of 34 OCs.

7.1 Open cluster NGC 6791

NGC 6791 is a particularly interesting member of the Galactic population of OCs. With an age of about 8 Gyr it is among the oldest OCs known, it is metal-rich, and its color-magnitude diagram posses many peculiarities (WD population and its cooling sequence, extreme horizontal branch stars and the UV upturn, or a possible evidence of prolonged star formation). Its location in the Galactic disk (at the Galactocentric radius of about 8 kpc) contradicts the classical picture of the metallicity gradient as traced by OCs, which is predicting a lover metallicity for a cluster at such a radius. Moreover, recently Geisler et al. (2012) observed an abundance spread among the stars in NGC 6791. While this phenomenon is common in the Galactic globular clusters, it is the first time it has been observed in an OC. The number of NGC 6791 extraordinary features (see Sect. 2.6 for a more detailed summary) poses the basic question of the cluster origin, which is still not well understood. Two main scenarios of the origin of NGC 6791 have been proposed – extragalactic origin and origin in the inner disk. We investigated a scenario in which the cluster is formed in the inner disk, close to the bulge, and then moved outward by the resonance overlap radial migration induced by the bar and spiral arms. This scenario might explain the high metallicity and age of the cluster, since the star formation close to the bulge is strong and the metal enrichment fast.

We conducted the investigation by integrating of orbits in an analytic model of the MW gravitational potential. The model consists of the axisymmetric part (with three components: bulge, disk, and halo) and it can include bar and spiral structure. First, we calculated the recent (1 Gyr back in time) orbit of NGC 6791 (Sect. 5.1). The initial conditions were derived using up-to-date observations and the observational uncertainties were taken into account in Monte Carlo fashion (by calculating a set of 1000 orbits with their initial conditions distributed according to proper motion, radial velocity, and distance errors). We found that orbits in the axisymmetric model and the models including rotating patterns differ only slightly. The orbit in the combined bar and spiral arms model is slightly more eccentric (with eccentricity up to 0.3), and has a higher vertical amplitude of about 1 kpc.

There are four other studies of NGC 6791 orbit published in literature (see Sect. 5.1.3 for more details). A direct comparison of these results is tricky, since the initial conditions differ depending on the input observational data available at given times. For example, Carraro et al. (2006), Wu et al. (2009), and Vande Putte et al. (2010) used older estimates of the proper motion (PM), radial velocity and solar distance, and hence their results cannot be directly compared with ours. Bedin et al. (2006) used similar initial observational data as this study, however we have identified a confusion in their initial condition calculation and so their results cannot be directly compared either.

To investigate whether the orbital parameters of the cluster current orbit could be achieved as a consequence of the resonance overlap radial migration mechanism, we also

followed a set of forward integrations (for 8 Gyr) with the initial positions closer to the Galactic center (with Galactocentric radii of 3–5 kpc). To this aim, we considered two different realizations of the MW gravitational potential – the present-day model, noted MW1 (the same we used for the backward integrations of NGC 6791); and a model with the rotating patterns more supporting the radial migration process, noted MW2. The MW2 model has a longer and more massive Galactic bar and also a stronger spiral arms. The angular velocity is decreased for the bar (to obtain the ratio of bar corotation and major axis consistent to that observed in most barred galaxies) and increased for the spiral arms (which brings their resonances closer to the Galactic center).

The purpose of this analysis, described in Sect. 5.2, was not to reproduce the cluster dynamical history precisely, but to estimate if the resonance overlap radial migration scenario is plausible, how efficient the migration induced by the MW bar and spiral structure could be, and how high the probability of the orbit realization within the limitations of our model is. We found that our MW2 model, that incorporates the bar and spiral arm perturbation, can produce orbits with the apogalacticon and perigalacticon distances similar to the actual values of NGC 6791. Thus we confirm the presence of the resonance overlap radial migration in the Galactic disk (compare the time evolution of orbital parameters in different flavors of our model in Figs. 5.4–5.6). However, the probability of this scenario, as quantified from our experiment, is very low, approximately 0.04% (see Sect. 5.2.3). Moreover, our migration scenario struggles to reproduce the vertical amplitude of NGC 6791.

Finally, we have also calculated an estimate of the initial mass of NGC 6791 (Sect. 5.3). We used the approximation of Lamers et al. (2005), where the mass loss from the cluster due to stellar evolution and due to two-body relaxation are directly taken into account and a constant tidal field is assumed (which corresponds to a circular orbit). The tidal shocks (interaction with giant molecular clouds or spiral arms) are not directly considered. Assuming the cluster has been living on a circular orbit approximately at the solar Galactocentric radius (about 8 kpc), that its current mass is 5000 $M_\odot$ and its age 8 Gyr, the initial mass estimated within the approximation is in the range $(1.5–4) \cdot 10^5 M_\odot$. The width of the range is mostly due to the uncertainty of the dissolution time scale for the two-body relaxation (we also discuss the influence of the uncertainties in cluster characteristics). Considering the suggested clusters scenarios of origin, its orbit was probably far away from close-to-circular one, possibly reaching the inner disk regions (even thought we find the probability of this scenario rather low) or being of an extragalactic origin. Therefore this estimate can be considered as a lower-limit for the real value of the cluster initial mass. Interestingly, the value falls between intervals of $(6–10) \cdot 10^5\, M_\odot$ and $10^{4.8}$–$10^5\, M_\odot$, which were theoretically estimated (by Bekki, 2011 and Vesperini et al., 2010, respectively) for the cluster initial mass limit necessary for a stellar system to form the second stellar generation and consequently to show an abundance spread.

7.2 Sample of open clusters

The second part of this manuscript is devoted to a study of the orbits of a sample of 34 OCs. The two most critical selection criteria for this sample were: availability of a high-resolution spectroscopic metallicity measurement in the literature (with $R \geq 15000$,

see Table 6.2 for numbers and references); and an estimate of the cluster mean PM vector based on the PMs of individual stars from the UCAC4 catalog (Zacharias et al., 2012b). We obtained the mean PM vectors for the sample clusters in an independent analysis using PMs of individual stars from the UCAC4 catalog. Other information necessary for the orbit calculations and further analysis – radial velocity (RV), solar distance, and age – was adopted from up-to-date literature (see Table 6.1).

The methods of obtaining the cluster mean PM vectors are described in Sects. 6.3, 6.4, and in Appendix B. Firstly, for those clusters with available high-resolution metallicity measurement (compilations including lists of such OCs are, e.g., Magrini et al., 2009, Carrera & Pancino, 2011 or Yong et al., 2012) we searched in the literature for the membership analysis based on RVs of the individual stars. Then, we made a cross-identification of the cluster RV-members with the stars in the UCAC4 catalog. This cross-identification method lead to the mean PM vector determination for 28 clusters. However, for a number of clusters, there was not enough stars to obtain a reliable mean PM vector via the cross-identification. To obtain the mean PM vector for these cases, we applied a nonparametric cluster–field separation method using the Gaussian kernel estimation of the cluster and field frequency functions. We obtained the mean PM vector for six more clusters (listed in Table 6.3). Additionally, the cluster–field separation method was tested for all clusters in our sample. The results generally agree well with these obtained via the cross-identification of the RV-members. Comments on individual clusters are given in Sect. 6.4. In Sect. 6.4.1 and Table C.1 we compare our mean PM vectors with several previous studies. In general, there is a good agreement and no systematic differences (average differences for individual PM vector components are in range 0.9–1.9 $\mathrm{mas\,yr^{-1}}$). Our results have generally higher errors of about 0.7 $\mathrm{mas\,yr^{-1}}$ compared to 0.4 $\mathrm{mas\,yr^{-1}}$ for four different previous studies.

The Galactic model, which was introduced for the investigation of the recent orbit of NGC 6791, was also used to study the orbits of our sample of 34 OCs. Uncertainties in the input observational data were taken into account in the similar way as for NGC 6791, by randomly generating 1000 sets of the initial conditions. Integrations were calculated forward in time and current orbits were characterized by the mean values of orbital parameters of the first completed orbital cycles. All clusters from our sample are located at Galactocentric radii of 6.5–12 kpc and the influence of the non-axisymmetric components is not prominent. Differences between orbital parameters derived using the axisymmetric model and models with non-axisymmetric components or their combination are relatively small compared to parameters uncertainties caused by the errors in the input observational data (Sect. 6.5.1). The presence of the bar and spiral arms generally increases the orbital eccentricity and vertical amplitude. Orbital parameters for the axisymmetric model and for the combined model including the Galactic bar and spiral arms are listed in Table 6.5. Figure D.1 shows the orbits projections into the Galactic and meridional plane.

Using the current Galactocentric radii of the OCs and their high-resolution metallicities, we obtained the radial metallicity gradient of $(-0.09 \pm 0.01)\,\mathrm{dex\,kpc^{-1}}$ (Sect. 6.5.2) that agrees with other investigations recently presented in the literature (which is expected, since similar data were used only for somewhat smaller sample). We investigated also a possible dependence of the radial metallicity gradient on clusters ages (Sect. 6.5.3).

We divided the sample into three different equally populated age bins and fitted the distributions to obtain their radial metallicity gradients. These have values consistent with each other within their uncertainties and we do not find any significant change of the metallicity gradient for clusters of different ages. This result is consistent with other studies (Carraro et al., 1998; Magrini et al., 2009, see Sect. 2.5.1).

Further, we aimed at estimating the time evolution of the radial metallicity gradient. We followed the orbits backward for 1 Gyr and constructed the gradient in time steps of 50 Myr. Assuming that the metallicities of individual clusters have not changed in time and that the calculated orbits represent the past positions of the clusters, this analysis can map the evolution of the radial metallicity gradient back in time. However, the metallicity gradients in different times do not show any significant evidence for the time evolution (Fig. 6.12). The uncertainties of the radial metallicity gradient at individual times are large compared to the changes of the gradient itself. A study of the radial metallicity gradient based on the clusters birth radii results in a similar conclusion (Fig. 6.13).

In Sect. 6.5.4 we investigated possible trends between clusters orbital parameters, age, and metallicity. However, apart from the trend that the older clusters generally have a higher vertical amplitude, we do not find any correlation between the age or metallicity and orbital parameters for our clusters.

To sum up, based on the results presented in Sect. 6, there does not seem to be any significant time evolution of the radial metallicity gradient for the OCs in our sample. Neither we found any prominent trends between clusters orbital parameters and metallicity or age. Moreover, the results obtained using the Galactic models including different non-axisymmetric components do not show much differences when compared with the axisymmetric case (apart from slightly higher eccentricities and vertical amplitudes). Several limiting factors have to be considered when drawing conclusions based on these results.

- Radial range of the sample: The range of the present-day Galactocentric radii of our OCs sample is 6.5–12 kpc. This is relatively far away from the Galactic center for the orbits to be prominently influenced by the central bar. At the same time, with the exception of the bar outer Lindblad resonance at the radius of 6.9 kpc (Table 5.5), no other resonant radii, where a possible influence of the non-axisymmetric patterns on the orbits is expected, is located within this radial range. The inner–outer disk transition region of the OCs radial metallicity distribution is observed at 12–13 kpc (Sect. 2.5.1) and our sample do not extend at these radii either.

- Size of the sample: Our sample consists of 34 OCs. These are the clusters with available high-resolution spectroscopic metallicity measurements for that it was possible to derive their mean PM vector using the UCAC4 catalog (see Sects. 6.2 and 6.3). We believe that our sample is as numerous as possible within the given constrains. However, compared with the number of observed OCs (more than 2000 OCs are listed in the catalog of Dias et al., 2002a, V3.2 of which about 500 have a measurement of the mean RV available), our sample is rather small. We find the key deficit in clusters PM information. It was not possible to derive an accurate PM vector

for many clusters located in the outer ($R > 12\,\mathrm{kpc}$) or the inner disk ($R < 6\,\mathrm{kpc}$). The situation with available data is expected to significantly improve with the upcoming astrometric Gaia mission (see, e.g., de Bruijne, 2012 for a brief summary about the mission).

- The Galactic model: The orbits were calculated using a Galactic model consistent with the present-day basic picture of the MW (Sect. 4). However, the model is relatively simple and some features possibly important for the radial migration are not included in the analysis, e.g., the transient spiral arms or the time evolution of individual non-axisymmetric components. While our model is an acceptable approximation when calculating the recent orbital parameters (characterizing the current orbital cycle with a typical duration of 250 Myr), it might be not sufficient for longer time scales. However, the relative uncertainties in the description of MW structure and evolution are generally much larger than these in the knowledge of the initial conditions, metallicity, or age of the OCs. On the one hand we are using up-to-date precise data to characterize the OCs, but on the other hand, we do not know the exact structure and evolution of the Galaxy, which is hence not possible to be precisely modeled.

Therefore, the fact that the results presented in Sect. 6 do not show any significant differences for orbits in the model including the bar and spiral arms, neither any significant time evolution does not directly indicates that OCs are not generally influence by the radial migration due to resonance overlap. With the results of the forward integration in the MW2 model (Sect. 5.2 dealing with the origin of NGC 6791 in the inner disk) we confirmed that the resonance overlap radial migration is present in the Galactic disk.

Appendix A

Force of the spiral arms model

Cox & Gómez (2002) proposed an expression for the potential of perturbation of a spiral density wave in their Eq. (8). We took the two-armed spiral ($N = 2$) and the simple sinusoid pattern (density described by Eq. (2) in Cox & Gómez, 2002). Then the potential can be written as (the same as Eqs. (4.12)–(4.16)),

$$\phi_{\mathrm{SA}}(R, z, \varphi) = -4\pi G h_{\mathrm{SA}} \rho_0 \exp\left(-\frac{R - R_0}{R_{\mathrm{SA}}}\right) \frac{1}{KD} \cos(\gamma) \left[\operatorname{sech}\left(\frac{Kz}{\beta}\right)\right]^{\beta}, \tag{A.1}$$

$$\text{where} \quad \gamma = 2\left[\varphi + \Omega_{\mathrm{SA}} t - \frac{\ln(R/R_0)}{\tan(\alpha)}\right]. \tag{A.2}$$

K, β, and D are functional parameters dependent on radius:

$$K = \frac{2}{R \sin(\alpha)}, \tag{A.3}$$

$$\beta = K h_{\mathrm{SA}}(1 + 0.4 K h_{\mathrm{SA}}), \tag{A.4}$$

$$D = \frac{1 + K h_{\mathrm{SA}} + 0.3(K h_{\mathrm{SA}})^2}{1 + 0.3 K h_{\mathrm{SA}}}. \tag{A.5}$$

The force vector is calculated as negative gradient of Eq. (4.12); in the cylindrical coordinates,

$$(F_R, F_\varphi, F_z) = -\left(\frac{\partial \phi}{\partial R}, \frac{1}{R}\frac{\partial \phi}{\partial \varphi}, \frac{\partial \phi}{\partial z}\right), \tag{A.6}$$

and we get

$$F_\varphi(R,\varphi,z) = \frac{2}{R}\tan(\gamma)\,\phi(R,\varphi,z), \tag{A.7}$$

$$F_R(R,\varphi,z) = \phi(R,\varphi,z)\Big\{ -\frac{1}{R_{\rm SA}} + \tan(\gamma)\frac{m}{R\tan(\alpha)} - \tag{A.8}$$

$$-K_R\left[\frac{1}{K} + z\tanh\left(\frac{Kz}{\beta}\right)\right] - \frac{D_R}{D} + \beta_R\left[\frac{Kz}{\beta}\tanh\left(\frac{Kz}{\beta}\right) + \ln\left(\frac{Kz}{\beta}\right)\right]\Big\},$$

$$F_z(R,\varphi,z) = K\tanh\left(\frac{Kz}{\beta}\right)\phi(R,\varphi,z), \tag{A.9}$$

where the subscript R in K_R, D_R, and β_R in Eq. (A.8) indicates the derivative of respected parameter with respect to R,

$$K_R = -\frac{2}{R^2\sin\alpha}, \tag{A.10}$$

$$D_R = K_R\frac{0.7h_{\rm SA} + 0.6Kh_{\rm SA}^2 + 0.09K^2h_{\rm SA}^3}{(1+0.3Kh_{\rm SA})^2}, \tag{A.11}$$

$$\beta_R = h_{\rm SA}K_R(0.8h_{\rm SA}K + 1). \tag{A.12}$$

Finally, the components of the force vector given in the cylindrical coordinates, Eqs. (A.7)–(A.9), were transformed into the Cartesian coordinate system which we use for the numerical orbit integrations (see Sects. 4.5.1 and 5.1.1).

Appendix B

Non-parametric membership determination

In this Appendix section, we describe technical details of the non-parametric cluster–field separation method used to obtain stars cluster membership probabilities and the cluster mean PM vectors. In the first part, Sect. B.1, we give a brief description of the theoretical background of the method. This section is strongly based (including the notation) on the work of Galadí-Enríquez et al. (1998), where we refer the reader for further details. The second part, Sect. B.2, describes the details of our implementation of the method including a practical example of its application (cluster NGC 2660).

B.1 Theoretical background

Let's have a 2-dimensional space of coordinates x, y (in our problem, they are the PM components, $\mu_\alpha \cos\delta$ and μ_α) where two populations of individuals are distributed; N_1 and N_2 are numbers of the individuals in each population (in our problem, they are the numbers of the cluster and the field stars in the sample). The populations are described by a probability density functions (PDFs), $\phi_1(x, y)$ and $\phi_2(x, y)$, for which

$$\iint_{-\infty}^{+\infty} \phi_i(x, y)\mathrm{d}x\,\mathrm{d}y = 1, \qquad i = 1, 2. \tag{B.1}$$

The frequency function of the populations then is

$$\Phi_i(x, y) = N_i\phi_i(x, y), \qquad i = 1, 2, \tag{B.2}$$

and the probability $P_i(x_*, y_*)$ of an individual at position (x_*, y_*) that it belongs to the population i is given by

$$P_i(x_*, y_*) = \frac{\Phi_i(x_*, y_*)}{\Phi_1(x_*, y_*) + \Phi_2(x_*, y_*)}. \tag{B.3}$$

The classical parametric method assumes specific parametric forms for the populations frequency functions and obtains their parameters by fitting the data (Sect. 6.3.1). The non-parametric method uses an empirical determination of the frequency functions without any assumption about their shape, e.g., via the kernel estimator (as firstly proposed by Cabrera-Cano & Alfaro, 1990).

The empirical frequency function Ψ at position (x, y) can be estimated as

$$\Psi(x, y) = \sum_{i=1}^{N} K(x - x_i, y - y_i), \tag{B.4}$$

where N is the total number of individuals in the sample (from both populations, $N = N_1 + N_2$) and the summation goes over all individuals; $K(x, y)$ is the kernel function. To determine h, we followed Cabrera-Cano & Alfaro (1990) and Galadí-Enríquez et al. (1998), we used a circular Gaussian kernel,

$$K(x, y) = \frac{1}{2\pi h^2} \exp\left(-\frac{1}{2}\frac{x^2 + y^2}{h^2}\right), \tag{B.5}$$

where h is the standard deviation of the Gaussian distribution and is usually called smoothing parameter or window width.[1] Following Chen (1996) and Galadí-Enríquez et al. (1998) we use the rule proposed by Silverman (1986),

$$h = \left(\frac{4}{d+2}\right)^{1/(d+4)} \sigma N^{-1/(d+4)}, \qquad \sigma^2 = \sum_{i=1}^{d} \sigma_i^2/d, \tag{B.6}$$

where d is the dimension of the space and σ_i are the standard deviations of the observed data coordinates. In our case $d = 2$ and the equation reduces to expression $h = \sigma N^{-1/6}$, where $\sigma = \sqrt{\frac{1}{2}(\sigma_1^2 + \sigma_2^2)}$.

The empirical frequency function can be calculated on a grid in the coordinate space. Let (x_a, y_b) be the grid points coordinates, then we tabulate the empirical frequency function at these points, $\Psi(x_a, y_b); a = 1, \ldots, n_a; b = 1, \ldots, n_b$, where n_a and n_b are total numbers of the grid points for each dimension. The empirical frequency function $\Psi(x_a, y_b)$ can be transformed into empirical PDF, $\psi(x_a, y_b)$, by normalization to the unit volume (following the Eq. (B.2)),

$$\psi(x_a, y_b) = \Psi(x_a, y_b) \left[\sum_{i=1,j=1}^{n_a,n_b} \Psi(x_i, y_j)\Delta x \Delta y\right]^{-1}, \tag{B.7}$$

where Δx and Δy are sizes of the grid cells.

[1] The smoothing parameter h determines the characteristic size of the kernel. In other words, it sets how distant individuals will contribute to the empirical frequency function at any given point. The exact form of the dependency of the individual contributions to the frequency function is given by the kernel function, which is analogical to a weighting function. An h of small value relatively to distances between observed points, could lead to noisy results (smoothing too sensitive to individual points); while a large value could lead to blurring out characteristic patterns of the frequency function. In the ideal case, $N \to \infty$ and then $h \to 0$, see Eq. (B.6).

When the cluster and the field populations are present in the sample, the empirical frequency function is a sum of individual frequency functions for the cluster, $\Psi_{\rm c}$, and the field, $\Psi_{\rm f}$: $\Psi_{\rm c+f} = \Psi_{\rm c} + \Psi_{\rm f}$. To obtain the cluster empirical frequency function, the combined empirical frequency function $\Psi_{\rm c+f}$ needs to be decomposed by subtracting the field contribution $\Psi_{\rm f}$. $\Psi_{\rm f}$ can be estimated, e.g., following Galadí-Enríquez et al. (1998), who used the fact of the limited cluster angular size – cluster stars are assumed to be found only within the circle of cluster radius $r_{\rm c}$. Cluster contribution beyond this radius is considered negligible, and the area outside $r_{\rm c}$ is assumed to be occupied only by the field stars. If it is further assumed that the field stars located within the cluster radius have the same PDF as the field stars in the area beyond the cluster radius, this area can be used to estimate the field empirical frequency function in the cluster area. Typically, a corona zone, limited by inner and outer radii, $r_{\rm f,in}$ and $r_{\rm f,out}$, respectively, centered on the cluster is used to calculate the field empirical frequency function noted $\Psi_{\rm f,cor}$ (Galadí-Enríquez et al., 1998; Balaguer-Núñez et al., 2004b,a, 2005, 2007). Finally, $\Psi_{\rm f,cor}$ needs to be scaled for a different spatial area of the corona and the circle covering the cluster. Assuming the same spatial density of the field stars inside the corona and within the cluster radius, this can be done through multiplying by the area factor,

$$\Psi_{\rm f} = \Psi_{\rm f,cor}\,\frac{r_{\rm c}^2}{r_{\rm f,out}^2 - r_{\rm f,in}^2}. \tag{B.8}$$

Following Eq. (B.3), the cluster membership probability of a star located at the given point (x_a, y_b) of the grid is,

$$P_{\rm c}(x_a, y_b) = \frac{\Psi_{\rm c+f}(x_a, y_b) - \Psi_{\rm f}(x_a, y_b)}{\Psi_{\rm c+f}(x_a, y_b)}. \tag{B.9}$$

The probability of the individual sample stars is then taken as the probability of the nearest grid point.

B.2 Our implementation of the method

The input characteristics of the cluster–field separation method are the cluster central coordinates (α, δ) and the cluster angular radius $r_{\rm c}$. The central coordinates were taken from the CDS. For the central coordinates, different sources give very similar values and the differences between various sources are well below the values significantly influencing the method. Situation is different in the case of the cluster radius for which, in some cases, various sources give a significantly different values (see for example the discussion in Sect. 6.4 for clusters NGC 2660, NGC 3680, or NGC 6705). Therefore, the cluster radii were treated individually, using values from various sources and the cluster–field separation method was tested for a range of radii of values similar to those published in the literature; see paragraphs in Sect. 6.4 for comments on individual clusters. The final values of the central coordinates and clusters angular radii are given in Table 6.3.

For the given values of cluster central coordinates and radius, the data from the UCAC4 catalog were queried via the CDS VizieR Service.[2] Stars located within the

[2] `http://vizier.u-strasbg.fr/viz-bin/VizieR?-source=ucac4`.

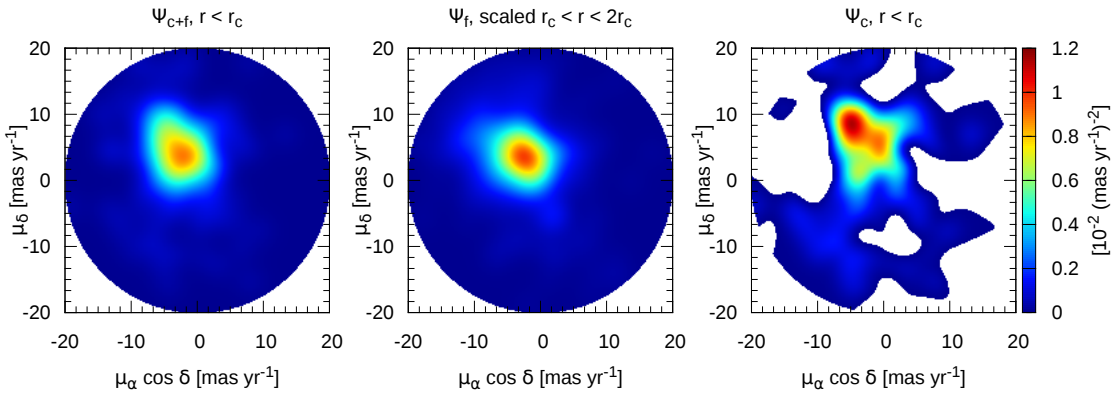

Figure B.1: Empirical PDFs for NGC 2660. *Left:* $\psi_{\mathrm{c+f}}(\mu_\alpha \cos\delta, \mu_\alpha)$ – mixed empirical PDF of cluster and field stars within the cluster radius r_c; *Middle:* $\psi_\mathrm{f}(\mu_\alpha \cos\delta, \mu_\alpha)$ – empirical PDF for field stars derived from the scaled empirical frequency function calculated within the corona (using Eq. (B.8)); *Right:* $\psi_\mathrm{c}(\mu_\alpha \cos\delta, \mu_\alpha)$ – PDF of cluster stars, derived from the empirical frequency function $\Psi_\mathrm{c} = \Psi_\mathrm{c+f} - \Psi_\mathrm{f}$ via normalization (Eq. (B.7)).

radius equal to $2r_\mathrm{c}$ and with available values of their PM components and available magnitude information from the 2MASS survey (J, H, and K magnitudes and their errors) in the catalog were queried. Further, to avoid measurements with large uncertainties and possible outliers (similarly as, e.g., Galadí-Enríquez et al., 1998; Frinchaboy & Majewski, 2008), we applied PM cut-off: $|\mu| < 20\,\mathrm{mas\,yr^{-1}}$, PM error cut-off: $\sigma_\mu < 5\,\mathrm{mas\,yr^{-1}}$, and magnitude cut-off: $J < 16\,\mathrm{mag}$.

We used an equidistant grid with square cells of $0.2 \times 0.2\,\mathrm{mas\,yr^{-1}}$, a size far below the observational errors of the UCAC4 catalog (about $4\,\mathrm{mas\,yr^{-1}}$ Zacharias et al., 2012a). We determined the empirical frequency function of the field using the stars from a circular corona limited by radii $r_\mathrm{f,in} = r_\mathrm{c}$ and $r_\mathrm{f,out} = 2r_\mathrm{c}$. The mean cluster PM is taken at the maximal value of the cluster empirical PDF. Cluster membership probability was calculated following Eq. (B.9) for each nod of the grid; probability for individual stars was then taken as the probability of the nearest nod.

To consider the errors in the stars PM components, we randomly generated ten datasets of the stars PM – for each star, 10 values of each PM component were generated, having a normal distribution with the mean equal the PM value from the UCAC4 catalog and the standard deviation equal the PM error of the given star in the catalog. The cluster–field separation method was carried out for each such dataset. The final cluster PM vector was calculated as the mean of the individual runs results and its error estimated as their standard deviation. The membership probability for individual stars was taken as the mean value of individual probabilities obtained from all runs.

B.2.1 Example – NGC 2660

We illustrate our implementation of the cluster–field separation method on an example of the cluster NGC 2660. In Fig. B.1, we plot the empirical PDFs of NGC 2660. The left plot shows the combined PDF, $\psi_\mathrm{c+f}$, calculated within the cluster radius $r_\mathrm{c} = 10'$ (see

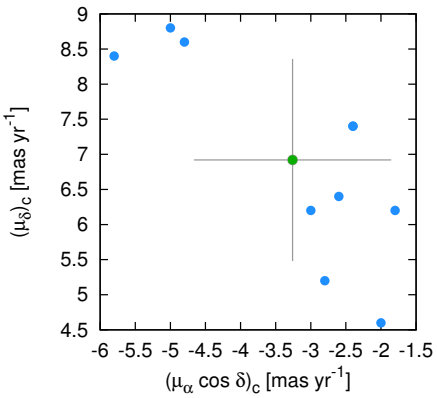

Figure B.2: VPD of the mean cluster PM vectors resulting from the 10 random data realizations for NGC 2660. Results of individual realizations are shown with blue points (the PM vector with coordinates of $\mu_\alpha)_{\max} = (-2.4, 7.4)\,\mathrm{mas\,yr^{-1}}$ resulted from two different realizations); their uncertainty is given by the grid cell size of $0.2\,\mathrm{mas\,yr^{-1}}$. The green point with error-bars shows the final mean cluster PM vector and its standard deviation.

paragraph NGC 2660 in Sect. 6.4 for the details of the cluster radius choice). The plot in the middle corresponds to the field empirical PDF, ψ_f, that was derived by scaling of the empirical frequency function $\Psi_\mathrm{f,cor}$ of the corona within the radii r_c and $2r_\mathrm{c}$, see Eq. (B.8), and by the normalization, see Eq. (B.7). Comparing these two plots, it can be seen that the shape of the combined PDF, $\psi_\mathrm{c+f}$, differs from the one of ψ_f by an excess around $(\mu_\alpha \cos\delta, \mu_\alpha) \sim (-5, 8)\,\mathrm{mas\,yr^{-1}}$. This excess corresponds to the cluster PDF. The ψ_c is showed in the right plot of Fig B.1 and its maximum is at the grid nod with coordinates $(\mu_\alpha \cos\delta, \mu_\alpha)_{\max} = (-4.8, 8.6)\,\mathrm{mas\,yr^{-1}}$, which corresponds to the cluster mean PM vector (for this realization of the dataset).

Since the field PDF in the corona, $\psi_\mathrm{f,cor}$, does not perfectly represent the field PDF inside the cluster radius, ψ_f, the cluster empirical PDF, noted ψ_c, reaches negative in some areas (white area within the considered circle of $20\,\mathrm{mas\,yr^{-1}}$ in the right plot of Fig. B.1 showing the ψ_c). To avoid these negative zones when calculating the cluster membership probabilities by Eq. (B.9), the probabilities were considered only for the grid points located where the cluster empirical PDF has values above a certain level of noise, ς. This noise is introduced by the unavoidable discrepancy between the empirical field PDF in the corona and that within the cluster radius. The level of noise was calculated as the mean PDF value over the grid points with a negative ψ_c and the probability was calculated only for the grid points with $\psi_\mathrm{c} > 3|\varsigma|$; in the case of NGC 2660, $|\varsigma| = 0.33 \cdot 10^{-3}\,(\mathrm{mas\,yr^{-1}})^{-2}$.

The described procedure was carried out for 10 random realization of the UCAC4 PM data. The final results of the cluster PM vector and membership probabilities of individual stars were calculated as the mean values over these realizations. Figure B.2 demonstrates the distribution of the cluster mean PMs from the individual realizations and the final

cluster mean PM estimate. The distribution of individual stars color-coded by their final cluster membership probability (the mean from all 10 runs of the data randomly generated from the UCAC4 values of PM and their dispersions) in the coordinate space (α, δ), their VPD, and their CMD based on the 2MASS magnitudes, are showed in Fig. 6.4. The final mean cluster mean PM vector is marked by the red cross in the VPD.

Appendix C

PMs of OCs in our sample

Table C.1: PMs of OCs in our sample.

Cluster	$\mu_\alpha \cos\delta$ [mas yr^{-1}]	σ_{μ_α}	μ_δ [mas yr^{-1}]	σ_{μ_δ}	Ref.
Blanco 1	20.17	0.51	3.00	0.51	(9)
	19.86	0.26	2.37	0.26	(3)
	17.9	0.21	1.65	0.29	(17)
	20.11	0.35	2.43	0.25	(16)
	18.9	0.2	3.2	0.2	(10)
IC 2602	−17.49	0.22	10.10	0.22	(9)
	−14.16	0.37	11.11	0.29	(3)
	−22.33	0.71	9.93	0.68	(2)
	−17.02	0.24	11.15	0.23	(16)
	−14.9	1.6	7.9	1.3	(10)
IC 4651	−1.07	0.5	−2.20	0.5	(9)
	−2.09	0.27	−3.28	0.27	(1)
	1.5	1.56	−5.35	0.87	(4)
	0.64	0.13	−1.11	0.12	(2)
	−0.81	0.37	−2.17	0.31	(3)
	−1.72	0.7	−2.76	0.69	(11)
	−1.6	1.0	−3.0	1.0	(14)
	−1.2	0.6	−2.5	1.0	(10)
Melotte 66	−4.28	0.49	3.96	0.49	(1)
	−4.18	0.61	7.67	1.56	(2)
	−2.0	1.0	1.2	0.6	(10)
Melotte 71	−2.19	0.25	5.15	0.25	(1)
	−3.59	0.49	6.26	0.43	(3)
	−0.90	0.11	1.14	0.11	(2)
	−4.7	0.6	7.5	0.6	(10)
NGC 188	−1.48	1.25	−0.56	1.24	(4)

Continued on next page.

Table C.1: PMs of OCs in our sample – continued from previous page.

Cluster	$\mu_\alpha \cos\delta$ [mas yr^{-1}]	σ_{μ_α}	μ_δ [mas yr^{-1}]	σ_{μ_δ}	Ref.
	−0.94	1.16	1.13	0.28	(2)
	−2.56	0.2	0.18	0.2	(8)
	−2.9	0.6	−1.4	0.5	(10)
NGC 752	7.50	0.32	−11.50	0.32	(7)
	8.29	0.91	−11.34	0.80	(4)
	8.02	0.20	−11.68	0.19	(2)
	7.66	0.23	−12.15	0.26	(3)
	7.7	0.1	−11.9	0.1	(10)
NGC 1039	0.39	0.78	−6.80	1.04	(4)
	−0.1	0.2	−7.2	0.2	(9)
	−0.29	0.17	−5.78	0.17	(1)
	−0.22	0.17	−6.93	0.20	(3)
	0.03	0.18	−7.43	0.18	(2)
	0.2	0.4	−6.3	0.3	(10)
NGC 1545	−0.04	0.28	0.79	0.37	(2)
	−1.63	0.77	−1.00	0.45	(3)
	0.45	1.18	−3.12	0.78	(4)
	0.25	0.70	0.20	0.70	(9)
	−1.7	0.3	0.2	0.4	(10)
NGC 1817	−0.19	0.31	−4.86	0.31	(1)
	0.14	0.21	−4.2	0.24	(2)
	−0.06	0.63	−3.13	0.53	(3)
	0.29	0.10	−0.96	0.07	(5)[a]
	0.0	0.2	−0.8	0.2	(5)[b]
	2.66	0.18	−3.72	0.19	(6)
	1.02	1.06	−6.51	1.06	(7)
	−2.2	0.5	−0.7	0.4	(10)
NGC 2099	2.47	0.17	−6.65	0.17	(1)
	3.29	0.18	−6.84	0.17	(2)
	3.09	0.23	−7.35	0.25	(3)
	3.36	2.52	−6.17	1.78	(4)
	3.78	0.29	−7.09	0.29	(7)
	4.5	1.2	−7.4	1.2	(11)
	2.5	0.3	−7.0	0.3	(10)
NGC 2204	4.04	0.77	0.09	0.77	(1)
	−0.22	0.48	1.78	0.44	(2)
	1.0	0.7	1.5	0.6	(10)
NGC 2243	−3.66	0.61	3.32	0.61	(1)
	2.53	0.54	2.90	1.30	(2)
	1.0	1.1	5.3	1.3	(10)
NGC 2355	−1.76	0.55	−4.28	0.55	(1)
	−0.39	0.32	−4.78	0.30	(6)
	−2.5	0.8	−3.0	1.5	(13)
	−2.5	0.5	−3.2	0.8	(10)
NGC 2360	3.61	1.49	8.07	1.57	(4)
	−2.88	0.51	5.37	0.51	(7)
	−2.68	0.28	6.37	0.28	(1)

Continued on next page.

Table C.1: PMs of OCs in our sample – continued from previous page.

Cluster	$\mu_\alpha \cos\delta$ [mas yr^{-1}]	σ_{μ_α}	μ_δ [mas yr^{-1}]	σ_{μ_δ}	Ref.
	−2.62	0.30	4.89	0.32	(3)
	−4.30	0.27	6.68	0.29	(2)
	−2.7	0.5	6.0	0.4	(10)
NGC 2420	−1.32	0.42	−4.18	0.26	(2)
	−0.7	0.9	−2.8	0.5	(10)
NGC 2447	−5.12	0.33	3.66	0.33	(1)
	−3.64	0.08	2.60	0.08	(2)
	−3.76	0.27	3.91	0.21	(3)
	−1.98	1.36	5.42	1.26	(4)
	−4.85	0.33	4.47	0.33	(7)
	−5.2	0.6	4.3	0.6	(11)
	−4.9	0.6	4.0	0.3	(10)
NGC 2477	−2.13	0.2	2.71	0.2	(1)
	2.63	0.26	3.6	0.29	(2)
	−0.23	0.56	1.83	0.29	(3)
	−0.65	0.6	1.13	0.59	(10)
NGC 2539	−3.6	0.15	−1.53	0.14	(2)
	−3.37	0.23	−1.87	0.26	(3)
	−2.5	1.11	−1.22	1.12	(4)
	−4.07	0.27	−1.83	0.27	(7)
	−3.82	0.85	−3.35	0.82	(11)
	−4.13	1.4	−1.7	0.6	(10)
NGC 2632	−35.58	0.19	−12.90	0.19	(9)
	−35.9	0.13	−12.88	0.11	(3)
	−35.99	0.14	−12.92	0.14	(4)
	−35.81	0.29	−12.85	0.24	(16)
	−35.3	0.3	−12.4	0.2	(10)
NGC 2660	−5.82	0.81	7.40	0.83	(2)
	−3.26	1.4	6.92	1.4	(10)
NGC 2682	−8.62	0.28	−6.0	0.28	(9)
	−6.47	1.29	−6.27	1.01	(4)
	−6.51	0.30	−4.54	0.28	(2)
	−8.31	0.26	−4.81	0.22	(3)
	−8.23	0.05	−5.72	0.05	(6)
	−7.87	0.61	−5.6	0.59	(11)
	−9.6	1.1	−3.7	0.8	(12)
	−7.1	0.8	−7.6	0.4	(13)[a]
	−7.1	0.7	−7.7	0.5	(13)[b]
	−9.1	0.3	−4.3	0.2	(10)
NGC 3114	−5.25	0.38	4.58	0.38	(1)
	−7.09	0.09	4.03	0.09	(2)
	−7.42	0.19	4.05	0.22	(3)
	−7.47	0.26	4.03	0.21	(4)
	−7.54	0.21	3.50	0.21	(9)
	−5.9	0.4	4.2	0.3	(10)
NGC 3680	−3.11	1.64	−5.30	0.98	(4)
	−5.86	0.62	1.90	0.62	(9)

Continued on next page.

Table C.1: PMs of OCs in our sample – continued from previous page.

Cluster	$\mu_\alpha \cos\delta$ [mas yr^{-1}]	σ_{μ_α}	μ_δ [mas yr^{-1}]	σ_{μ_δ}	Ref.
	−6.44	0.68	2.02	0.68	(1)
	−5.38	0.44	1.54	0.45	(3)
	−6.00	0.30	0.90	0.28	(2)
	−5.8	0.6	1.1	0.6	(11)
	−6.1	0.8	1.0	0.4	(10)
NGC 3960	−7.70	0.73	3.22	0.73	(1)
	−7.01	0.24	−0.45	0.33	(2)
	−4.2	3.6	1.9	4.0	(14)
	−8.9	1.4	5.2	1.3	(10)
NGC 5822	−6.20	0.16	−6.08	0.16	(1)
	−6.50	0.12	−5.85	0.11	(2)
	−7.46	0.19	−5.66	0.25	(3)
	−8.34	1.36	−2.65	1.33	(4)
	−7.95	0.24	−8.20	0.24	(9)
	−8.6	0.9	−8.8	0.9	(11)
	−8.2	0.7	−6.1	0.5	(10)
NGC 6134	−0.86	0.88	−4.60	0.88	(9)
	−1.26	0.27	−6.50	0.27	(1)
	0.32	0.89	−5.88	0.48	(3)
	0.48	0.14	−3.13	0.16	(2)
	−0.11	1.12	−6.97	1.09	(11)
	−1.6	1.4	−6.4	1.6	(14)
	−0.7	0.6	−5.9	0.5	(10)
NGC 6192	−2.67	0.34	−0.91	0.34	(1)
	0.64	0.30	−3.39	0.41	(2)
	1.8	0.83	−0.77	0.39	(3)
	0.5	1.9	1.4	1.7	(14)
	3.73	0.83	3.18	1.39	(15)[c]
	2.7	0.9	2.94	1.2	(10)
NGC 6253	−1.7	1.2	−3.5	1.9	(10)
NGC 6475	2.58	0.08	−4.54	0.07	(2)
	2.83	0.15	−5.14	0.15	(3)
	2.61	0.33	−4.80	0.22	(4)
	1.67	0.20	−3.60	0.20	(9)
	1.1	0.4	−3.7	0.4	(10)
NGC 6633	0.23	0.11	−1.54	0.13	(2)
	0.1	0.22	−2.00	0.24	(3)
	2.67	0.75	−0.01	0.66	(4)
	−0.21	0.31	−1.60	0.31	(9)
	0.2	0.4	−1.0	0.4	(10)
NGC 6705	−6.27	0.30	−3.55	0.30	(1)
	−6.51	0.49	−0.48	0.41	(3)
	−6.55	0.25	−0.04	0.38	(2)
	−4.63	0.48	−1.10	0.48	(7)
	−5.4	1.2	−0.3	1.2	(11)
	−4.1	0.7	−1.3	1.2	(10)
NGC 6819	−5.33	0.5	−2.76	0.5	(1)

Continued on next page.

Table C.1: PMs of OCs in our sample – continued from previous page.

Cluster	$\mu_\alpha \cos\delta$ [mas yr^{-1}]	σ_{μ_α}	μ_δ [mas yr^{-1}]	σ_{μ_δ}	Ref.
	−2.66	0.67	−3.93	0.78	(2)
	−5.8	1.0	−2.8	1.1	(10)
NGC 7789	−2.20	0.22	−1.11	0.18	(2)
	3.03	0.56	−0.58	0.54	(3)
	1.7	0.3	−2.4	0.6	(10)

Notes. [(a)] Result of the parametric membership determination of Balaguer-Núñez et al. (2004b) and Balaguer-Núñez et al. (2007). [(b)] Result of the non-parametric membership determination of Balaguer-Núñez et al. (2004b) and Balaguer-Núñez et al. (2007). [(c)] Values from the catalog of Dias et al. (2002a, V3.2) catalog, where they refer to Magrini et al. (2010) as to the source. However, the mean PM in Magrini et al. (2010, Table10) is different (see the reference (14) for the same cluster) and therefore the source of these values stays unclear to us.

References. (1) Dias et al. (2006); (2) Loktin & Beshenov (2003); (3) Kharchenko et al. (2005a); (4) Baumgardt et al. (2000); (5) Balaguer-Núñez et al. (2004b); (6) Krone-Martins et al. (2010); (7) Dias et al. (2002a); (8) Platais et al. (2003); (9) Dias et al. (2001); (10) this study; (11) Frinchaboy & Majewski (2008); (12) Bellini et al. (2010a); (13) Soubiran et al. (2000); (14) Magrini et al. (2010); (15) Dias et al. (2002a, V3.2); (16) van Leeuwen (2009); (17) Mermilliod et al. (2008b)

Appendix D

Plots of OCs orbits

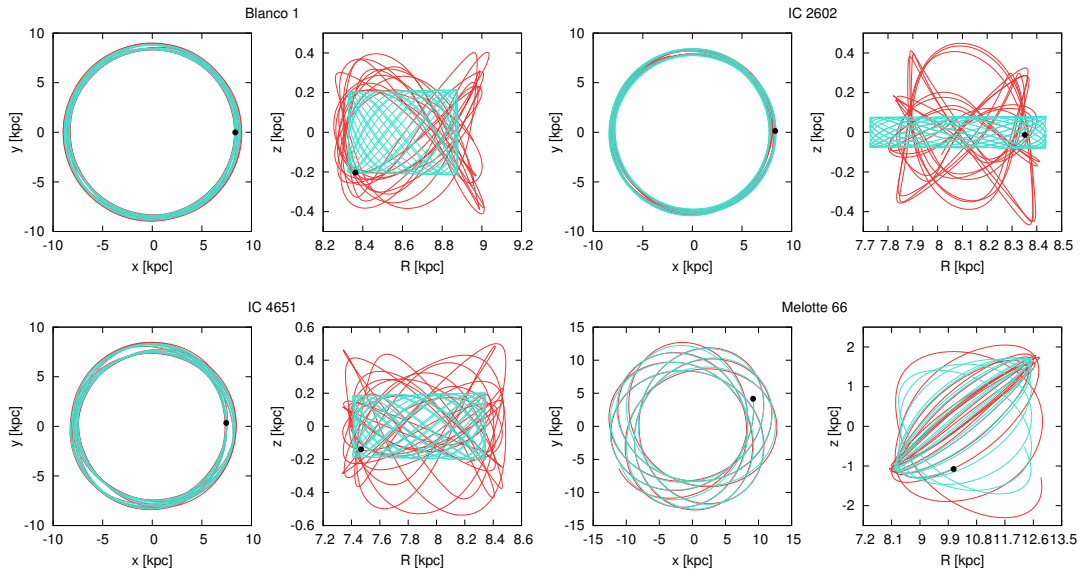

Figure D.1: Orbits of OCs from our sample. Two clusters are plotted at each line. The projection into the Galactic (x, y) and meridional plane (R, z) is plotted for each cluster. Cluster name is indicated above each pair of plots. Orbit in the axisymmetric potential is plotted with blue line. Red line shows orbit in the combined model including bar and spiral arms. The black dot marks the initial position of the cluster. The initial conditions are given by the mean input observational data (see Table 6.1 for $d_\odot$ and v_r, Table C.1 for PMs). Integrations were forward for time of 2 Gyr. Continued on next pages.

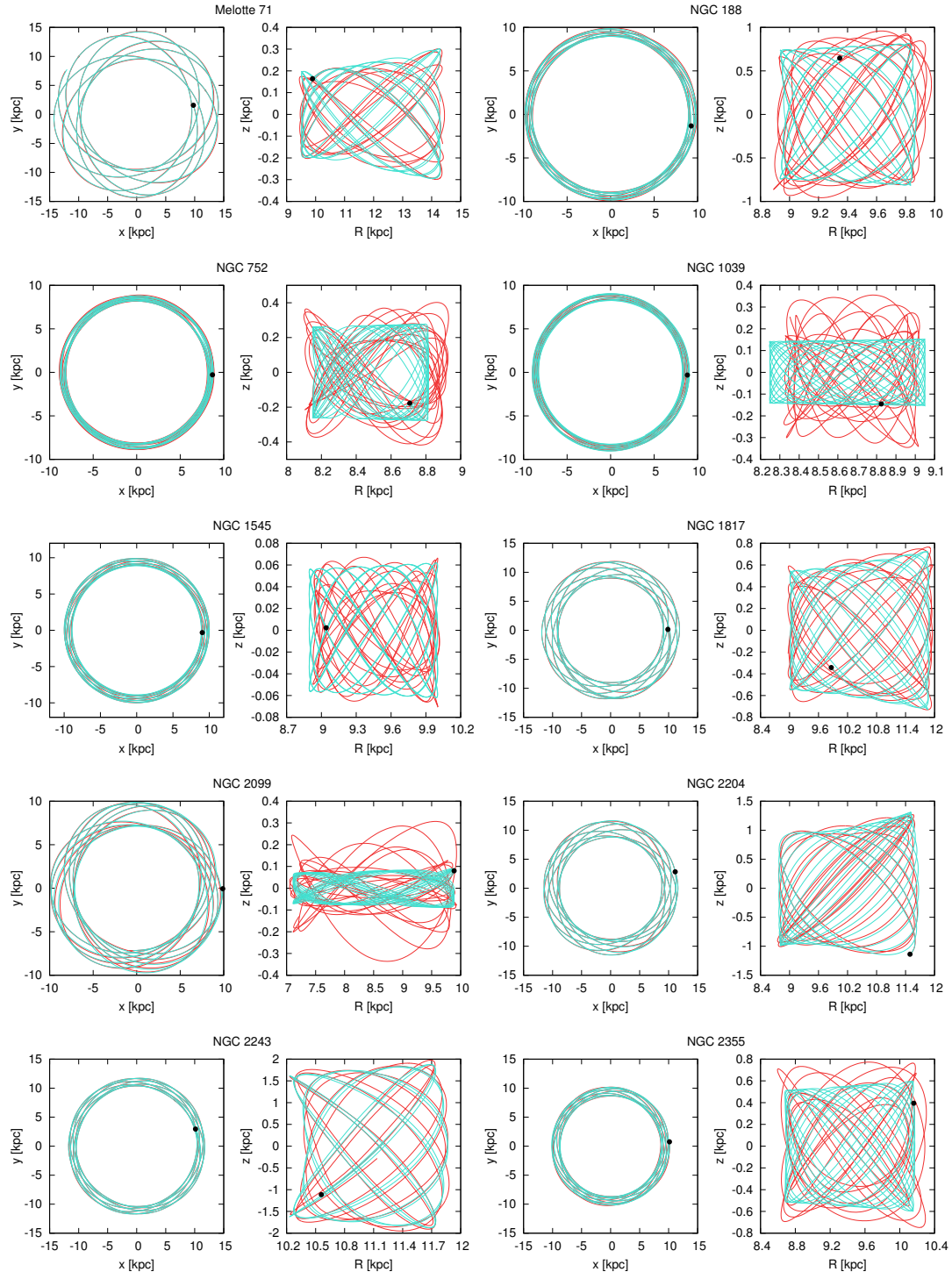

Figure D.1: Orbits of OCs from our sample – continued from previous page.

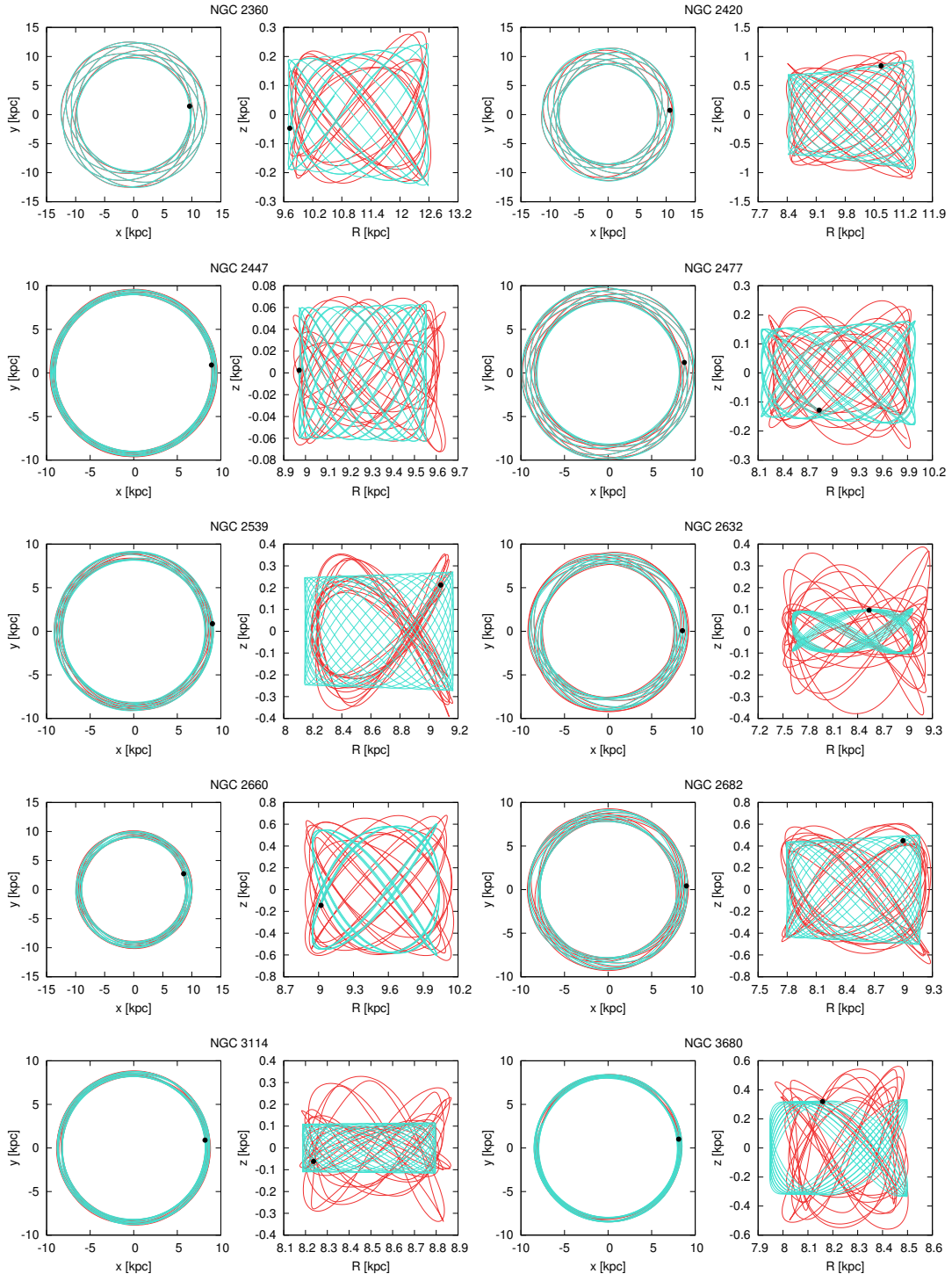

Figure D.1: Orbits of OCs from our sample – continued from previous page.

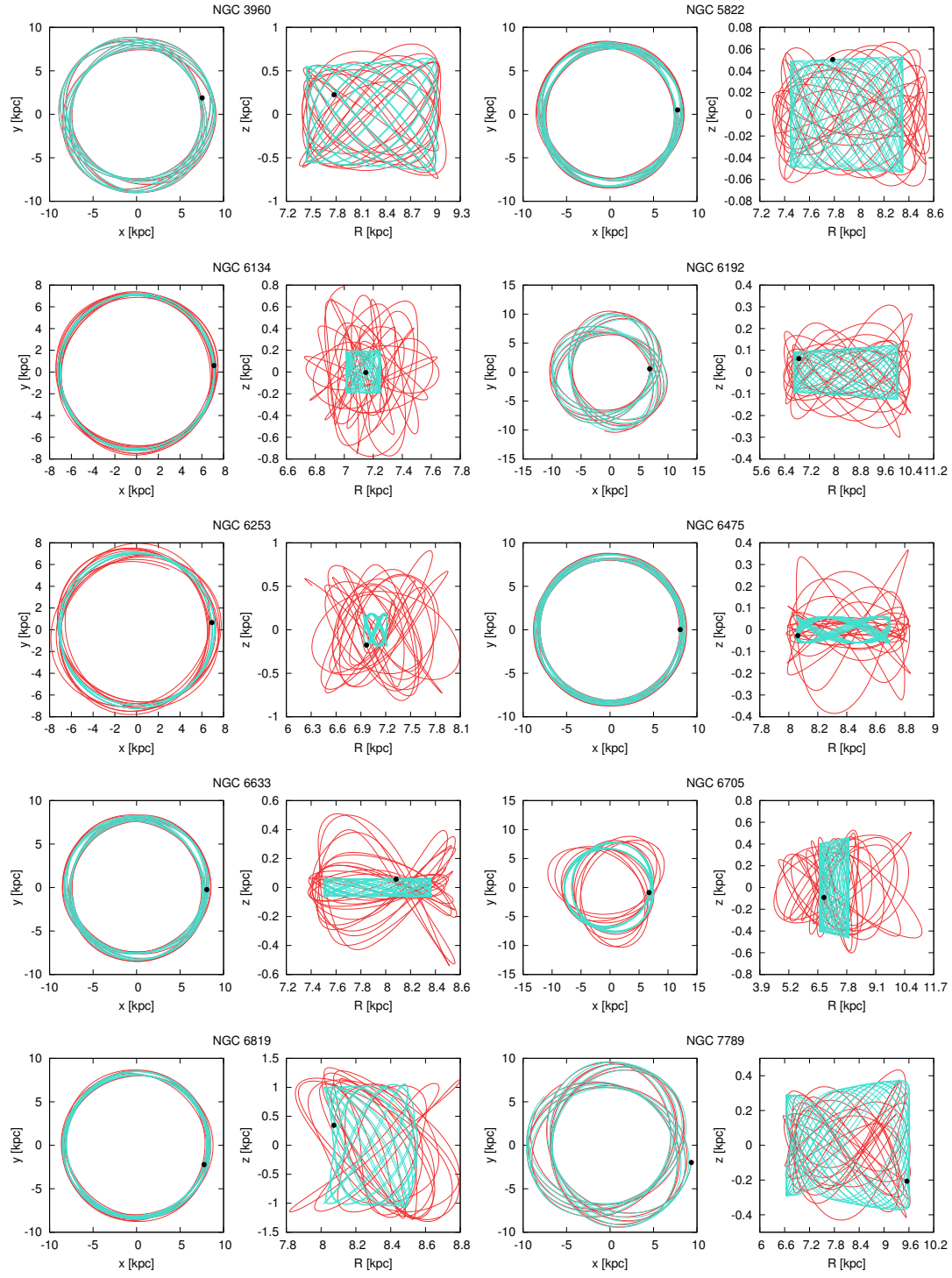

Figure D.1: Orbits of OCs from our sample – continued from previous page.

Bibliography

Allen, C. & Martos, M. A. 1988, Rev. Mexicana Astron. Astrofis., 16, 25

Allen, C., Moreno, E., & Pichardo, B. 2006, ApJ, 652, 1150

—. 2008, ApJ, 674, 237

Allen, C. & Santillan, A. 1991, Revista Mexicana de Astronomia y Astrofisica, 22, 255

Amôres, E. B., Lépine, J. R. D., & Mishurov, Y. N. 2009, MNRAS, 400, 1768

Andreuzzi, G., Bragaglia, A., Tosi, M., & Marconi, G. 2011, MNRAS, 412, 1265

Anthony-Twarog, B. J., Deliyannis, C. P., Twarog, B. A., Croxall, K. V., & Cummings, J. D. 2009, AJ, 138, 1171

Anthony-Twarog, B. J., Deliyannis, C. P., Twarog, B. A., Cummings, J. D., & Maderak, R. M. 2010, AJ, 139, 2034

Anthony-Twarog, B. J. & Twarog, B. A. 1985, ApJ, 291, 595

Anthony-Twarog, B. J., Twarog, B. A., & Mayer, L. 2007, AJ, 133, 1585

Antoja, T., Figueras, F., Romero-Gómez, M., Pichardo, B., Valenzuela, O., & Moreno, E. 2011, MNRAS, 418, 1423

Antoja, T., Valenzuela, O., Pichardo, B., Moreno, E., Figueras, F., & Fernández, D. 2009, ApJ, 700, L78

Athanassoula, E., Lambert, J. C., & Dehnen, W. 2005, MNRAS, 363, 496

Balaguer-Núñez, L., Galadí-Enríquez, D., & Jordi, C. 2007, A&A, 470, 585

Balaguer-Núñez, L., Jordi, C., & Galadí-Enríquez, D. 2005, A&A, 437, 457

Balaguer-Núñez, L., Jordi, C., Galadí-Enríquez, D., & Masana, E. 2004a, A&A, 426, 827

Balaguer-Núñez, L., Jordi, C., Galadí-Enríquez, D., & Zhao, J. L. 2004b, A&A, 426, 819

Basu, S., Grundahl, F., Stello, D., Kallinger, T., Hekker, S., Mosser, B., García, R. A., Mathur, S., Brogaard, K., Bruntt, H., Chaplin, W. J., Gai, N., Elsworth, Y., Esch, L., Ballot, J., Bedding, T. R., Gruberbauer, M., Huber, D., Miglio, A., Yildiz, M., Kjeldsen, H., Christensen-Dalsgaard, J., Gilliland, R. L., Fanelli, M. M., Ibrahim, K. A., & Smith, J. C. 2011, ApJ, 729, L10

Baumgardt, H., Dettbarn, C., & Wielen, R. 2000, A&AS, 146, 251

Baumgardt, H. & Makino, J. 2003, MNRAS, 340, 227

Becker, W. & Fenkart, R. B. in , IAU Symposium, Vol. 38, The Spiral Structure of our Galaxy, ed. W. BeckerG. I. Kontopoulos, 205

Bedin, L. R., King, I. R., Anderson, J., Piotto, G., Salaris, M., Cassisi, S., & Serenelli, A. 2008a, ApJ, 678, 1279

Bedin, L. R., Piotto, G., Anderson, J., Cassisi, S., King, I. R., Momany, Y., & Carraro, G. 2004, ApJ, 605, L125

Bedin, L. R., Piotto, G., Carraro, G., King, I. R., & Anderson, J. 2006, A&A, 460, L27

Bedin, L. R., Salaris, M., Piotto, G., Cassisi, S., Milone, A. P., Anderson, J., & King, I. R. 2008b, ApJ, 679, L29

Bedin, L. R., Salaris, M., Piotto, G., King, I. R., Anderson, J., Cassisi, S., & Momany, Y. 2005, ApJ, 624, L45

Bekki, K. 2011, MNRAS, 412, 2241

Bellini, A., Bedin, L. R., Pichardo, B., Moreno, E., Allen, C., Piotto, G., & Anderson, J. 2010a, A&A, 513, A51+

Bellini, A., Bedin, L. R., Piotto, G., Milone, A. P., Marino, A. F., & Villanova, S. 2010b, AJ, 140, 631

Bensby, T., Feltzing, S., Johnson, J. A., Gould, A., Adén, D., Asplund, M., Meléndez, J., Gal-Yam, A., Lucatello, S., Sana, H., Sumi, T., Miyake, N., Suzuki, D., Han, C., Bond, I., & Udalski, A. 2010, A&A, 512, A41+

Bica, E. & Bonatto, C. 2005, A&A, 431, 943

Binney, J. & Merrifield, M. 1998, Galactic Astronomy

Binney, J. & Tremaine, S. 2008, Galactic Dynamics: Second Edition (Princeton University Press)

Bird, J. C., Kazantzidis, S., & Weinberg, D. H. 2012, MNRAS, 420, 913

Block, D. L., Buta, R., Knapen, J. H., Elmegreen, D. M., Elmegreen, B. G., & Puerari, I. 2004, AJ, 128, 183

Boesgaard, A. M., Jensen, E. E. C., & Deliyannis, C. P. 2009, AJ, 137, 4949

Bonatto, C., Kerber, L. O., Bica, E., & Santiago, B. X. 2006, A&A, 446, 121

Bournaud, F. & Combes, F. 2002, A&A, 392, 83

Boutloukos, S. G. & Lamers, H. J. G. L. M. 2003, MNRAS, 338, 717

Bovy, J., Allende Prieto, C., Beers, T. C., Bizyaev, D., da Costa, L. N., Cunha, K., Ebelke, G. L., Eisenstein, D. J., Frinchaboy, P. M., García Pérez, A. E., Girardi, L., Hearty, F. R., Hogg, D. W., Holtzman, J., Maia, M. A. G., Majewski, S. R., Malanushenko, E., Malanushenko, V., Mészáros, S., Nidever, D. L., O'Connell, R. W., O'Donnell, C., Oravetz, A., Pan, K., Rocha-Pinto, H. J., Schiavon, R. P., Schneider, D. P., Schultheis, M., Skrutskie, M., Smith, V. V., Weinberg, D. H., Wilson, J. C., & Zasowski, G. 2012, ApJ, 759, 131

Bragaglia, A., Carretta, E., Gratton, R. G., Tosi, M., Bonanno, G., Bruno, P., Calì, A., Claudi, R., Cosentino, R., Desidera, S., Farisato, G., Rebeschini, M., & Scuderi, S. 2001, AJ, 121, 327

Bragaglia, A., Sestito, P., Villanova, S., Carretta, E., Randich, S., & Tosi, M. 2008, A&A, 480, 79

Bragaglia, A., Tosi, M., Carretta, E., Gratton, R. G., Marconi, G., & Pompei, E. 2006, MNRAS, 366, 1493

Brogaard, K., Bruntt, H., Grundahl, F., Clausen, J. V., Frandsen, S., Vandenberg, D. A., & Bedin, L. R. 2011, A&A, 525, A2+

Brogaard, K., VandenBerg, D. A., Bruntt, H., Grundahl, F., Frandsen, S., Bedin, L. R., Milone, A. P., Dotter, A., Feiden, G. A., Stetson, P. B., Sandquist, E., Miglio, A., Stello, D., & Jessen-Hansen, J. 2012, A&A, 543, A106

Brown, J. A., Wallerstein, G., Geisler, D., & Oke, J. B. 1996, AJ, 112, 1551

Bruntt, H., Frandsen, S., Kjeldsen, H., & Andersen, M. I. 1999, A&AS, 140, 135

Buson, L. M., Bertone, E., Buzzoni, A., & Carraro, G. 2006, Baltic Astronomy, 15, 49

Buta, R. & Block, D. L. 2001, ApJ, 550, 243

Buzzoni, A., Bertone, E., Carraro, G., & Buson, L. 2012, ApJ, 749, 35

Cabrera-Cano, J. & Alfaro, E. J. 1990, A&A, 235, 94

Cameron, L. M. 1985, A&A, 147, 47

Cargile, P. A., James, D. J., & Jeffries, R. D. 2010, ApJ, 725, L111

Carlin, J. L., Majewski, S. R., Casetti-Dinescu, D. I., Law, D. R., Girard, T. M., & Patterson, R. J. 2012, ApJ, 744, 25

Carney, B. W., Lee, J.-W., & Dodson, B. 2005, AJ, 129, 656

Carraro, G., Anthony-Twarog, B. J., Costa, E., Jones, B. J., & Twarog, B. A. 2011, AJ, 142, 127

Carraro, G., Bresolin, F., Villanova, S., Matteucci, F., Patat, F., & Romaniello, M. 2004, AJ, 128, 1676

Carraro, G. & Chiosi, C. 1994, A&A, 288, 751

Carraro, G., Chiosi, C., Bressan, A., & Bertelli, G. 1994, A&AS, 103, 375

Carraro, G., Geisler, D., Villanova, S., Frinchaboy, P. M., & Majewski, S. R. 2007, A&A, 476, 217

Carraro, G., Ng, Y. K., & Portinari, L. 1998, MNRAS, 296, 1045

Carraro, G. & Patat, F. 2001, A&A, 379, 136

Carraro, G., Villanova, S., Demarque, P., McSwain, M. V., Piotto, G., & Bedin, L. R. 2006, ApJ, 643, 1151

Carrera, R. & Pancino, E. 2011, A&A, 535, A30

Carretta, E., Bragaglia, A., Gratton, R. G., Lucatello, S., Catanzaro, G., Leone, F., Bellazzini, M., Claudi, R., D'Orazi, V., Momany, Y., Ortolani, S., Pancino, E., Piotto, G., Recio-Blanco, A., & Sabbi, E. 2009, A&A, 505, 117

Carretta, E., Bragaglia, A., Gratton, R. G., & Tosi, M. 2004, A&A, 422, 951

Chaboyer, B., Green, E. M., & Liebert, J. 1999, AJ, 117, 1360

Chen, B. 1996, A&AS, 118, 181

Chen, B., Carraro, G., Torra, J., & Jordi, C. 1998, A&A, 331, 916

Chen, L., Hou, J. L., & Wang, J. J. 2003, AJ, 125, 1397

Chen, W. P., Chen, C. W., & Shu, C. G. 2004, AJ, 128, 2306

Chiappini, C., Matteucci, F., & Gratton, R. 1997, ApJ, 477, 765

Chiappini, C., Matteucci, F., & Romano, D. 2001, ApJ, 554, 1044

Choo, K. J., Kim, S.-L., Yoon, T. S., Chun, M.-Y., Sung, H., Park, B.-G., Ann, H. B., Lee, M. G., Jeon, Y.-B., & Yuk, I.-S. 2003, A&A, 399, 99

Churchwell, E., Babler, B. L., Meade, M. R., Whitney, B. A., Benjamin, R., Indebetouw, R., Cyganowski, C., Robitaille, T. P., Povich, M., Watson, C., & Bracker, S. 2009, PASP, 121, 213

Coşkunoğlu, B., Ak, S., Bilir, S., Karaali, S., Yaz, E., Gilmore, G., Seabroke, G. M., Bienaymé, O., Bland-Hawthorn, J., Campbell, R., Freeman, K. C., Gibson, B., Grebel, E. K., Munari, U., Navarro, J. F., Parker, Q. A., Siebert, A., Siviero, A., Steinmetz, M., Watson, F. G., Wyse, R. F. G., & Zwitter, T. 2011, MNRAS, 412, 1237

Cohen, J. G. 1978, ApJ, 223, 487

Combes, F. 2008, ArXiv e-prints: 0811.0153

Combes, F. & Sanders, R. H. 1981, A&A, 96, 164

Cox, D. P. & Gómez, G. C. 2002, ApJS, 142, 261

Daniel, S. A., Latham, D. W., Mathieu, R. D., & Twarog, B. A. 1994, PASP, 106, 281

D'Cruz, N. L., Dorman, B., Rood, R. T., & O'Connell, R. W. 1996, ApJ, 466, 359

de Bruijne, J. H. J. 2012, Ap&SS, 341, 31

de Silva, G. M., Gibson, B. K., Lattanzio, J., & Asplund, M. 2009, A&A, 500, L25

de Zeeuw, T. & Pfenniger, D. 1988, MNRAS, 235, 949

Debattista, V. P., Mayer, L., Carollo, C. M., Moore, B., Wadsley, J., & Quinn, T. 2006, ApJ, 645, 209

Dehnen, W. 2000, AJ, 119, 800

Dehnen, W. & Binney, J. J. 1998, MNRAS, 298, 387

Demarque, P., Green, E. M., & Guenther, D. B. 1992, AJ, 103, 151

D'Ercole, A., Vesperini, E., D'Antona, F., McMillan, S. L. W., & Recchi, S. 2008, MNRAS, 391, 825

Dias, W. S., Alessi, B. S., Moitinho, A., & Lépine, J. R. D. 2002a, A&A, 389, 871

Dias, W. S., Assafin, M., Flório, V., Alessi, B. S., & Líbero, V. 2006, A&A, 446, 949

Dias, W. S. & Lépine, J. R. D. 2005, ApJ, 629, 825

Dias, W. S., Lépine, J. R. D., & Alessi, B. S. 2001, A&A, 376, 441

—. 2002b, A&A, 388, 168

Dinescu, D. I., Girard, T. M., & van Altena, W. F. 1999, AJ, 117, 1792

Dobbie, P. D., Lodieu, N., & Sharp, R. G. 2010, MNRAS, 409, 1002

Drimmel, R. 2000, A&A, 358, L13

Drimmel, R. & Spergel, D. N. 2001, ApJ, 556, 181

Edvardsson, B., Andersen, J., Gustafsson, B., Lambert, D. L., Nissen, P. E., & Tomkin, J. 1993, A&A, 275, 101

Fellhauer, M., Belokurov, V., Evans, N. W., Wilkinson, M. I., Zucker, D. B., Gilmore, G., Irwin, M. J., Bramich, D. M., Vidrih, S., Wyse, R. F. G., Beers, T. C., & Brinkmann, J. 2006, ApJ, 651, 167

Finlay, J., Noriega-Crespo, A., Friel, E. D., & Cudworth, K. M. 1995, in Bulletin of the American Astronomical Society, Vol. 27, American Astronomical Society Meeting Abstracts, 107.02

Flynn, C., Sommer-Larsen, J., & Christensen, P. R. 1996, MNRAS, 281, 1027

Ford, A., Jeffries, R. D., & Smalley, B. 2005, MNRAS, 364, 272

Foyle, K., Rix, H.-W., Dobbs, C. L., Leroy, A. K., & Walter, F. 2011, ApJ, 735, 101

Freeman, K. C. 1970, ApJ, 160, 811

Friel, E. D. 1995, ARA&A, 33, 381

Friel, E. D., Jacobson, H. R., & Pilachowski, C. A. 2005, AJ, 129, 2725

—. 2010, AJ, 139, 1942

Friel, E. D. & Janes, K. A. 1993, A&A, 267, 75

Friel, E. D., Janes, K. A., Tavarez, M., Scott, J., Katsanis, R., Lotz, J., Hong, L., & Miller, N. 2002, AJ, 124, 2693

Frinchaboy, P. M. & Majewski, S. R. 2008, AJ, 136, 118

Fujii, M. S. & Baba, J. 2012, MNRAS, 427, L16

Fux, R. 1997, A&A, 327, 983

—. 1999, A&A, 345, 787

Galadí-Enríquez, D., Jordi, C., & Trullols, E. 1998, A&A, 337, 125

García-Berro, E., Torres, S., Althaus, L. G., Renedo, I., Lorén-Aguilar, P., Córsico, A. H., Rohrmann, R. D., Salaris, M., & Isern, J. 2010, Nature, 465, 194

García-Berro, E., Torres, S., Renedo, I., Camacho, J., Althaus, L. G., Córsico, A. H., Salaris, M., & Isern, J. 2011, A&A, 533, A31

Gardner, E. & Flynn, C. 2010, MNRAS, 405, 545

Geisler, D., Villanova, S., Carraro, G., Pilachowski, C., Cummings, J., Johnson, C. I., & Bresolin, F. 2012, ApJ, 756, L40

Geller, A. M., Mathieu, R. D., Harris, H. C., & McClure, R. D. 2008, AJ, 135, 2264

Gerhard, O. 2011, Memorie della Societa Astronomica Italiana Supplementi, 18, 185

Gieles, M., Athanassoula, E., & Portegies Zwart, S. F. 2007, MNRAS, 376, 809

Gieles, M., Baumgardt, H., Bastian, N., & Lamers, H. J. G. L. M. Astronomical Society of the Pacific Conference Series, Vol. 322, , The Formation and Evolution of Massive Young Star Clusters, ed. H. J. G. L. M. LamersL. J. Smith & A. Nota, 481

Gieles, M., Portegies Zwart, S. F., Baumgardt, H., Athanassoula, E., Lamers, H. J. G. L. M., Sipior, M., & Leenaarts, J. 2006, MNRAS, 371, 793

Gilliland, R. L., Brown, T. M., Christensen-Dalsgaard, J., Kjeldsen, H., Aerts, C., Appourchaux, T., Basu, S., Bedding, T. R., Chaplin, W. J., Cunha, M. S., De Cat, P., De Ridder, J., Guzik, J. A., Handler, G., Kawaler, S., Kiss, L., Kolenberg, K., Kurtz, D. W., Metcalfe, T. S., Monteiro, M. J. P. F. G., Szabó, R., Arentoft, T., Balona, L., Debosscher, J., Elsworth, Y. P., Quirion, P.-O., Stello, D., Suárez, J. C., Borucki, W. J., Jenkins, J. M., Koch, D., Kondo, Y., Latham, D. W., Rowe, J. F., & Steffen, J. H. 2010, PASP, 122, 131

Gilmore, G. & Reid, N. 1983, MNRAS, 202, 1025

Gim, M., Vandenberg, D. A., Stetson, P. B., Hesser, J. E., & Zurek, D. R. 1998, PASP, 110, 1318

Glebbeek, E., Sills, A., & Leigh, N. 2010, MNRAS, 408, 1267

Gonzalez, G. & Wallerstein, G. 2000, PASP, 112, 1081

González, J. F. & Lapasset, E. 2001, AJ, 121, 2657

Gratton, R., Bragaglia, A., Carretta, E., & Tosi, M. 2006, ApJ, 642, 462

Gratton, R., Sneden, C., & Carretta, E. 2004, ARA&A, 42, 385

Gratton, R. G., Bonifacio, P., Bragaglia, A., Carretta, E., Castellani, V., Centurion, M., Chieffi, A., Claudi, R., Clementini, G., D'Antona, F., Desidera, S., François, P., Grundahl, F., Lucatello, S., Molaro, P., Pasquini, L., Sneden, C., Spite, F., & Straniero, O. 2001, A&A, 369, 87

Gratton, R. G., Carretta, E., & Bragaglia, A. 2012, A&A Rev., 20, 50

Grosbol, P., Carraro, G., & Beletski, Y. 2011, The Messenger, 03, 47

Grundahl, F., Clausen, J. V., Hardis, S., & Frandsen, S. 2008, A&A, 492, 171

Güneş, O., Karataş, Y., & Bonatto, C. 2012, New A, 17, 720

Hansen, B. M. S. 2005, ApJ, 635, 522

Harris, W. E. 1996, AJ, 112, 1487

Hartman, J. D., Gaudi, B. S., Holman, M. J., McLeod, B. A., Stanek, K. Z., Barranco, J. A., Pinsonneault, M. H., Meibom, S., & Kalirai, J. S. 2008, ApJ, 675, 1233

Heber, U. 2009, ARA&A, 47, 211

Hole, K. T., Geller, A. M., Mathieu, R. D., Platais, I., Meibom, S., & Latham, D. W. 2009, AJ, 138, 159

Hron, J. 1987, A&A, 176, 34

Jacobson, H. R., Friel, E. D., & Pilachowski, C. A. 2008, AJ, 135, 2341

—. 2009, AJ, 137, 4753

—. 2011a, AJ, 141, 58

Jacobson, H. R., Pilachowski, C. A., & Friel, E. D. 2011b, AJ, 142, 59

Janes, K. & Adler, D. 1982, ApJS, 49, 425

Janes, K. A. 1979, ApJS, 39, 135

—. 1984, PASP, 96, 977

Janes, K. A., Tilley, C., & Lynga, G. 1988, AJ, 95, 771

Jeffries, R. D., Totten, E. J., Harmer, S., & Deliyannis, C. P. 2002, MNRAS, 336, 1109

Jílková, L., Carraro, G., Jungwiert, B., & Minchev, I. 2012, A&A, 541, A64

Johnson, D. R. H. & Soderblom, D. R. 1987, AJ, 93, 864

Jones, B. F. & Prosser, C. F. 1996, AJ, 111, 1193

Jurić, M., Ivezić, Ž., Brooks, A., Lupton, R. H., Schlegel, D., Finkbeiner, D., Padmanabhan, N., Bond, N., Sesar, B., Rockosi, C. M., Knapp, G. R., Gunn, J. E., Sumi, T., Schneider, D. P., Barentine, J. C., Brewington, H. J., Brinkmann, J., Fukugita, M., Harvanek, M., Kleinman, S. J., Krzesinski, J., Long, D., Neilsen, Jr., E. H., Nitta, A., Snedden, S. A., & York, D. G. 2008, ApJ, 673, 864

Kalirai, J. S., Bergeron, P., Hansen, B. M. S., Kelson, D. D., Reitzel, D. B., Rich, R. M., & Richer, H. B. 2007, ApJ, 671, 748

Kaluzny, J. 1990, MNRAS, 243, 492

Kaluzny, J. & Rucinski, S. M. 1995, A&AS, 114, 1

Kaluzny, J. & Udalski, A. 1992, Acta Astron., 42, 29

Kassis, M., Janes, K. A., Friel, E. D., & Phelps, R. L. 1997, AJ, 113, 1723

Keenan, D. W. & Innanen, K. A. 1974, ApJ, 189, 205

Keenan, D. W., Innanen, K. A., & House, F. C. 1973, AJ, 78, 173

Kharchenko, N. V., Berczik, P., Petrov, M. I., Piskunov, A. E., Röser, S., Schilbach, E., & Scholz, R.-D. 2009, A&A, 495, 807

Kharchenko, N. V., Piskunov, A. E., Röser, S., Schilbach, E., & Scholz, R.-D. 2005a, A&A, 438, 1163

—. 2005b, A&A, 440, 403

Kharchenko, N. V., Scholz, R.-D., Piskunov, A. E., Röser, S., & Schilbach, E. 2007, Astronomische Nachrichten, 328, 889

King, I. R. 1966, AJ, 71, 64

King, I. R., Bedin, L. R., Piotto, G., Cassisi, S., & Anderson, J. 2005, AJ, 130, 626

Kinman, T. D. 1965, ApJ, 142, 655

Krone-Martins, A., Soubiran, C., Ducourant, C., Teixeira, R., & Le Campion, J. F. 2010, A&A, 516, A3

Kruijssen, J. M. D. & Mieske, S. 2009, A&A, 500, 785

Kruijssen, J. M. D., Pelupessy, F. I., Lamers, H. J. G. L. M., Portegies Zwart, S. F., & Icke, V. 2011, MNRAS, 414, 1339

Lada, C. J. & Lada, E. A. 2003, ARA&A, 41, 57

Lamers, H. J. G. L. M., Baumgardt, H., & Gieles, M. 2010, MNRAS, 409, 305

Lamers, H. J. G. L. M. & Gieles, M. 2006, A&A, 455, L17

Lamers, H. J. G. L. M., Gieles, M., Bastian, N., Baumgardt, H., Kharchenko, N. V., & Portegies Zwart, S. 2005, A&A, 441, 117

Lépine, J. R. D., Acharova, I. A., & Mishurov, Y. N. 2003, ApJ, 589, 210

Lépine, J. R. D., Cruz, P., Scarano, Jr., S., Barros, D. A., Dias, W. S., Pompéia, L., Andrievsky, S. M., Carraro, G., & Famaey, B. 2011, MNRAS, 417, 698

Lépine, J. R. D., Dias, W. S., & Mishurov, Y. 2008, MNRAS, 386, 2081

Liebert, J., Saffer, R. A., & Green, E. M. 1994, AJ, 107, 1408

Loktin, A. V. & Beshenov, G. V. 2003, Astronomy Reports, 47, 6

Loktin, A. V., Gerasimenko, T. P., & Malysheva, L. K. 2001, Astronomical and Astrophysical Transactions, 20, 607

Luck, R. E. & Lambert, D. L. 2011, AJ, 142, 136

Lyngå, G. 1982, A&A, 109, 213

—. 1987, CDS Strasbourg (VII/92A)

Lyngå, G. & Palouš, J. 1987, A&A, 188, 35

Magrini, L., Randich, S., Zoccali, M., Jilkova, L., Carraro, G., Galli, D., Maiorca, E., & Busso, M. 2010, A&A, 523, A11

Magrini, L., Sestito, P., Randich, S., & Galli, D. 2009, A&A, 494, 95

Matteucci, F. & Francois, P. 1989, MNRAS, 239, 885

Maxted, P. f. L., Heber, U., Marsh, T. R., & North, R. C. 2001, MNRAS, 326, 1391

Meibom, S., Andersen, J., & Nordström, B. 2002, A&A, 386, 187

Meibom, S., Mathieu, R. D., Stassun, K. G., Liebesny, P., & Saar, S. H. 2011, ApJ, 733, 115

Mermilliod, J. C., Mayor, M., & Udry, S. 2008a, A&A, 485, 303

Mermilliod, J.-C., Mayor, M., & Udry, S. 2009, A&A, 498, 949

Mermilliod, J.-C., Platais, I., James, D. J., Grenon, M., & Cargile, P. A. 2008b, A&A, 485, 95

Meynet, G., Mermilliod, J.-C., & Maeder, A. 1993, A&AS, 98, 477

Miglio, A., Brogaard, K., Stello, D., Chaplin, W. J., D'Antona, F., Montalbán, J., Basu, S., Bressan, A., Grundahl, F., Pinsonneault, M., Serenelli, A. M., Elsworth, Y., Hekker, S., Kallinger, T., Mosser, B., Ventura, P., Bonanno, A., Noels, A., Silva Aguirre, V., Szabo, R., Li, J., McCauliff, S., Middour, C. K., & Kjeldsen, H. 2012, MNRAS, 419, 2077

Milone, A. P., Bedin, L. R., Piotto, G., & Anderson, J. 2009, A&A, 497, 755

Minchev, I. & Famaey, B. 2010, ApJ, 722, 112

Minchev, I., Famaey, B., Combes, F., Di Matteo, P., Mouhcine, M., & Wozniak, H. 2011, A&A, 527, A147+

Minchev, I. & Quillen, A. C. 2006, MNRAS, 368, 623

Miyamoto, M. & Nagai, R. 1975, PASJ, 27, 533

Moitinho, A. in , IAU Symposium, Vol. 266, IAU Symposium, ed. R. de GrijsJ. R. D. Lépine, 106–116

Montalto, M., Piotto, G., Desidera, S., Platais, I., Carraro, G., Momany, Y., de Marchi, F., & Recio-Blanco, A. 2009, A&A, 505, 1129

Montgomery, K. A., Janes, K. A., & Phelps, R. L. 1994, AJ, 108, 585

Nilakshi, Sagar, R., Pandey, A. K., & Mohan, V. 2002, A&A, 383, 153

Origlia, L., Valenti, E., Rich, R. M., & Ferraro, F. R. 2006, ApJ, 646, 499

Palouš, J., Ruprecht, J., Dluzhnevskaia, O. B., & Piskunov, A. 1977, A&A, 61, 27

Panagia, N. & Tosi, M. 1981, A&A, 96, 306

Pancino, E., Carrera, R., Rossetti, E., & Gallart, C. 2010, A&A, 511, A56

Pedicelli, S., Bono, G., Lemasle, B., François, P., Groenewegen, M., Lub, J., Pel, J. W., Laney, D., Piersimoni, A., Romaniello, M., Buonanno, R., Caputo, F., Cassisi, S., Castelli, F., Leurini, S., Pietrinferni, A., Primas, F., & Pritchard, J. 2009, A&A, 504, 81

Perryman, M. A. C. & ESA, eds. 1997, ESA Special Publication, Vol. 1200, The HIPPARCOS and TYCHO catalogues. Astrometric and photometric star catalogues derived from the ESA HIPPARCOS Space Astrometry Mission

Pfenniger, D. 1984, A&A, 134, 373

Piatti, A. E., Claria, J. J., & Abadi, M. G. 1995, AJ, 110, 2813

Pichardo, B., Martos, M., & Moreno, E. 2004, ApJ, 609, 144

Pichardo, B., Martos, M., Moreno, E., & Espresate, J. 2003, ApJ, 582, 230

Pichardo, B., Moreno, E., Allen, C., Bedin, L. R., Bellini, A., & Pasquini, L. 2012, AJ, 143, 73

Pietrukowicz, P., Kaluzny, J., & Krzeminski, W. 2006, MNRAS, 365, 110

Piotto, G., Villanova, S., Bedin, L. R., Gratton, R., Cassisi, S., Momany, Y., Recio-Blanco, A., Lucatello, S., Anderson, J., King, I. R., Pietrinferni, A., & Carraro, G. 2005, ApJ, 621, 777

Piskunov, A. E., Kharchenko, N. V., Röser, S., Schilbach, E., & Scholz, R.-D. 2006, A&A, 445, 545

Platais, I., Cudworth, K. M., Kozhurina-Platais, V., McLaughlin, D. E., Meibom, S., & Veillet, C. 2011, ApJ, 733, L1

Platais, I., Kozhurina-Platais, V., Mathieu, R. D., Girard, T. M., & van Altena, W. F. 2003, AJ, 126, 2922

Plummer, H. C. 1911, MNRAS, 71, 460

Portegies Zwart, S. F., McMillan, S. L. W., Hut, P., & Makino, J. 2001, MNRAS, 321, 199

Press, W. H., Teukolsky, S. A., Vetterling, W. T., & Flannery, B. P. 1992, Numerical recipes in FORTRAN. The art of scientific computing (Cambridge: University Press)

Quillen, A. C. 2003, AJ, 125, 785

Quillen, A. C., Minchev, I., Bland-Hawthorn, J., & Haywood, M. 2009, MNRAS, 397, 1599

Radburn-Smith, D. J., Roškar, R., Debattista, V. P., Dalcanton, J. J., Streich, D., de Jong, R. S., Vlajić, M., Holwerda, B. W., Purcell, C. W., Dolphin, A. E., & Zucker, D. B. 2012, ApJ, 753, 138

Randich, S., Pallavicini, R., Meola, G., Stauffer, J. R., & Balachandran, S. C. 2001, A&A, 372, 862

Randich, S., Sestito, P., Primas, F., Pallavicini, R., & Pasquini, L. 2006, A&A, 450, 557

Rasmussen, M. B., Bruntt, H., Frandsen, S., Paunzen, E., & Maitzen, H. M. 2002, A&A, 390, 109

Reddy, A. B. S., Giridhar, S., & Lambert, D. L. 2012, MNRAS, 419, 1350

Reddy, B. E., Lambert, D. L., & Allende Prieto, C. 2006, MNRAS, 367, 1329

Reddy, B. E., Tomkin, J., Lambert, D. L., & Allende Prieto, C. 2003, MNRAS, 340, 304

Reid, M. J. & Brunthaler, A. 2004, ApJ, 616, 872

Reid, M. J., Menten, K. M., Zheng, X. W., Brunthaler, A., Moscadelli, L., Xu, Y., Zhang, B., Sato, M., Honma, M., Hirota, T., Hachisuka, K., Choi, Y. K., Moellenbrock, G. A., & Bartkiewicz, A. 2009, ApJ, 700, 137

Renzini, A. 2008, MNRAS, 391, 354

Roediger, J. C., Courteau, S., Sánchez-Blázquez, P., & McDonald, M. 2012, ApJ, 758, 41

Roškar, R., Debattista, V. P., Stinson, G. S., Quinn, T. R., Kaufmann, T., & Wadsley, J. 2008a, ApJ, 675, L65

Roškar, R., Debattista, V. P., Quinn, T. R., Stinson, G. S., & Wadsley, J. 2008b, ApJ, 684, L79

Salaris, M., Weiss, A., & Percival, S. M. 2004, A&A, 414, 163

Sanders, W. L. 1971, A&A, 14, 226

Sandrelli, S., Bragaglia, A., Tosi, M., & Marconi, G. 1999, MNRAS, 309, 739

Santos, Jr., J. F. C., Bonatto, C., & Bica, E. 2005, A&A, 442, 201

Santos, N. C., Lovis, C., Melendez, J., Montalto, M., Naef, D., & Pace, G. 2012, A&A, 538, A151

Santos, N. C., Lovis, C., Pace, G., Melendez, J., & Naef, D. 2009, A&A, 493, 309

Sarajedini, A., Brandt, K., Grocholski, A. J., & Tiede, G. P. 2004, AJ, 127, 991

Sarajedini, A., von Hippel, T., Kozhurina-Platais, V., & Demarque, P. 1999, AJ, 118, 2894

Schönrich, R. & Binney, J. 2009, MNRAS, 396, 203

Schönrich, R., Binney, J., & Dehnen, W. 2010, MNRAS, 403, 1829

Schuler, S. C., King, J. R., Fischer, D. A., Soderblom, D. R., & Jones, B. F. 2003, AJ, 125, 2085

Scott, J. E., Friel, E. D., & Janes, K. A. 1995, AJ, 109, 1706

Sellwood, J. A. & Binney, J. J. 2002, MNRAS, 336, 785

Sestito, P., Bragaglia, A., Randich, S., Carretta, E., Prisinzano, L., & Tosi, M. 2006, A&A, 458, 121

Sestito, P., Bragaglia, A., Randich, S., Pallavicini, R., Andrievsky, S. M., & Korotin, S. A. 2008, A&A, 488, 943

Sestito, P., Randich, S., & Bragaglia, A. 2007, A&A, 465, 185

Sestito, P., Randich, S., Mermilliod, J.-C., & Pallavicini, R. 2003, A&A, 407, 289

Sestito, P., Randich, S., & Pallavicini, R. 2004, A&A, 426, 809

Sharma, S., Pandey, A. K., Ogura, K., Mito, H., Tarusawa, K., & Sagar, R. 2006, AJ, 132, 1669

Silverman, B. W. 1986, Density estimation for statistics and data analysis

Skrutskie, M. F., Cutri, R. M., Stiening, R., Weinberg, M. D., Schneider, S., Carpenter, J. M., Beichman, C., Capps, R., Chester, T., Elias, J., Huchra, J., Liebert, J., Lonsdale, C., Monet, D. G., Price, S., Seitzer, P., Jarrett, T., Kirkpatrick, J. D., Gizis, J. E., Howard, E., Evans, T., Fowler, J., Fullmer, L., Hurt, R., Light, R., Kopan, E. L., Marsh, K. A., McCallon, H. L., Tam, R., Van Dyk, S., & Wheelock, S. 2006, AJ, 131, 1163

Soubiran, C., Odenkirchen, M., & Le Campion, J.-F. 2000, A&A, 357, 484

Sousa, S. G., Santos, N. C., Mayor, M., Udry, S., Casagrande, L., Israelian, G., Pepe, F., Queloz, D., & Monteiro, M. J. P. F. G. 2008, A&A, 487, 373

Spitzer, Jr., L. 1958, ApJ, 127, 17

Stetson, P. B. 1980, AJ, 85, 387

Stetson, P. B., Bruntt, H., & Grundahl, F. 2003, PASP, 115, 413

Taylor, B. J. 2001, A&A, 377, 473

Tripicco, M. J., Bell, R. A., Dorman, B., & Hufnagel, B. 1995, AJ, 109, 1697

Turon, C., Primas, F., Binney, J., Chiappini, C., Drew, J., Helmi, A., Robin, A., & Ryan, S. G. 2008, The Messenger, 134, 46

Twarog, B. A., Anthony-Twarog, B. J., & De Lee, N. 2003, AJ, 125, 1383

Twarog, B. A., Ashman, K. M., & Anthony-Twarog, B. J. 1997, AJ, 114, 2556

Twarog, B. A., Carraro, G., & Anthony-Twarog, B. J. 2011, ApJ, 727, L7+

Twarog, B. A., Corder, S., & Anthony-Twarog, B. J. 2006, AJ, 132, 299

Valcarce, A. A. R. & Catelan, M. 2011, A&A, 533, A120

Vallée, J. P. 2005, AJ, 130, 569

—. 2008, AJ, 135, 1301

van Leeuwen, F. 2009, A&A, 497, 209

Van Loon, J. T., Boyer, M. L., & McDonald, I. 2008, ApJ, 680, L49

Vande Putte, D., Garnier, T. P., Ferreras, I., Mignani, R. P., & Cropper, M. 2010, MNRAS, 407, 2109

Vasilevskis, S., Klemola, A., & Preston, G. 1958, AJ, 63, 387

Vesperini, E., McMillan, S. L. W., D'Antona, F., & D'Ercole, A. 2010, ApJ, 718, L112

Villanova, S., Carraro, G., Bresolin, F., & Patat, F. 2005, AJ, 130, 652

Villanova, S., Carraro, G., & Saviane, I. 2009, A&A, 504, 845

Villanova, S., Piotto, G., King, I. R., Anderson, J., Bedin, L. R., Gratton, R. G., Cassisi, S., Momany, Y., Bellini, A., Cool, A. M., Recio-Blanco, A., & Renzini, A. 2007, ApJ, 663, 296

Wielen, R. 1971, A&A, 13, 309

—. 1974, Highlights of Astronomy, 3, 395

—. 1977, A&A, 60, 263

Wielen, R., Fuchs, B., & Dettbarn, C. 1996, A&A, 314, 438

Williams, K. A. & Bolte, M. 2007, AJ, 133, 1490

Worthey, G. & Jowett, K. J. 2003, PASP, 115, 96

Wu, Z., Zhou, X., Ma, J., & Du, C. 2009, MNRAS, 399, 2146

Yadav, R. K. S., Bedin, L. R., Piotto, G., Anderson, J., Cassisi, S., Villanova, S., Platais, I., Pasquini, L., Momany, Y., & Sagar, R. 2008, A&A, 484, 609

Yoachim, P., Roškar, R., & Debattista, V. P. 2012, ApJ, 752, 97

Yong, D., Carney, B. W., & Friel, E. D. 2012, AJ, 144, 95

Yong, D., Carney, B. W., & Teixera de Almeida, M. L. 2005, AJ, 130, 597

Zacharias, N., Finch, C., Girard, T., Hambly, N., Wycoff, G., Zacharias, M. I., Castillo, D., Corbin, T., DiVittorio, M., Dutta, S., Gaume, R., Gauss, S., Germain, M., Hall, D., Hartkopf, W., Hsu, D., Holdenried, E., Makarov, V., Martinez, M., Mason, B., Monet, D., Rafferty, T., Rhodes, A., Siemers, T., Smith, D., Tilleman, T., Urban, S., Wieder, G., Winter, L., & Young, A. 2010, AJ, 139, 2184

Zacharias, N., Finch, C., Girard, T., Henden, A., Bartlett, J., Monet, D., & Zacharias, M. 2012a, ArXiv e-prints

Zacharias, N., Finch, C. T., Girard, T. M., Henden, A., Bartlett, J. L., Monet, D. G., & Zacharias, M. I. 2012b, VizieR Online Data Catalog, 1322, 0

Zacharias, N., Urban, S. E., Zacharias, M. I., Wycoff, G. L., Hall, D. M., Monet, D. G., & Rafferty, T. J. 2004, AJ, 127, 3043

Začs, L., Alksnis, O., Barzdis, A., Laure, A., Musaev, F. A., Bondar, A., & Sperauskas, J. 2011, MNRAS, 417, 649

Zhao, J. L. & He, Y. P. 1990, A&A, 237, 54

Zhu, Z. 2009, Research in Astronomy and Astrophysics, 9, 1285

Appendix E

List of publications

Refereed publications

Casetti-Dinescu, D. I., Girard, T. M., **Jílková**, **L.**, van Altena, W. F., Podestá, F., & Lopéz, L., *Space Velocities of Southern Globular Clusters VII. NGC 6397, NGC 6626 (M 28) and NGC 6656 (M 22).* 2013, AJ, submitted on 19 Feb

Ebrová, I., **Jílková**, **L.**, Jungwiert, B., Křížek, M., Bílek, M., Bartošková, K., Skalická, T., & Stoklasová, I., *Quadruple-peaked spectral line profiles as a tool to constrain gravitational potential of shell galaxies.* 2012, A&A, 545, A33

Jílková, **L.**, Carraro, G., Jungwiert, B., & Minchev, I., *The origin and orbit of the old, metal-rich, open cluster NGC 6791. Insights from kinematics.* 2012, A&A, 541, A64

Salinas, R., **Jílková**, **L.**, Carraro, G., Catelan, M., & Amigo, P., *Structural parameters and blue stragglers in Sagittarius dwarf spheroidal galaxy globular clusters.* 2012, MNRAS, 421, 960

Ortolani, S., Barbuy, B., Momany, Y., Saviane, I., Bica, E., **Jílková**, **L.**, Salerno, G. M., & Jungwiert, B., *A Fossil Bulge Globular Cluster Revealed by very Large Telescope Multi-conjugate Adaptive Optics.* 2011, ApJ, 737, 31

Monaco, L., Villanova, S., Moni Bidin, C., Carraro, G., Geisler, D., Bonifacio, P., Gonzalez, O. A., Zoccali, M., & **Jílková**, **L.**, *Lithium-rich giants in the Galactic thick disk.* 2011, A&A, 529, A90

Magrini, L., Randich, S., Zoccali, M., **Jílková**, **L.**, Carraro, G., Galli, D., Maiorca, E., & Busso, M., *Open clusters towards the Galactic centre: chemistry and dynamics. A VLT spectroscopic study of NGC 6192, NGC 6404, NGC 6583.* 2010, A&A, 523, A11

Unrefereed publications (selected)

Jílková, **L.**, Carraro, G., Jungwiert, B., & Minchev, I., *The orbit of the old, metal-rich, open cluster NGC 6791*, in *European Physical Journal Web of Conferences*, Vol. 19 of *European Physical Journal Web of Conferences*, 2012, 7005

Ebrová, I., **Jílková**, **L.**, Jungwiert, B., Bartošková, K., Křížek, M., Bartáková, T., & Stoklasová, I., *Quadruple-Peaked Line-of-Sight Velocity Distributions in Shell Galaxies*, in *Environment and the Formation of Galaxies: 30 Years Later*, ed., I. Ferreras A. Pasquali, 2011, 225

Ebrová, I., Jungwiert, B., Canalizo, G., Bennert, N., & **Jílková**, **L.**, *Shell Galaxies, Dynamical Friction, and Dwarf Disruption*, in *Galaxies in Isolation: Exploring Nature Versus Nurture*, ed., L. Verdes-Montenegro, A. Del Olmo, and J. Sulentic, 2010, ASPC, 421, 252

Jílková, **L.**, Jungwiert, B., Křížek, M., Ebrová, I., Stoklasová, I., Bartáková, T., & Bartosková, K., *Simulations of Line Profile Structure in Shell Galaxies*, in *Galaxy Wars: Stellar Populations and Star Formation in Interacting Galaxies*, ed., B. Smith, J. Higdon, S. Higdon, & N. Bastian, 2012, ASPC, 423, 243

Ebrová, I., Jungwiert, B., Canalizo, G., Bennert, N., & **Jílková**, **L.**, *Shell Galaxies: Dynamical Friction, Gradual Satellite Decay and Merger Dating*, in *Galaxy Wars: Stellar Populations and Star Formation in Interacting Galaxies*, ed., B. Smith, J. Higdon, S. Higdon, & N. Bastian, 2010, ASPC, 423, 236